Dissertation zur Erlangung des Doktorgrades
der Fakultät für Chemie und Pharmazie
der Ludwig-Maximilians-Universität München

# Iron based superconductors and related compounds synthesized by solid state metathesis and high temperature reactions

Rainer Frankovsky
aus
Hermannstadt, Rumänien

2013

**Erklärung**

Diese Dissertation wurde im Sinne von § 7 der Promotionsordnung vom 28. November 2011 von Herrn Prof. Dr. Dirk Johrendt betreut.

**Eidesstattliche Versicherung**

Diese Dissertation wurde eigenständig und ohne unerlaubte Hilfe erarbeitet.

München, 11.04.2013

Rainer Frankovsky

| | |
|---|---|
| Dissertation eingereicht am | 11.04.2013 |
| 1. Gutachter: | Prof. Dr. Dirk Johrendt |
| 2. Gutachter: | Prof. Dr. Wolfgang Schnick |
| Mündliche Prüfung am | 03.06.2013 |

# Danksagung

Zuallererst möchte ich Herrn Prof. Dr. Dirk Johrendt für die Aufnahme in seinen Arbeitskreis und die Möglichkeit zur Bearbeitung eines höchst interessanten Forschungsthemas danken. Besonders für die stete Gesprächsbereitschaft, den daraus entstandenen neuen Ideen und Ansatzpunkten, die Ermutigung bei Problemen, die Freiheit eigene Ideen auszuprobieren und das tolle Arbeitsklima möchte ich mich bedanken.

Herrn Prof. Dr. Wolfgang Schnick danke ich sehr herzlich für die Übernahme des Zweitgutachtens.

Ein großer Dank gilt Herrn Prof. Dr. Konstantin Karaghiosoff, Frau Prof. Dr. Dina Fatthakova-Rohlfing, Herrn Prof. Dr. Hans-Christian Böttcher und Herrn Prof. Dr. Jörn Schmedt auf der Günne für ihre Bereitschaft, als Prüfer an meinem Rigorosum teilzunehmen.

Für die tolle Arbeit und den großen Enthusiasmus möchte ich mich bei meinen Bacheloranden und F-Praktikanten Mona Calik, Roman Pobel, Alexey Marchuk, Frank Tambornino, Constantin (Noggi) v. Schirnding und Alexander André bedanken. Es hat Spaß gemacht mit euch zu arbeiten.

Mein besonderer Dank gilt:

- Marcus Tegel für die unzähligen hilfreichen Diskussionen, das tolle Erlebnis Tokio („Das glaubt mir kein Mensch…"), unvergessliche Singstar-Abende, das unermüdliche Korrekturlesen dieser Arbeit…
- Marianne Martin für das mir so leicht gemachte Einleben in den AK, die ständige gute Laune und die einfach geniale Labornachbarschaft.

- Catrin Löhnert für die Hilfsbereitschaft im täglichen Laborbetrieb und die tolle Unterstützung zu jeder Zeit.
- Gina Friederichs für alle Diskussionen (hat Spaß gemacht), das Korrekturlesen der Arbeit, die Unterstützung am SQUID, Babysitting…
- Franziska Hummel für gemeinsame Pfeif- und *a capella*- Einlagen, die Süßigkeiten, das Korrekturlesen der Arbeit, Babysitting, die Aufnahme von Tieftemperatur-Pulverdiffraktogrammen…
- Erwin Wiesenmayer & Roman Pobel für Anregungen und Disskussionen bzgl. 122-Verbindungen, Babysitting, die vielen lustigen Videos, das Reden über Fußball und Musikgeschmack…
- Daniel Bichler, für die Hilfe bei Fragen zum Magnetismus und zur Leitfähigkeit.
- Veronika Zinth für die Durchführung von Einkristallmessungen und die Verschönerung meines Arbeitsplatzes.
- allen (ehemaligen) Mitgliedern des AK Johrendt für das tolle freundschaftliche Miteinander, sowohl während der Arbeitszeit als auch in der Freizeit: Daniel Bichler, Gina Friederichs, Christine Hieke, Franziska Hummel, Lola Lilensten, Catrin Löhnert, Marianne Martin, Fabian Nitsche, Ursula Pachmayr, Simon Peschke, Roman Pobel, Tobias Stürzer, Marcus Tegel, Erwin Wiesenmayer, Veronika Zinth,. Dank euch, hat das Arbeiten immer Spaß gemacht.
- Thomas Miller für die Aufnahme von Hochtemperatur-Pulverdiffraktogtrammen und der Aushilfe bei benötigten Chemikalien oder Arbeitsgeräten.
- W. Wünschheim für die Lösung aller Soft- und Hardwareprobleme.
- Christian Minke für die Aufnahme zahlreicher EDX-Messungen.
- Hubertus Luetkens vom Paul-Scherrer-Institut für die Unterstützung und Hilfe bei allen Fragen rund um die μSR-Technik und die Mitarbeit bei unserem gemeinsamen Manuskript.

- allen (ehemaligen) Mitgliedern der Arbeitskreise Schnick, Müller-Buschbaum, Oeckler, Lotsch, Schmedt a. d. Günne und Hoch für die super Zusammenarbeit und die tollen AK übergreifenden Veranstaltungen.

Vor allem aber bin ich meiner Familie zu Dank verpflichtet. Meiner Frau Kathrin für ihre Liebe, Unterstützung und Geduld zu jeder Zeit. Unserer Tochter Hannah dafür, dass sie unser Leben mit Sonnenschein füllt. Meinen Eltern Inge und Eduard für die Möglichkeit das zu tun was mich begeistert, ihren Glauben daran und ihre immerwährende Unterstützung dabei. Meinem Bruder Ralf, für die letzten 30 Jahre und 9 Monate und die unglaublichen gemeinsamen Erlebnisse.

*"Door meten tot weten"*

*("Through measurement to knowledge")*

*- Heike Kammerlingh Onnes –*

*"Stupid is as stupid does"*

*- Forrest Gump-*

# Contents

**1 Introduction ..... 1**

**2 Synthesis and Analytical Methods ..... 11**

2.1 Synthesis ..... 11

2.1.1 Synthesis conditions ..... 11

2.1.2 Starting Materials ..... 12

2.2 Analytics ..... 14

2.2.1 X-ray powder diffraction and Rietveld refinements ..... 14

2.2.2 Single crystal X-ray diffraction ..... 16

2.2.3 Energy dispersive X-ray analyses (EDX) ..... 17

2.2.4 Electrical resistance measurements ..... 17

2.2.5 Magnetic measurements ..... 18

**3 $La_3Pd_{4-x}Fe_xGe_4$ ..... 21**

3.1 Motivation ..... 21

3.2 Synthesis ..... 24

3.3 Compositional characterization ..... 24

3.4 Physical Properties ..... 29

3.5 Conclusion ..... 31

3.6 Synthesis of $LaGe_{1.33}Pd_{0.67}$ ..... 31

3.6.1 Synthesis ..... 31

3.6.1 Characterization ..... 32

**4 Synthesis and physical properties of ZrTiAs and $Zr_{1+x}V_{1-x}As$ ..... 33**

4.1 Structural details and motivation ..... 33

4.2 Synthesis ..... 35

4.3 Sample quality ..... 35

4.4 Physical properties ..... 36

4.5 Conclusion ..... 39

**5 Synthesis of $LaFeAsO_{1-x}F_x$ via solid state metathesis reaction ..... 41**

5.1 Motivation ..... 41

5.2 Synthesis ..... 44
5.3 Reaction pathway ..... 45
5.4 Sample quality ..... 46
5.5 Physical properties ..... 49
5.6 Conclusion ..... 52

**6 Synthesis of CaFeAsF and $Ca_{0.4}Nd_{0.6}FeAsF$ via solid state metathesis reaction ..53**

6.1 CaFeAsF ..... 53
6.1.1 Synthesis and reactivity ..... 53
6.1.2 Sample quality and physical properties ..... 54
6.2 $Ca_{0.4}Nd_{0.6}FeAsF$ ..... 56
6.2.1 Synthesis, sample quality and magnetism ..... 57
6.3 Conclusion ..... 59

**7 Co-substituted $LaFe_{1-x}Mn_xAsO_{1-y}F_y$ ..... 61**

7.1 Motivation ..... 61
7.2 Synthesis ..... 63
7.3 Sample quality and structural changes upon doping ..... 64
7.4 Physical properties ..... 68
7.5 Conclusion ..... 78

**8 Summary ..... 81**

**A. Appendix ..... 87**

A.1 Rietveld refinement of $LaGe_{2-x}Pd_x$ ..... 87
A.2 Additional data for Zr*M*As (*M* = V, Ti) and $Zr_{1+x}V_xAs$ ..... 88
A.3 Rietveld refinement of $LaFeAsO_{0.9}F_{0.1}$ ..... 92
A.4 Additional data for CaFeAsF and $Ca_{0.4}Nd_{0.6}FeAsF$ ..... 93
A.5 Synthesis of LaMnAsO ..... 95

**Abbreviations ..... 99**

**Bibliography ..... 101**

**Full list of Publications ..... 109**

**Conference contributions ..... 110**

**Curriculum Vitae ..... 111**

# 1 Introduction

'It was a wonderful sight when the liquid, which looked almost unreal, was seen for the first time. It was not noticed when it flowed in. Its presence could not be confirmed until it had already filled up the vessel. Its surface stood sharply against the vessel like the edge of a knife.'[1]

These words were used by Heike Kammerlingh Onnes describing an experiment from 1908 and which has paved the road for a new era of science, *the properties of matter at low temperatures* (for which the Nobel Prize of Physics was awarded to Kammerlingh Onnes in 1913). The liquid he was talking about was helium, the last of the known elements, which resisted its liquefaction (having a boiling point of only 4.2 K). Soon after his successful experiment, it was possible to reach temperatures as low as 1 K in Kammerlingh Onnes's Laboratory - and the discovery of superconductivity by cooling mercury below 4.2 K followed only three years later.

Superconductivity is the property of some materials to completely loose their electrical resistance below a certain temperature (which is called critical temperature $T_c$). It is understandable that Kammerlingh Onnes was fascinated by this phenomenon because he was able to construct an electrical circuit with a current flowing theoretically forever - something that must have looked like a perpetual motion[2]. It is probably this ability that explains the great fascination and attraction of superconducting materials even today.

Since those early days, a lot of superconducting materials have been found. While the first 20 years were restricted to discovering superconducting elements, with Nb having the highest $T_c$ of all elements (9.4 K), this development was followed by the observation of superconductivity in compounds like NbN and intermetallic compounds like $Nb_3Sn$ and $Nb_3Ge$[3, 4]. The latter two compounds were found to be superconducting by Bernd Matthias and it was him who also discovered the most superconducting materials overall. This might have been because Matthias was

following an alternative approach, trying to find new correlations between properties like the chemical structure or the number of valence electrons per atom and high critical temperatures ('*Matthias Rule*' 1955)[5, 6], instead of following any known theoretical predictions. These empirical rules are particularly suited for the type of intermetallic compounds mentioned above. They belong to the so-called A15 compounds and they crystallize in the in the $V_3Si$-type structure (often called A15-type). The discovery of superconductivity in the A15 compounds also gave hope to overcome the two main difficulties for the technical application of superconductors:

Already Kammerlingh Onnes had realized that superconductors could be used as electromagnets to generate high magnetic fields. One problem however had been, that in the early-discovered materials the superconducting state is destroyed even by small magnetic fields, making it unrealistic to build magnets from superconducting wires of these materials. Conventional electromagnets made of copper coils and an iron core can however produce magnetic flux densities of up to 1.6 T[7], a flux density where the superconducting state of all early-discovered materials already is destroyed. In 1960, it was found that $Nb_3Sn$ could withstand flux density of up to 9 T in real applications and nowadays flux densities of even over 20 T can be achieved in superconducting magnets made of $Nb_3Sn$ wires[2, 5, 8]. Superconducting magnets today are used in many applications - for magneto resonance imaging, for analytical tools like NMR or in magnetometers equipped with SQUID sensors. Even at particle accelerators like the Large Hadron Collider at CERN, thousands of superconducting magnets cooled by tons of liquid helium at 1.9 K and 4.2 K are employed[9].

The second, more obvious problem, that makes a technical application of superconductors often uneconomical, is the cost of the coolant, i. e. liquid helium. This makes it understandable why, after almost two decades of stagnation in reaching higher $T_c$s (the above-mentioned $Nb_3Ge$ was the record holder for a long time), the discovery of the so-called cuprate superconductors has caused an enormous uproar in the 1980s. First reports of possible high $T_c$ superconductivity

in the Ba-La-Cu-O System by Bednorz and Müller have therefore unleashed an avalanche of reports about new high $T_c$ cuprate superconductors, such as the famous YBCO ($YBa_2Cu_3O_{7-x}$, Tc ~ 90 K) [10, 11].

The theoretical framework to explain superconductivity at low temperatures had been established in the mid-1950s. According to the BCS theory, two electrons form a Cooper Pair, which cannot be scattered by the crystal lattice anymore and as a result the resistance of the compound is zero (for details see [5, 12, 13]). However, according to the BCS theory the transition temperature is expected not to exceed ~ 30 K, which is possibly a reason that there had seemed to be little hope to find high $T_c$ superconductors before the groundbreaking discovery by Bednorz and Müller.

But as quick as the hope to overcome the chore of helium cooling and to use the way more economic nitrogen cooling instead had risen, the disillusionment had set in. Because of their ceramic character, the cuprates are very brittle making it difficult to construct flexible materials such as wires. This, together with the anisotropy of the physical properties, make cuprate superconductors only applicable in niche products and this is also the reason why conventional superconductors like the A15 compounds are still preferably used in technical applications.

Therefore, finding new superconducting materials by intuition, chemical understanding and the help of theoretical forecasts, is still one of the most challenging but also worthwhile tasks of modern solid-state chemistry and physics – both from a theoretical point of view as well as the objective to improve everyday life. It should take more than 20 years since the discovery of superconductivity in the cuprates to find a new class of high-temperature superconductors. In 2006 and 2008, reports about superconducting LaFePO and $LaFeAsO_{1-x}F_x$ were published[14, 15]. The latter with a reported $T_c$ of 26 K has triggered a new gold rush, comparable to the discovery of high-temperature superconductivity in the 1980s and new results have been proposed almost daily on the pre-print server of the Cornell University (*arxiv.org*). The non-

superconducting parent compound LaFeAsO has already been known since 2000 but was not getting much attention from the superconductivity community. This is because LaFeAsO contains iron, which in its elemental form is a strong ferromagnet. Since ferromagnetism destroys the superconducting state, it has been an unspoken law that compounds containing iron cannot achieve high transition temperatures or even show superconducting properties at all, although it should be clear, that properties of the elements cannot automatically be transferred to compounds containing these elements. The discovery of high $T_c$ superconductivity in the iron arsenides is therefore another example that swimming against the tide and trying an unconventional approach may be worthwhile in superconductivity research.

A closer look at the properties of the non-superconducting parent compound LaFeAsO revealed that below ~ 155 K, a structural phase transition followed by anitferromagnetic ordering at ~ 138 K occurs (details will be discussed later), which is indicated by anomalies in the electrical resistance and magnetic susceptibility[15-17]. Another already known iron arsenide compound, $BaFe_2As_2$ showed comparable anomalies in physical properties and is built up of similar structural units [18, 19]. Going straight forward, shortly after the report of superconducting $LaFeAsO_{1-x}F_x$, a critical temperature as high as 38 K in $Ba_{1-x}K_xFe_2As_2$ has been achieved[20].

According to their structure, iron arsenide superconductors can be divided into different classes. $LaFeAsO_{1-x}F_x$ belongs to the so-called 1111 class and $Ba_{1-x}K_xFe_2As_2$ was the first representative of the 122 family, where the numbers simply represent the corresponding compositions.

LaFeAsO and other 1111 compounds crystallize in the tetragonal ZrCuSiAs-type structure (space group *P*4/*nmm*), a filled variant of the PbFCl type. LaFeAsO is built up from two-dimensional iron arsenide layers (edge sharing $FeAs_{4/4}$ tetrahedra), which are separated by two-dimensional lanthanum oxide layers (edge sharing $OLa_{4/4}$ tetrahedra)[21, 22]. Replacing the $OLa_{4/4}$ layers by $AEF_{4/4}$ –layers (*AE* = Ca, Sr, Eu) leads to the isostructural 1111 compounds *AE*FeAsF which are the parent compounds of some other high-temperature superconductors (e. g. $Ca_{1-x}Nd_xFeAsF$

with $T_c$ = 56 K, for details see chapter 4)[23-27]. The two-dimensional iron pnictide layers constitute the structural motif, which is shared by all of the new iron-based superconductors. Beside the already mentioned 1111- and 122- class, there are superconductors with 111- (NaFeAs, LiFeAs, 2008)[28-30], 11 (FeSe and $Fe_{1+y}(Te_{1-x}Se_x)$, 2008)[31, 32] or more complicated 21311- stoichiometry ($Sr_2VO_3FeAs$, 2009) [33]. Even the most recently discovered iron platinum arsenide superconductors ($Ca_{10}(Fe_{1-x}Pt_xAs)_{10}(Pt_zAs_8)$, 2010) contain iron-arsenide tetrahedra. For comparison, the crystal structures of some iron arsenide superconductors (or parent compounds) are depicted in Figure 1.1.

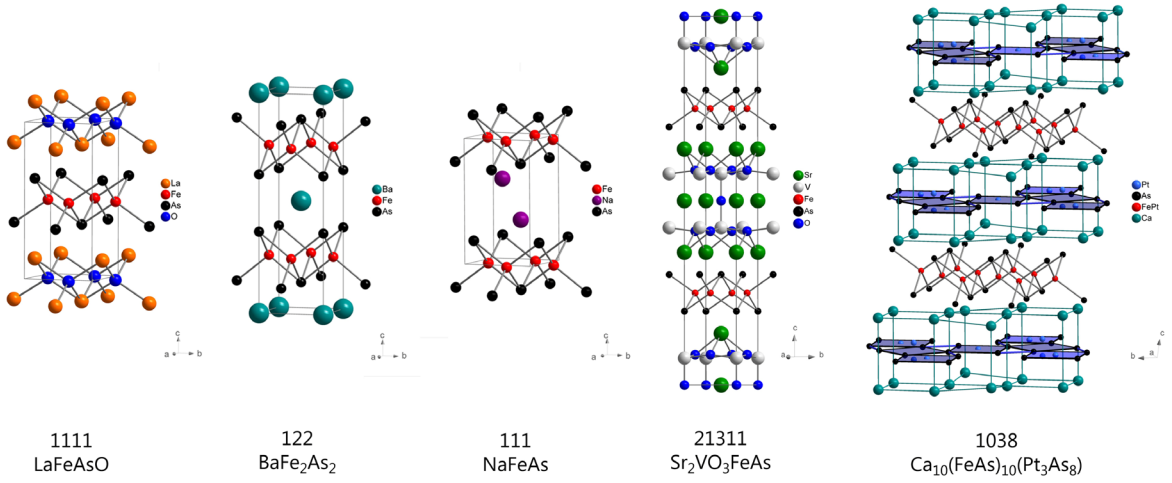


**Figure 1.1:** Crystal structure of some iron-based superconductors showing one representative of each class. Removing the Na atoms from NaFeAs and replacing As by Se leads to the structure of FeSe.

In the different compounds, the iron arsenide layers are separated either by alkali atoms (111), alkaline earth atoms (122), rare earth oxide or alkaline earth fluoride layers (1111), perovskite-like layers (21311) or by Ca / PtAs layers (1038). In the 11 family, the iron-pnictide layers are not separated by any other atoms or structural motifs, but are stacked directly. It is therefore obvious, that the iron pnictide layers are the key to the physical properties of all compounds. Indeed, early theoretical calculations of non-superconducting LaFeAsO revealed that the electronic states near the Fermi-Energy $E_F$ are dominated by contributions from Fe-3d and As-p states. Band structure calculations also showed that LaFeAsO is a semi-metal,

forming so-called hole- and electron-pockets (for details see [34-36]) and Fermi surface calculations proposed a spin density wave (SDW) antiferromagnetic ground state at low temperatures[37]. As mentioned above, LaFeAsO undergoes a magnetic transition at $T_N$ ~ 137 K which was found by neutron diffraction experiments and confirmed the proposed SDW anitferromagnetism and also revealed a stripe-like ordering of the magnetic moments (the magnetic moments lie horizontally within the *ab*-plane and are antiferromagnetically aligned along the *a*- and *c*- axis but ferromagnetically aligned along the *b*-axis)[38]. Well above the Néel temperature, a structural transition was observed ($T_s$ ~ 155 K). The crystal structure changes from the tetragonal space group *P*4/*nmm* to orthorhombic *Cmme* with $a_{ortho} = \sqrt{2} \cdot a_{tetra} - \delta$; $b_{ortho} = \sqrt{2} \cdot b_{tetra} + \delta$ and $c_{ortho} \sim c_{tetra}$ [39].

Similar electronic properties and phase transitions have been observed for the 122 parent compound $BaFe_2As_2$. The structure changes from tetragonal to orthorhombic symmetry and the magnetic ordering is a stripe-like antiferromagnetic alignment (with $T_s$ and $T_N$ at 140 K)[18, 40]. Introducing electrons (e.g. $LaFeAsO_{1-x}F_x$) or holes (e.g. $Ba_{1-x}K_xFe_2As_2$) by doping with elements having a different number of valence electrons or by applying pressure (e. g. $SrFe_2As_2$ or $BaFe_2As_2$) leads to a gradual decrease of $T_s$ and $T_N$ and finally superconductivity is induced [15, 20, 41]. To illustrate the relation between these different phases and the doping level *x*, the phase diagram of $LaFeAsO_{1-x}F_x$ is exemplarily shown in Figure 1.2.

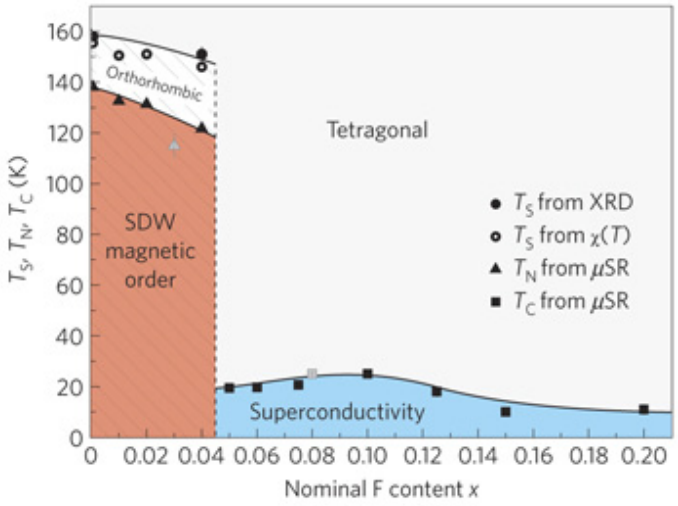


**Figure 1.2:** Electronic phase diagram of $LaFeAsO_{1-x}F_x$. Reprinted by permission from Nature Publishing Group: Nature Materials[42]. Copyright 2009.

Up to the present day, nearly any possible substitution of elements in the parent compounds has been realized by which many superconducting compounds have been published (for an overview see [43]). Contrary to the cuprates, superconductivity in the iron arsenides can even be induced by substituting the iron metal itself, referred to as direct doping. $BaFe_{2-x}Co_xAs_2$ ($T_c$ = 22 K) and $LaFe_{1-x}Co_xAsO$ ($T_c$ = 14 K) are two examples of such directly electron-doped systems[44, 45]. On the other hand, direct hole-doping in $LaFe_{1-x}Mn_xAsO$ or $BaFe_{2-x}Mn_xAs_2$ does not lead to superconducting properties (which will be discussed in detail in chapter 7)[46-48].

There have been many attempts to find a correlation between structural and/or electronic changes and the occurrence of (high-$T_c$) superconductivity. One structural parameter that has often been discussed to be crucial for high $T_c$s is the As-Fe-As bond angle $\varepsilon$. The highest $T_c$s in the 122 compounds ($Ba_{0.6}K_{0.4}Fe_2As_2$) and the 1111 compounds ($SmFeAsO_{1-x}F_x$)[49] are found when the tetrahedral angle $\varepsilon$ is close to the ideal value of 109.47°[43, 50, 51]. Another correlation was found between the distance of the iron pnictide layers (and therefore the dimensionality of the structure) and the highest attainable critical temperatures in the corresponding structure types. Before superconductivity in the 21311 family was discovered in early 2009, the largest distance between the iron arsenide layers (corresponding to

the highest $T_c$) had been found in the 1111 family (max. $T_c$ = 56 K in $SmFeASO_{1-x}F_x$ and $Ca_{1-x}Nd_xFeAsF$) followed by the 122 family (max. $T_c$ = 38 K in $Ba_{1-x}KFe_2As_2$) and the 111 family (max. $T_c$ = 18 K in LiFeAs). The smallest distance and the lowest $T_c$ had been found in the 11 family (max. $T_c$ = 8 K in FeSe). Therefore, a promising task was to find compounds with large interlayer distances. However, in both the 21311 and the 1038 structures, the interlayer distances are larger compared to the 1111 family, but the maximum attainable critical temperatures ($T_c$ = 37 K in $Sr_2VO_3FeAs$ [33] and 35 K for $Ca_{10}(FeAs)_{10}(Pt_4As_8)$[52]) remain well below the ones obtained in the 1111 compounds.

Newest investigations about the interplay between doping and structural changes in doped $BaFe_2As_2$ show that it is more probable that charge modifications play a more important role for the suppression of magnetism and the emergence of superconductivity: Zinth *et al.* have shown that charge compensation in $Ba_{1-x}K_xFe_{1.86}Co_{0.14}As_2$ ($x \approx 0.14$) recovers the behavior of the parent compound (magnetic and structural transition) and superconductivity re-emerges at lower (electron-doped) as well as higher (hole-doped) potassium concentrations[53]. This shows that the physical properties can be controlled by modifying the charge in $BaFe_2As_2$, despite the structural disorder induced by simultaneous doping of potassium and cobalt into the system. Overviews of the relationship between structural and/or electronic properties and superconductivity are given by Johnston[43], Stewart[54] and Johrendt [36].

When work on this thesis had started in the beginning of 2009, the above-mentioned correlation between the interlayer distance and the critical temperature had not been proven to be invalid. Therefore, one goal was to find compounds with structural motifs similar to the iron pnicitdes (with large distances between the building blocks) and possible superconducting properties upon doping. In chapter 3 ($La_3Pd_{4-x}Fe_xGe_4$) and chapter 4 ($ZrMAs$ ($M$ = Ti, V)) such compounds are discussed and their physical and structural details are presented. The latter have already been known for eight years, but the physical properties have not been

studied yet and the example of LaFeAsO teaches us, that it sometimes can be worthwhile to check the physical properties of seemingly unspectacular compounds.

The efforts to synthesize BiFeAsO, a hypothetical compound isostructural to LaFeAsO, led to the development of a solid-state metathesis synthesis route suitable for (superconducting) iron-arsenide compounds of the 1111 family. Chapter 5 discusses general considerations about this synthesis route, its advantages compared to conventional methods as well as the reaction pathway at the example of the series $LaFeAsO_{1-x}F_x$. Since the latter yielded samples of high purity, this alternative synthesis route has been extended to the synthesis of CaFeAsF and $Ca_{0.4}Nd_{0.6}FeAsF$, presented in chapter 6.

Finally chapter 7 ($LaFe_{1-x}Mn_xAsO_{1-y}F_{y,}$) is dedicated to the interplay between structural and electronic changes upon doping and the resulting physical properties and it also shows the large variability of the used metathesis reaction. Is it possible to recover the physical properties of the parent compound LaFeAsO in charge-compensated $LaFe_{0.9}Mn_{0.1}AsO_{0.1}F_{0.1}$ or even induce superconductivity in formally electron doped $LaFe_{0.9}Mn_{0.1}AsO_{1-y}F_y$ ($y > 0.2$)?

And how does the structure change upon doping simultaneously with Mn and F?

These questions, along with the unexplained absence of superconductivity in directly hole-doped iron arsenide compounds like $LaFe_{1-x}Mn_xAsO$ are within the scope of the present thesis, thus providing new insights into this interesting and highly topical class of materials. Furthermore, the search for alternative synthesis routes and the thereby possibly increased sample quality is one of the very important tasks when it comes to questions about applicability of these new materials or the synthesis of still unknown compounds.

# 2 Synthesis and Analytical Methods

## 2.1 Synthesis

### 2.1.1 Synthesis conditions

Unless stated otherwise, the storage and handling of the starting materials and all products was realized using a glove-box (BRAUN, MB150-Gl, $O_2$ < 1 ppm, $H_2O$ < 1 ppm) containing an atmosphere of purified argon. Generally, the starting materials were well homogenized using an agate mortar and filled into the desired reaction vessels. For reaction mixtures which contained very fluffy components (e. g. LaOCl), a brush was used to transfer the mixture to the vessels. All reactions, except the synthesis of LaOCl, were performed under an atmosphere of purified argon. The argon (Argon 5.0, AIR LIQUIDE) was dried by passing the gas through columns filled with BTS-catalyst (copper (I) oxide dispersed on a ceramic carrier matrix, FLUKA) kept at 393 K, molecular sieve (pore size 0.4 nm, Merck) and phosphorous pentoxide (MERCK).

#### 2.1.1.1 Syntheses in resistance furnaces

Depending on the components of the reaction mixture, alumina crucibles, niobium tubes or a combination of both (alumina crucible inside the Nb tube) were used as reaction vessels. These vessels were sealed in pre-dried silica ampoules (HSQ300, $Ø_{ext}$ = 14 mm, wall thickness 1.2 mm, VOGELSBERGER QUARZGLASTECHNIK) using an oxyhydrogen burner, under static inert gas conditions. Prior to sealing, the vessel containing ampoules were evacuated and re-filled with argon several times. Evacuation was achieved by using a rotary vane pump (RZ5, suction capacity 5.6 $m^3$/h, VACUUBRAND). The syntheses were performed in tubular resistance furnaces equipped with programmable temperature controllers (model 24089, EUROTHERM) and Pt/PtRh or NiCr/Ni thermocouples. The reaction temperatures

varied between 773 K and 1373 K and all reaction mixtures were cooled to room temperature after the heating steps. Unless stated otherwise the cooling rate was 200 K/h. The used heating rates and reaction times of the various syntheses can be found in the detailed descriptions of the corresponding chapters. After the first annealing step the samples where ground, checked for purity and annealed again if necessary.

#### 2.1.1.2 Arc melting syntheses

To gain good homogeneity of the reaction mixture and prevent the loss of reactants, the starting compounds were pressed into pellets with a diameter of 4 to 5 mm. The pellets were then placed in a water-cooled copper head in the arc melting furnace. To obtain inert conditions the whole gadget was evacuated several times and flooded with inert gas (argon) in between. The pellets were arc melted twice (once each side) using a current of 15–60 A. To check for evaporation during arc melting, the reaction mixture was weighed before and after the reaction; weight losses of smaller than 2 wt% were tolerated.

### 2.1.2 Starting Materials

An overview of the commercially available materials used in this work is given in Table 2.1. The purity (%), molecular weight (g/mol), appearance and the supplier are listed.

**Table 2.1**: Commercially available Chemicals used in this thesis.

| Material | Purity | m. w. | Appearance | Supplier |
|---|---|---|---|---|
| Ammonium chloride ($NH_4Cl$) | 99.9 | 53.4910 | Powder | FLUKA |
| Arsenic (As) | 99.999 | 74.9216 | Pieces | ALFA AESAR |
| Calcium (Ca) | 99.99 | 40.0780 | Pieces | SIGMA ALDRICH |
| Calcium chloride ($CaCl_2$) | 99.999 | 110.984 | Powder | ALFA AESAR |
| Calcium fluoride ($CaF_2$) | 99.999 | 78.0750 | Powder | ALFA AESAR |
| Germanium (Ge) | 99.999 | 72.6400 | Pieces | SIGMA ALDRICH |
| Iron (Fe) | 99.9 | 55.8450 | Powder | CHEMPUR |
| Lanthanum (La) | 99.9 | 138.9055 | Ingot | SMART ELEMENTS |
| Lanthanum fluoride ($LaF_3$) | 99.99 | 195.9007 | Powder | SIGMA-ALDRICH |
| Lanthanum oxide ($La_2O_3$) | 99.999 | 325.8020 | Powder | ALFA AESAR |
| Manganese (Mn) | 99.99 | 54.9380 | Granules | ALFA AESAR |
| Neodymium fluoride ($NdF_3$) | 99.9 | 201.2350 | Powder | ALFA AESAR |
| Palladium (Pd) | 99.95 | 106.4200 | Grated | ALLG. GOLD- UND SILBERSCHEIDE-ANSTALT AG |
| Sodium (Na) | 99.8 | 22.9898 | Ingot | ALFA AESAR |
| Titanium (Ti) | 99.5 | 47.8670 | Powder | ALFA AESAR |
| Vanadium (V) | 99.90 | 50.9415 | Powder | ABCR |
| Zirconium (Zr) | 99.97 | 91.2240 | Pieces | SMART ELEMENTS |

### 2.1.2.1 Binary and ternary iron arsenides (FeAs, NaFeAs, NaMnAs)

For the synthesis of the binary iron arsenide FeAs, stoichiometric amounts of the elements were heated directly in silica ampoules, without using any additional crucibles. The final reaction temperature was 973 K (heated at a rate of 50 K/h) and the mixture was kept there for 20 h.

The as-synthesized FeAs was heated with stoichiometric amounts of sodium to obtain the ternary iron arsenide NaFeAs. The mixture was heated to 1023 K in a niobium crucible sealed in a silica ampoule (to avoid the reaction of the alkali

metal with the silica ampoule) and kept at this temperature for 48 h[55]. In contrast to NaFeAs, NaMnAs could be prepared better from the elements rather than the binary metal arsenide[56]. It turned out that a combination of an alumina crucible and a sealed niobium tube (see section 2.1.1.1) inside of the sealed silica ampoule works best for this synthesis. For the reaction, very slow heating rates of 30 K/h between 623 K and 873 K (with heating for 10 h at 873 K) are necessary.

#### 2.1.2.2 LaOCl

According to the following reaction equation, stoichiometric amounts of $La_2O_3$ and $NH_4Cl$ (with an excess of 0.15 eq.) were put on an alumina boat, which was placed inside a gas flow furnace. After evacuating the reaction aperture several times, the product was synthesized in a dynamic atmosphere of nitrogen at temperatures between 773 K and 1173 K. This synthesis is a slightly modified version of[57]. The obtained product was a phase-pure, colourless and very fluffy powder.

$$La_2O_3 + 2\ NH_4Cl \xrightarrow{N_2} 2\ LaOCl + 2\ NH_3\uparrow + H_2O\uparrow$$

#### 2.1.2.3 CaFCl

Equal amounts of $CaF_2$ and $CaCl_2$ were heated in a sealed silica tube at 923 K for 10 h, with a heating rate of 100 K/h to give a white, single phase powder of CaFCl[58]. Higher temperatures led to higher amounts of $CaF_2$ and $CaCl_2$ as impurity phases, indicating that CaFCl decomposes at higher temperatures[58].

## 2.2 Analytics

### 2.2.1 X-ray powder diffraction and Rietveld refinements

The obtained sample powders were characterized by recording X-ray powder diffraction patterns. Less air-sensitive samples were measured using flat sample holders, with the sample powders placed in between two polyacetate films.

Air-sensitive samples were sealed in argon-filled glass capillaries with outer diameters between 0.1 mm and 0.3 mm (HILGENBERG). The diffraction patterns were recorded on the following computer controlled diffractometers:

- HUBER G670 Guinier Imaging Plate Diffractometer (Cu-$K_{\alpha1}$ radiation, λ = 154.06 pm, Ge(111) monochromator, silicon dioxide and silicon as external standards, oscillating flat sample holder, controlled by the HUBER-G670 Imaging Plate Guinier Camera control software[59]).
- HUBER G670 Guinier Imaging Plate Diffractometer (Co-$K_{\alpha1}$ radiation, λ = 179.02 pm, Ge(111) monochromator, silicon as external standard, oscillating flat sample holder, controlled by the HUBER-G670 Imaging Plate Guinier Camera control software[59]).
- STOE STADI P (Cu-$K_{\alpha1}$ radiation, λ = 154.06 pm, Ge(111) monochromator, silicon as external standard, rotating capillary (Debye-Scherrer geometry) or oscillating flat sample holder (transmission geometry), controlled by the WinXPOW software package[60]).
- STOE STADI P (Mo-$K_{\alpha1}$ radiation, λ = 70.93 pm, Ge(111) monochromator, silicon as external standard, rotating capillary (Debye-Scherrer geometry) or oscillating flat sample holder (transmission geometry), controlled by the WinXPOW software package[60]).

Temperature-dependent X-ray data between 298 K and 1033 K were collected on the STOE STADI P (Mo-$K_{\alpha1}$ radiation) diffractometer, equipped with a high-temperature furnace (STOE capillary furnace). Data collected with the Huber diffractometer were pre-processed with the program HConvert[61] (see [13] for details). For phase identification and phase purity checks, the software package WinXPOW was used. The package included the programs GRAPHIC[62], THEO[63] (which was used for simulating theoretical patterns) and the semi-automatic search routine Search[64] (for phase analyses) which accesses the PDF 2 or the PDF 4+ JCPDS-database[65, 66].

To identify unknown phases, the patterns were automatically indexed using the TOPAS[67] or manually using the CMPR[68] program.

Rietveld refinements of the recorded diffraction patterns were performed with the TOPAS package using the fundamental parameter approach to generate the reflection profiles. If necessary, a modified approach of *Le Bail* and *Jounneaux*[69] was used to describe small peak half width and shape anisotropy effects. A description of the implemented approach and several other diffractometer-specific templates (created by *M. Tegel*) which were used can be found in[13]. Giving consideration to possible preferred orientations of the crystallites, spherical harmonics functions with orders of 4, 6 or 8 were used. For capillary measurements, absorption was corrected using the capillary diameter (as sample thickness), the estimated powder densities (50-70 % of the crystallographic densities) and the calculated linear absorption coefficients. If necessary, empirical absorption corrections have been performed for flat sample holder measurements with the parameters described above, but an estimated sample thickness instead of the well-defined capillary diameter.

### 2.2.2 Single crystal X-ray diffraction

A first selection of suitable single crystals was done under a stereo microscope (Leica MZ6, LEICA). The selected crystals were fixed on very tiny silica glass filaments with superglue, which themselves were placed on brass pins. For a second quality check of the crystals, Laue diffraction patterns were recorded on imaging plates[70] using a precession camera (Buerger Precession Camera 205, HUBER), which operates with white Mo radiation. (Röntgengenerator Kristalloflex 760, SIEMENS). The recorded patterns were scanned with a laser scanner (BAS 2500 Bio Imaging Analyser, FUJI PHOTO FILM CORPORATION), read in with the BASREADER[71] software and displayed by the program TINA[72].

Single crystal data were measured using a STOE IPDS single-crystal x-ray diffractometer (Mo-$K_{\alpha 1}$ radiation, $\lambda$ = 70.93 pm, graphite monochromator). The programs X-RED 32 [73], XPREP [74] and XSHAPE [75] were used for data reduction,

absorption correction and crystal shape optimization. Crystal structures were solved and refined using the WinGX [76, 77] software and the implemented programs SHELXS-97 and SHELXL-97 [78-80]. The crystal structures were visualized with DIAMOND[81].

### 2.2.3 Energy dispersive X-ray analyses (EDX)

Samples for scanning electron microscopy (powder or single crystals) were put on double sided adhesive carbon discs (PANO, Wetzlar) on brass sample holders. EDX was used for semi-quantitative analyses of the samples' chemical composition. A JEOL (model JSM-6500F) scanning electronic microscope equipped with an OXFORD EDX detector (model 7418) was used to perform the analyses based on the characteristic X-ray emissions of elements due to electron bombardment. The INCA [82] software package was used for the collection of the spectra. For accuracy reasons, at least 5 different spots of a sample were recorded and the obtained compositions were averaged, if reasonable.

### 2.2.4 Electrical resistance measurements

Measurements of the electrical resistance between 8 K and 320 K were performed on cold pressed pellets of the samples (Ø= 4-6 mm, thickness: 0.8–1.3 mm). The cold pressed samples were usually heated to 873-1173 K for 40 h after being sealed in the same reaction vessel type which was used for the synthesis. The current-reversal four-terminal sensing method was applied[83, 84] to measure the voltage drop across each sample. Therefore, the pellets were fixed on brass sample holders using the epoxy resin Stycast (2850FT, EMERSON & CUMING; with Tetraethylenepentamine as catalyst). Four copper wires were attached to each pellet and contacted with silver conducting paint. Two wires were connected to the source meter (Source Meter 2400. KEITHLEY, square waves with amplitudes between 2 µA and 5 mA, frequency of 2 Hz), the other two wires were connected to a KEITHLEY 2182 nanovoltmeter in differential voltage setup. The sample resistance

was determined using Ohm's law and the specific resistivity according to the Van-der-Pauw method[85]. Measurements between 8 K and 320 K were realized in a closed-cycle He-cryostat (CRYODYNE 22 CP closed-cycle cold head with 8200 compressor, CTI CRYOGENICS) connected to a LAKESHORE temperature controller (model 311). High-vacuum conditions were achieved by using a turbomolecular vacuum pump (PFEIFFER VACUUM, pressure < $1 \cdot 10^{-6}$ mbar). Temperature control and data acquisition was performed by using the LEITMESS[86] software. The obtained data were processed and visualized in ORIGIN[87].

### 2.2.5 Magnetic measurements

Magnetic characterizations of polycrystalline samples were either performed on a SQUID magnetometer (MPMS-XL5, Quantum Design Inc.) or a self-manufactured AC susceptometer[13].

The MPMS-XL5 employs a SQUID sensor (Superconducting Quantum Interference Device) and allows external magnetic fields up to 50 kOe and operating temperatures between 1.8 K and 400 K. A detailed description of the different measurement methods and technical details of the SQUID magnetometer can be found elsewhere[88, 89]. The magnetometer was controlled and data were collected with the MPMS MultiVu software[90]. For each measurement, 30 mg to 50 mg of substance were put into a gelatine capsule, which was fixed in a straw as sample holder. The generated data files were either processed with Origin[87] or with the fully automatic SQUID processor software[91]. Corrections were made for diamagnetic contributions of the sample holder and the diamagnetic increments of the ions, which can be found in[92].

The fully automatic dual-coil AC susceptometer operates in the temperature range from 3.5 K to 320 K and alternating magnetic fields of up to 8 Oe (usually 3.5 Oe were applied). A detailed description of the susceptometer setup, calibration procedure and operating modes can be found in[13]. As for the SQUID magnetometer, samples were put into gelatine capsules fixed in straws. The AC

susceptometer control software was used for operating the AC susceptometer and for data processing.

For the collected magnetic data, the CGS unit system was used. The definition of the used magnetic quantities in this thesis can be found elsewhere[92, 93].

# 3 $La_3Pd_{4-x}Fe_xGe_4$

## 3.1 Motivation

In the beginning of 2009, there seemed to be some structural preconditions for the occurrence of superconductivity in the iron arsenide family. One of these was the distance between two iron arsenide layers. Considering the compounds $Li_{1-x}FeAs$ ($T_c$ = 18 K), $Ba_{1-x}K_xFe_2As_2$ ($T_c$ = 38 K) and $Sr_{1-x}Sm_xFeAsF$ ($T_c$ = 56 K), there is an empirical correlation between the $FeAs_{4/4}$-layer distance and the critical temperature, i. e. the highest $T_c$ is observed in the compound with the largest interlayer distance[20, 94, 95]. The interlayer distance also seems to play a role in the 122- iron arsenides (crystallizing in the $ThCr_2Si_2$-type structure). Whereas in $BaFe_2As_2$ and $SrFe_2As_2$, it is possible to induce superconductivity by applying an external pressure, this is not the case in $CaFe_2As_2$[96, 97]. In $CaFe_2As_2$, the interlayer distance is not only the smallest in the latter compounds, but under pressure the structure becomes even three-dimensional by the formation of As–As bonds along the *c* axis. In each of the $REFe_2As_2$ - compounds (*RE* = ca, Sr, Ba) the structural distortion to the orthorhombic crystal system is suppressed (and superconductivity is induced in $BaFe_2As_2$ and $SrFe_2As_2$) when external pressure is applied. However in $CaFe_2As_2$, the lattice parameter *c* decreases by 9.5 % upon cooling from ambient temperature to 50 K under an external pressure of 0.63 GPa[98]. This low-temperature phase is sometimes improperly called the 'collapsed tetragonal' phase[98].

Even before the discovery of superconductivity in $Ba_{1-x}K_xFe_2As_2$, intermetallic compounds of the $ThCr_2Si_2$-type structure had been extensively studied and they had showed a large variety of possible element combinations. Among the germanides, $LaFe_2Ge_2$ and $LaPd_2Ge_2$ are two representatives of this structure type[99, 100]. Whereas the iron germanide does not show superconducting properties, the Pd compound exhibits superconductivity with a critical temperature

of 1.12 K. In both compounds, the shortest Ge–Ge distances are in the range of the interatomic distance of elemental germanium (2.45 Å). This leads to the formation of dimers along the *c*-axis, which can be written as $[Ge_2]^{6-}$ units following the Zintl-concept, and a very short distance between the tetrahedral layers and therefore a more three-dimensional structure - similar to $CaFe_2As_2$ under pressure. Earlier investigations had shown that it is not possible to induce superconductivity in hole-doped $La_{1-x}AE_xFe_2Ge_2$ (*AE* = Ca, Sr)[93] in an analogous way it has been realized for $Ba_{1-x}K_xFe_2As_2$.

Since a small interlayer distance of the metal-based tetrahedral layers had seemed to have contrary effects for the occurrence of superconductivity, a major goal was to find compounds with larger distances. One compound, which consists of similar transition metal-based layers as the above-mentioned iron arsenides / germanides and which additionally has a very large interlayer distance, is $La_3Pd_4Ge_4$ with the orthorhombic $U_3Ni_4Si_4$-type structure (Figure 3.1) [101, 102].

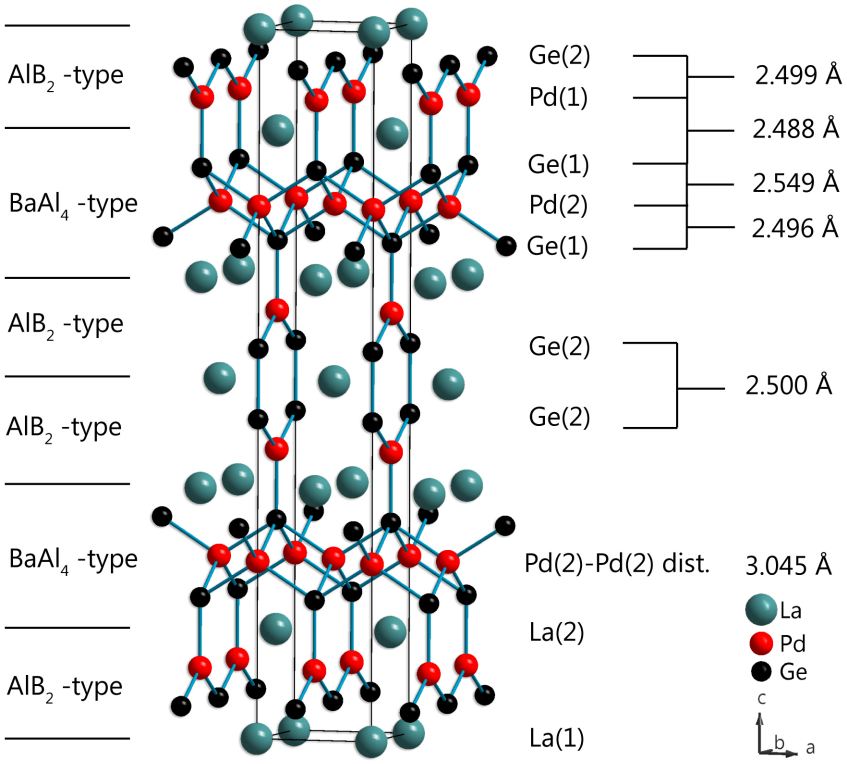


**Figure 3.1:** Crystal structure of $La_3Pd_4Ge_4$ with the different building blocks (left) and some interatomic distances (right)[102].

The $U_3Ni_4Si_4$–type structure is built up from alternating $BaAl_4$-type and $AlB_2$-type layers, where each $BaAl_4$ unit is separated by two $AlB_2$ units[103]. The $ThCr_2Si_2$-type structure is an ordered ternary derivate of the $BaAl_4$-type[104]. Therefore, $La_3Pd_4Ge_4$ is composed of $LaPd_2Ge_2$ layers (hosting the $PdGe_{4/4}$ tetrahedra), separated by two $La(Pd_{0.5}Ge_{0.5})_2$ layers, which are a ternary variant of the $AlB_2$-type (Figure 3.1). In the $AlB_2$-type layers, the Pd atoms are coordinated trigonally planar by Ge atoms. Since one of these atoms (Ge(1)) is shared with the $BaAl_4$-type layers, where it is part of the germanide tetrahedra, the distance between the $AlB_2$ units and the $BaAl_4$ units is only 2.5 Å. This means that although the distance between the tetrahedral layers is increased, the structure is three-dimensional because of bonds between these layers. Nevertheless, the insertion of $AlB_2$ units into $LaPd_2Ge_2$ and the enlargement of the distance between the $PdGe_{4/4}$-layers (from 2.5 Å in $LaPd_2Ge_2$ to 9.9 Å in $La_3Pd_4Ge_4$) doubles the critical temperature from 1.12 K to 2.75 K in $La_3Pd_4Ge_4$ [100, 102]. A summary of the crystallographic parameters of $La_3Pd_4Ge_4$ is given in Table 3.1.

**Table 3.1:** Structural parameters of $La_3Pd_4Ge_4$[102].

| Spacegroup | *Immm* (79), $Z$ = 2 | | | | |
|---|---|---|---|---|---|
| Lattice parameters [pm] | $a$ = 422.93(1); $b$ = 438.23(1); $c$ = 2501.09(8) | | | | |
| **Atom** | **Site** | ***x*** | ***y*** | ***z*** | **Occ.** |
| La(1) | 2*a* | 0 | 0 | 0 | 1 |
| La(2) | 4*j* | ½ | 0 | 0.3513(2) | 1 |
| Pd(1) | 4*j* | ½ | 0 | 0.0979(2) | 1 |
| Pd(2) | 4*i* | 0 | 0 | 0.2501(2) | 1 |
| Ge(1) | 4*j* | ½ | 0 | 0.1972(2) | 1 |
| Ge(2) | 4*i* | 0 | 0 | 0.4503(3) | 1 |

In this chapter, the synthesis and characterization of the solid solution $La_3Pd_{4-x}Fe_xGe_4$ ($x$ = 0.7, 1.0, 1.5, 2.0, 3.0, 4.0) is presented. The goal was to investigate, if a partial substitution of Pd by Fe is possible and if this enhances the critical temperature of the superconducting parent compound. Since iron should

prefer a tetrahedral coordination, it was expected that the substitution of the Pd(2) atom should be favored. A comparison of the transition metal–germanium distances in the La$TM_2Ge_2$ compounds shows that the Fe–Ge distance is slightly shorter than the corresponding Pd–Ge distance. This means that the Fe–Ge distance in the tetrahedral layers of iron-substituted $La_3Pd_4Ge_4$ should be shorter, which in turn would lead to an increase of the Pd(1)–Ge(1) distance and the two dimensional character as well.

## 3.2 Synthesis

Samples of the solid solution were synthesized by arc-melting the elements in the desired composition. The preparation of the reagent pellets and a detailed description of the arc-melting process can be found in chapter 2. It has to be noted that the used argon gas of the arc-melting furnace has not been dried and purified for preparing these compounds. The batch size of the experiments was 400 mg and the used current was between 60 A and 70 A. The arc-melting process was performed on both sites of the pellet and the weight loss during arc melting was less than 1 wt%. The obtained melted bullets were ground in an agate mortar and annealed at 1273-1373 K over a period of 4-7 days and if it seemed necessary, several times.

## 3.3 Compositional characterization

All obtained samples where characterized by means of Rietveld refinements from X-ray powder diffraction data and additional EDX measurements. The Rietveld refinements were performed using the TOPAS package. If necessary, an empirical absorption correction with an assumed sample thickness of 0.02 mm was performed. It should be noted that all stated compositions of the samples are nominal compositions and deviate from the effective ones.

The samples with the lowest Fe contents of the series ($x$ = 0.7, 1.0) were annealed once. This led to smaller reflection widths and the disappearance of $LaGe_{2-x}Pd_x$ as impurity phase, which has been identified by indexing the diffraction data and is isotypic to $LaGe_{1.33}Fe_{0.67}$ ($AlB_2$-type structure) (see section 3.6). Nevertheless, the samples still contained some $La_2O_3$ and $LaPd_2Ge_2$ ($x$ = 0.7), as well as Fe and Pd ($x$ = 1.0). The Rietveld refinements were performed with a free Pd:Fe ratio on both transition metal atom positions and showed that in both samples only the Pd(2) positions are occupied by Fe atoms, however the effective Fe content is lower than the nominal one. The refined compositions are $La_3Pd_{3.64(2)}Fe_{0.36(2)}Ge_4$ ($x$ = 0.7) and $La_3Pd_{3.36(2)}Fe_{0.64(2)}Ge_4$ ($x$ = 1.0). The effective doping levels have also been confirmed by at least 5 EDX measurements of each sample showing deviations smaller than 1 % from the refined compositions. With increasing nominal iron content, it becomes more difficult to make clear statements of the effective compositions. This is either due to unidentified impurity phases ($x$ = 1.5) or that the targeted compound occurs in only small amounts ($x$ = 2.0 sample only 22 wt %, with $LaGe_{2-x}Pd_x$ being the main phase). Additional annealing steps did not lead to sample quality improvements. The refinement of nominal $La_3Pd_{2.5}Fe_{1.5}Ge_4$ with an refined $x$ of 0.94 leads to a mixed occupancy of both the Pd(2) and the Pd(1) positions with Fe atoms (0.7 : 0.24 ratio), but there is a quite large deviation in the EDX measurements with an averaged composition of $La_3Pd_{2.97}Fe_{0.81}Ge_{4.2}$. Since for nominal $LaPd_2Fe_2Ge_4$ the Rietveld refinement is only of limited reliability because of the large amount of impurities, only the comparison of the obtained lattice parameters gives hints about the effective composition. The lattice parameters are close to that of nominal $LaPd_{2.5}Fe_{1.5}Ge_4$ so that a similar doping level is assumed for the obtained $U_3Ni_4Si_4$-type product (see Table 3.2). For the samples with the highest doping levels ($x$ = 3.0 and 4.0), the targeted compounds did not emerge at all. Here, $LaGe_{2-x}Pd_x$, $LaFe_2Ge_2$ and $La_2O_3$ were the main components of the obtained mixture. The cell parameters of $La_3Pd_4Ge_4$ and the series $La_3Pd_{4-x}Fe_xGe_4$ ($x$ = 0.7-2.0) are listed in Table 3.2. With increasing $x$ the unit cell decreases along $a$ and $b$ but increases along $c$. The cell volume decreases

slightly with increasing Fe content. The development of the unit cell parameters shows that the effective doping levels increase with the nominal ones. The refined Fe content as well as the identified impurities are summarized in Table 3.2.

**Table 3.2:** Cell parameters and sample quality of $La_3Pd_{4-x}Fe_xGe_4$ ($x$ =0.0-2.0).

| $La_3Pd_{4-x}Fe_xGe_4$ | Refined $x$ | $a$ [pm] | $b$ [pm] | $c$ [pm] | $V$ [Å3] | Impurities |
|---|---|---|---|---|---|---|
| $x$ = 0 [102] | --- | 422.9(1) | 438.2(1) | 2501.1(1) | 463.49(5) | --- |
| $x$ = 0.7 | 0.36 | 419.7(1) | 437.3(1) | 2507.6(1) | 460.30(3) | $La_2O_3$, 7 wt%; $LaPd_2Ge_2$, 3 wt% |
| $x$ = 1.0 | 0.64 | 418.2(1) | 435.1(1) | 2512.0(1) | 457.09(3) | Pd, 4 wt%; Fe, 3 wt%; $La_2O_3$, 3 wt% |
| $x$ = 1.5 | 0.94 | 421.2(1) | 432.7(1) | 2518.1(2) | 458.89(6) | $La_2O_3$, 12 wt%; Fe, 3 wt%; x % unidentified |
| $x$ = 2.0 | 0.92 | 421.3(1) | 431.3(1) | 2519.5(1) | 457.84(5) | $LaGe_{2-x}Pd_x$, 68 wt%; Fe, 7 wt%; $La_2O_3$, 4 wt% |

A single crystal of good quality was selected from the $LaPd_{3.3}Fe_{0.7}Pd_4$ sample. The crystallographic data is summarized in Table 3.3. The refined composition matches the one from the Rietveld refinement. The obtained interatomic distances show that doping with Fe does not lead to a significant increase of the Pd(1)–Ge(1) distance (249 pm to 250 pm), meaning the distance between the $AlB_2$ units and the $BaAl_4$ building blocks remains unchanged. Likewise, the metal- germanide distances within the tetrahedra remain more or less unchanged (there is a minimal decrease along *a* and a minimal increase along *b*).

From the results of the Rietveld refinements and the single crystal analysis it can be summarized that a partial substitution of Pd by Fe in $La_3Pd_{4-x}Fe_xGe_4$ is possible, although the nominal doping levels cannot be achieved. For low doping

concentrations, iron prefers the tetrahedral coordination instead of a trigonal planar environment. An increasing Fe content leads to a slight decrease of the *a* and *b* lattice parameters and an increase of the *c* lattice parameters, but this does not change the interatomic distances drastically. This means that the structural conditions remain more or less unchanged upon Fe doping. The question if the changed charge carrier concentration due to Fe doping leads to a change of the physical properties is presented in the next section.

**Table 3.3**: Crystallographic data of $La_3Pd_{3.66}Fe_{0.34}Ge_4$.

| | |
|---|---|
| Nominal composition | $La_3Pd_{3.3}Fe_{0.7}Ge_4$ |
| Refined composition | $La_3Pd_{3.66(2)}Fe_{0.34(2)}Ge_4$ |
| Temperature | 293 K |
| Diffractometer | STOE IPDS |
| Radiation | Mo $K_\alpha$, λ = 0.71073 Å |
| Space group | *Immm* (79) |
| Lattice parameters | *a* = 418.05 (8) pm; *b* = 439.61 (9) pm; *c* = 2510.6 (5) pm |
| Cell volume | 0.4614(2) $Å^3$ |
| Z | 2 |
| Calculated density | 8.03 $g/cm^3$ |
| Absorption coefficient | 33.75 $mm^{-1}$ |
| 2*θ* range | 7.50 – 65.6 |
| Reflections (total) | 3321 |
| Reflections (independent), | 538 |
| Reflections with I > 2σ(I) | 387 |
| Refined Parameters | 26 |
| $R_{int}$, $R_\sigma$ | 0.118, 0.063 |
| *R*1, *wR*2 [I > 2σ(I)] | 0.030, 0.059 |
| *R*1, *wR*2 [all data] | 0.048, 0.064 |
| Goodness of fit (GooF) | 0.862 |
| Largest resid. peak, hole | 2.173 e/$Å^3$, -2.053 e/$Å^3$ |

Atomic parameters, with atomic displacement parameters U in $pm^2$:

| | | | | |
|---|---|---|---|---|
| La(1) | 2*a* (0,0,0) | | occ. 1 | $U_{11}$ = 68(3); $U_{22}$ = 74(4); $U_{33}$ = 92(3) |
| La(2) | 4*j* (½, 0, *z*) | *z* = 0.3517 (1) | occ. 1 | $U_{11}$ = 76(3); $U_{22}$ = 78(3); $U_{33}$ = 77(2) |
| Pd(1) | 4*j* (½, 0, *z*) | *z* = 0.0977(1) | occ. 1 | $U_{11}$ = 154(3); $U_{22}$ = 53(3); $U_{33}$ = 71(3) |
| Pd(2) | 4*i* (0, 0, *z*) | *z* = 0.2501(1) | occ. 0.83(1) | $U_{11}$ = 93(4); $U_{22}$ = 103(4); $U_{33}$ = 83(3) |
| Fe | 4*i* (0, 0, *z*) | *z* = 0.2501(1) | occ. 0.17(1) | $U_{11}$ = 93(4); $U_{22}$ = 103(4); $U_{33}$ = 83(3) |
| Ge(1) | 4*j* (½, 0, *z*) | *z* = 0.1974(1) | occ. 1 | $U_{11}$ = 101(3); $U_{22}$ = 113(4); $U_{33}$ = 71(3) |
| Ge(2) | 4*i* (0, 0, *z*) | *z* = 0.4502(1) | occ. 1 | $U_{11}$ = 153(5); $U_{22}$ = 58(5); $U_{33}$ = 55(3) |

Interatomic distances:

| | | |
|---|---|---|
| Ge(2)–Pd(1) | 250.5(1) pm | 2x |
| Pd(1)–Ge(1) | 250.3(2) pm | 1x |
| Ge(1)–Pd(2)/Fe | 256.4(1) pm | 2x along *b* |
| Ge(1)–Pd(2)/Fe | 247.3(1) pm | 2x along *a* |
| Ge(2)–Ge(2) | 250.2(1) pm | 1x |
| Pd(2)/Fe–Pd(2)/Fe | 303.3(1) | 4x |
| Ge(1)–Ge(1) | 991.2(1) pm | 1x along *c* |

Interatomic angles:

| | | |
|---|---|---|
| Ge(1)–Pd(2)/Fe–Ge(1) | 105.97(2)° | 4x |
| | 115.38(5)° | 1x |
| | 118.06(5)° | 1x |

## 3.4 Physical Properties

The electrical resistance of the samples with nominal doping levels of $x$ = 0.7, 1.0 and 1.5 has been measured between 10 K and 300 K. The relative change of the resistance with temperature ($R$ / $R_{300K}$) is shown in Figure 3.2. All samples showed a slight decrease of the resistance with decreasing temperature, which is typical for metallic compounds. The measured resistivity values $\rho_{s(300K)}$ ranged between $2.7 \cdot 10^{-5}$ Ωm ($x$ = 0.7) and $2.8 \cdot 10^{-4}$ Ωm ($x$ = 1.5) and are characteristic for poor metal conductors. With increasing doping levels, the samples became poorer electrical conductors, since the resistivity $\rho_{s(300K)}$ is increased and the relative decrease of resistance with temperature is smaller. This is probably due to grain boundary effects and / or an increased amount of non-conducting impurities ($La_2O_3$).

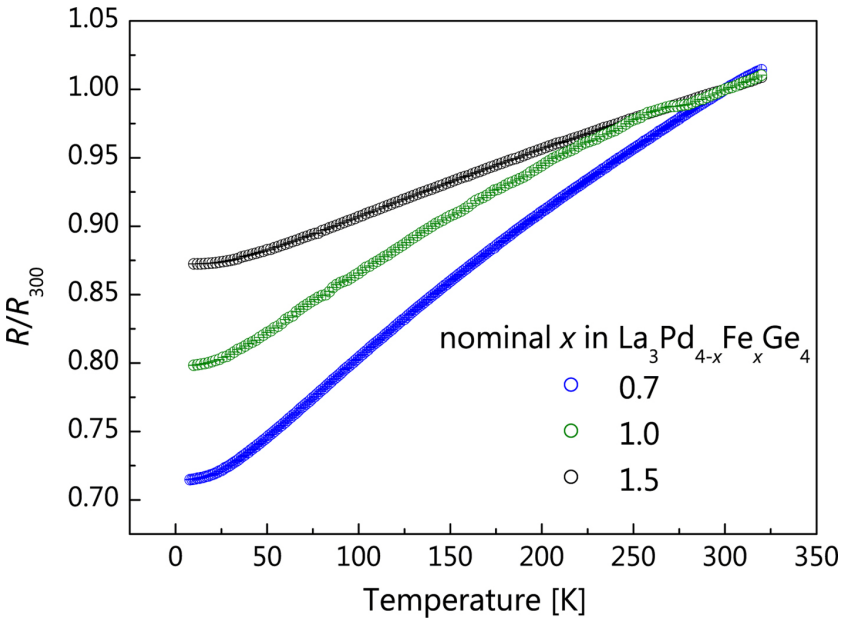


**Figure 3.2:** Electrical resistivity versus temperature for $La_3Pd_{4-x}Fe_xGe_4$ ($x$ = 0.7 – 1.5).

Because no superconducting transition has been observed down to 10 K, additional magnetic measurements were performed down to a temperature of 1.8 K (for $x$ = 0.7 and 1.5). Figure 3.3 depicts the $\chi$ vs. $T$ plot for the $x$ = 0.7 sample. The magnetic susceptibility is nearly temperature independent (Pauli paramagnetic), as one would expect for metallic compounds. No superconducting

signal has been detected over the whole temperature range. The measured susceptibilities are well above the ones expected for metals. This increase of the magnetic signal is probably due to small amounts of ferromagnetic impurities (iron) in the $x$ = 0.7 sample. Since the $x$ = 1.5 sample contains large amounts of Fe as impurity (3 wt%), the susceptibility was empirically corrected to $\chi_{mol} = \Delta M/\Delta H$ = ($M_{mol}$ (20 kOe) – $M_{mol}$ (10 kOe)) / (2 kOe – 1 kOe). This correction takes into account, that at an external magnetic field of 10 kOe, the ferromagnetic impuritiy is already saturated (as obtained from isothermal magnetization measurements). The obtained diagram is displayed in the inlay of Figure 3.3. The amount of elemental Fe in the $x$ = 1.5 sample was estimated from the saturation moment of the isothermal magnetization measurement to be ~ 4 %, which is consistent with the result from the Rietveld refinement.

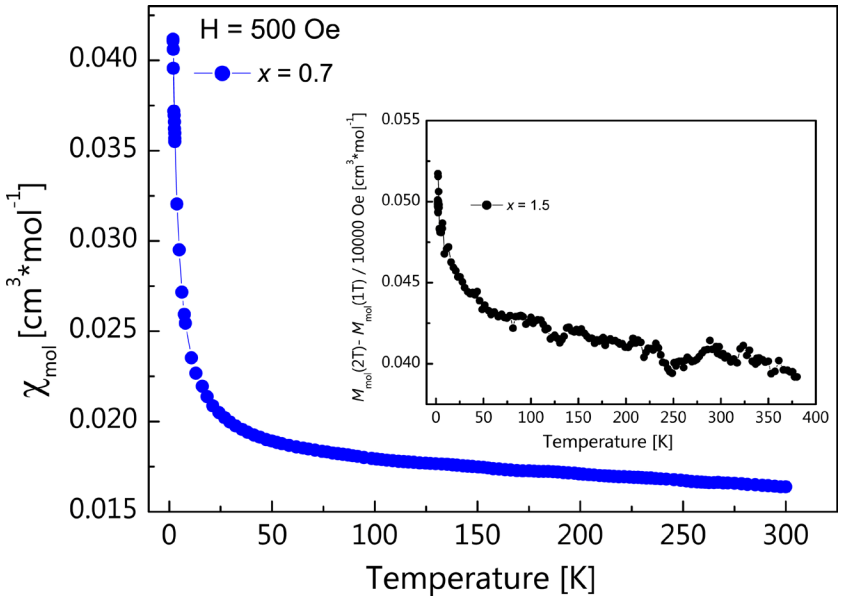


**Figure 3.3:** Susceptibility versus temperature for $La_3Pd_{4-x}Fe_xGe_4$ ($x$ = 0.7 and 1.5 (inlay)).

## 3.5 Conclusion

It was shown that a partial substitution of Pd by Fe in $La_3Pd_4Ge_4$ is possible and that iron prefers the tetrahedral coordinated metal position for low doping concentrations. However, the structural changes and the change of the interatomic distances upon iron doping remain small. This means that the distance between the $BaAl_4$ type units and the $AlB_2$-type is still very small and a three-dimensional character of the structure is supposed. Futhermore doping with iron leads to a less distinctive metallic character and even seems to destroy the superconducting properties of the parent compound $La_3Pd_4Ge$, since no superconducting transition has been observed in the obtained samples.

## 3.6 Synthesis of $LaGe_{1.33}Pd_{0.67}$

As mentioned above, prior annealed samples and samples with high nominal *x* of the series $La_3Pd_{4-x}Fe_xGe_4$ often contained a hexagonal product as impurity phase. The indexed diffraction pattern (cell parameters *a* = 431.0 pm; c = 423.9 pm) was compared with entries in the JCPDS-database[65, 66] but no matching compound was found. Since the indexed cell parameters were very close to listed $LaGe_{1.33}Fe_{0.67}$ (spacegroup *P6/mmm*, $AlB_2$- structure, *a* = 422.3 pm; *c*= 431.6 pm))[105] the Rietveld refinements were performed under the assumption that the hexagonal byproduct could be isotypic $LaGe_{1.33}Pd_{0.67}$, which led to a good explanation of the recorded diffraction patterns. To prove this assumption and the existence of the hexagonal La-Pd-Ge $AlB_2$-type compound, $LaGe_{1.33}Pd_{0.67}$ was tried to be obtained as single product.

### 3.6.1 Synthesis

$LaGe_{1.33}Pd_{0.67}$ was synthesized by arc melting (I = 60 A) the elements in the desired composition using the procedure described above.

### 3.6.1 Characterization

The Rietveld analysis of the arc-melted sample showed, that the desired $LaGe_{2-x}Pd_x$ (*P6/mmm*, $AlB_2$-type) was the main component of the obtained mixture (87 wt %) with $LaPd_2Ge_2$ (8 wt%) and $La_2O_3$ (5 wt%) being impurity phases. Since the diffraction signals of the main phase were broadened a certain phase width of $LaGe_{2-x}Pd_x$ was assumed, which could probably be narrowed by additional annealing steps. The refined composition was $LaGe_{1.28(1)}Pd_{0.72(1)}$ and the cell parameters were refined as $a$ = 432.1(1) pm and $c$ = 422.7(1) pm The diffraction pattern and the obtained crystal data from the Rietveld refinement can be found at the appendix. Additional EDX measurements showed an averaged composition of $La_{1.25}Pd_{0.66}Ge_{1.33}O_{0.56}$ (the excess of La and O is probably due to $La_2O_3$ impurities).

The successful synthesis of $LaGe_{2-x}Pd_x$ is the first example of a La-Pd-Ge compound crystallizing in the $AlB_2$-type structure and was helpful for the refinement of the diffraction patterns of the $La_3Pd_{4-x}Fe_xGe_4$ series.

# 4 Synthesis and physical properties of ZrTiAs and $Zr_{1+x}V_{1-x}As$

## 4.1 Structural details and motivation

Since the interplay of the crystal structure and physical properties is one of the crucial questions of solid state chemistry, a structure prediction tool can be a helpful device for the synthesis of new compounds crystallizing in known structure-types. Such a tool, a structure map, was presented in 2000 for metal-rich pnictides and chalcogenides $M_2Q$ (including the ternaries $M_{2-x}M_x'Q$)[106]. In 2001 and 2002 this semi empirical structure map was used to successfully predict the structures of ZrTiAs and ZrVAs (Zr*M*As), respectively[107, 108]. Both compounds crystallize in the tetragonal space group *I*4/*mmm* forming the CeScSi-type structure, which is the ordered variant of the $LaSb_2$ – type[109-111]. The main structural motifs of the Zr*M*As compounds are As – centered tri-capped trgional prisms, where As is surrounded by 5 Zr and 4 *M* atoms, and empty distorted $Zr_2M_4$ octahedra whose faces are capped by As (see Figure 4.1).

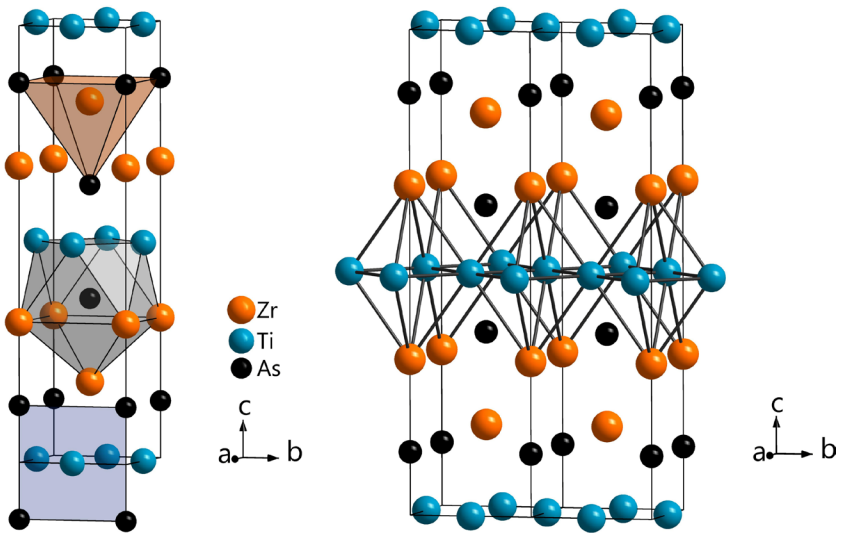


**Figure 4.1:** Crystal structure of Zr*M*As emphasizing the filled polyhedra (left) and the empty $Zr_2M_4$ octahedra which are interconnected via common corners (right).

The trigonal prisms are connected via common faces (forming linear chains parallel to [100]) and via common edges, leading to a three-dimensional structure[107]. The 3*d* metal atoms *M* occupy the Wykoff position 4*c* ((0, ½, 0); see Table 4.1 and Figure 4.1) and form *M*-*M* square nets within the *ab*-plane. Similar to the structures of the iron arsenide superconductors, the 3*d* metal atoms are surrounded by 4 As atoms, though forming distorted square planes instead of tetrahedra. The Zr atom is surrounded by 5 As atoms inside a distorted square pyramide. The structure is stabilized through strong *M*–*M*, Zr–As and *M*–As bonds as well as intermediate Zr–*M* and weaker Zr–Zr interactions[108].First principle calculations proposed a metallic character of both compounds and showed that the states around the Fermi Energy are mainly composed of Zr and *M d* states. Furthermore crystal orbital Hamiltonion populations calculations (COHP) revealed that only bonding states are filled, though ZrVAs being on the border were antibonding V-V states occur[107, 108].

**Table 4.1:** Crystal parameters of ZrTiAs[a] and $Zr_{0.85}V_{1.15}As$[b] [107, 108].

| | | | | | |
|---|---|---|---|---|---|
| Spacegroup | | *I*4/*mmm* (139), *Z* = 4 | | | |
| Lattice parameters [pm] | | ZrTiAs: *a* = 379.3(1); *c* = 1480.2(3), *V* = 212.9(1) | | | |
| and cell volume [Å$^3$] | | $Zr_{0.85}V_{1.15}As$: *a* = 375.8(1); *c* = 1400.2(3), *V* = 197.7(1) | | | |
| **Atom** | **Site** | ***x*** | ***y*** | ***z*$^a$** | **z$^b$** |
| Zr | 4*e* | 0 | 0 | 0.32097(6) | 0.3270(1) |
| *M* | 4c | 0 | ½ | 0 | 0 |
| As | 4*e* | 0 | 0 | 0.13029(7) | 0.1290(1) |

The goal was to synthesize ZrTiAs and ZrVAs to reveal their physical properties. Since a phase range of $Zr_{1+x}V_{1-x}As$ (-0.15 ≤ x ≤ 0.43) was reported[108], samples with *x* = 0.20, 0.25, 0.35 and 0.50 were synthesized to investigate if this *direct hole-doping* of the VAs-layers changes the physical properties of the parent compound ZrVAs. Despite the three-dimensional character of the CeScSi-type structure, common features to the structures of the iron arsenid superconductors can be seen in the coordination of the 3*d* metal, which is coordinated by 4 As atoms, and

the strong interactions between the 3*d* metal atoms. If these common features are sufficient for similar properties will be shown in the following chapter.

## 4.2 Synthesis

According to the desired composition $Zr_{1+x}M_{1-x}As$ the elements were pre-reacted in sealed alumina crucible at 1073 K for 48 h. The as-prepared mixtures were pressed to pellets and arc-melted twice with a current of 25 A. A detailed description of the arc-melting process can be found in chapter 2. The weight loss during arc melting was less than 1 wt%.

## 4.3 Sample quality

Samples of high quality were obtained for ZrTiAs and the series $Zr_{1+x}V_{1-x}As$ ($x$ = 0.20 -0.35). No additional phases were detected in the case of ZrTiAs and only small amounts of ZrAs (< 2 wt %) were identified as impurity phase for the V containing samples (additional to some small unidentified peaks for the $x$ > 0 samples). For a nominal $x$ of 0.50, a mixture of $Zr_{1+x}V_{1-x}As$ (with $x$ = 0.29), ZrAs, VAs and some other unidentified compounds was obtained, which is in accordance with the reported maximum of $x$ = 0.43[108]. A single crystal of good quality was selected from the ZrTiAs sample, the obtained crystallographic data can be found at the appendix section. Interestingly the Rietveld refinement of ZrTiAs as well as the single crystal data showed a slight deficiency at the Ti position ($ZrTi_{0.96(1)}As$). This explains the smaller cell parameters compared to literature data (see Table 4.1 and Table 4.2) and could be an interesting effect concerning the physical properties. The refined cell parameters of ZrVAs are well in between the ones published for $Zr_{1.43}V_{0.57}As$ and $Zr_{0.85}V_{1.15}As$ [108].

**Table 4.2:** Refined cell parameters and composition of ZrTiAs and $Zr_{1+x}V_{1-x}As$. Please note that the mixed occupancy in the Zr rich samples (x > 0) is only present at the Wykoff position 4*c* (V site).

| nominal | refined | *a* [pm] | *c* [pm] | *V* [Å$^3$] |
|---|---|---|---|---|
| ZrTiAs | $ZrTi_{0.96(1)}As$ | 376.8(1) | 1474.5(4) | 209.3(1) |
| ZrVAs | $ZrV_{0.98(1)}As$ | 376.8(1) | 1411.7(1) | 200.3(1) |
| $Zr_{1.20}V_{0.80}As$ | $Zr_{1.20(1)}V_{0.80(1)}As$ | 377.4(1) | 1433.3(1) | 204.1(2) |
| $Zr_{1.25}V_{0.75}As$ | $Zr_{1.29(1)}V_{0.71(1)}As$ | 377.0(4) | 1434.2(1) | 203.9(1) |
| $Zr_{1.35}V_{0.65}As$ | $Zr_{1.36(1)}V_{0.64(1)}As$ | 378.2(1) | 1457.4(2) | 208.4(1) |

The Rietveld refinements of the Zr-rich samples $Zr_{1+x}V_{1-x}As$ ($x$ = 0.20, 0.25, 0.35) showed that the effective compositions deviate only slightly from the nominal ones. The Zr:V ratio was allowed to be refined freely on both metal sites, but a Zr / V mixed occupancy is only present at the Wykoff position 4*c*. It is notable that the unit cell parameters are drastically increased for $x$ = 0.35 compared to lower Zr concentrations, but are still smaller than for reported $Zr_{1.43}V_{0.57}As$ ($a$ = 382.4(1) pm, $c$ = 1486.8(6) pm)[108]. This means that the unit cell parameters do not increase linearly with the Zr concentration. Complete crystal data can be found at the appendix.

## 4.4 Physical properties

Resistivity and susceptibility measurements of Zr*M*As confirmed the proposed metallic character of these metal rich arsenides. As one can see from Figure 4.2 the resistivity of the samples decreases with decreasing temperature and the susceptibility shows a nearly temperature independent (Pauli paramagnetic) behavior, typical for metallic compounds (see appendix for the magnetic measurements). The measured resistivity values $\rho_{s(300K)}$ of $2.4 \cdot 10^{-5}$ Ωm (ZrTiAs) and $2.7 \cdot 10^{-6}$ Ωm (ZrVAs) are characteristic for poor metal conductors, but the resistivity of ZrVAs is one order of magnitude smaller than the typical values obtained for the iron arsenide parent compounds.

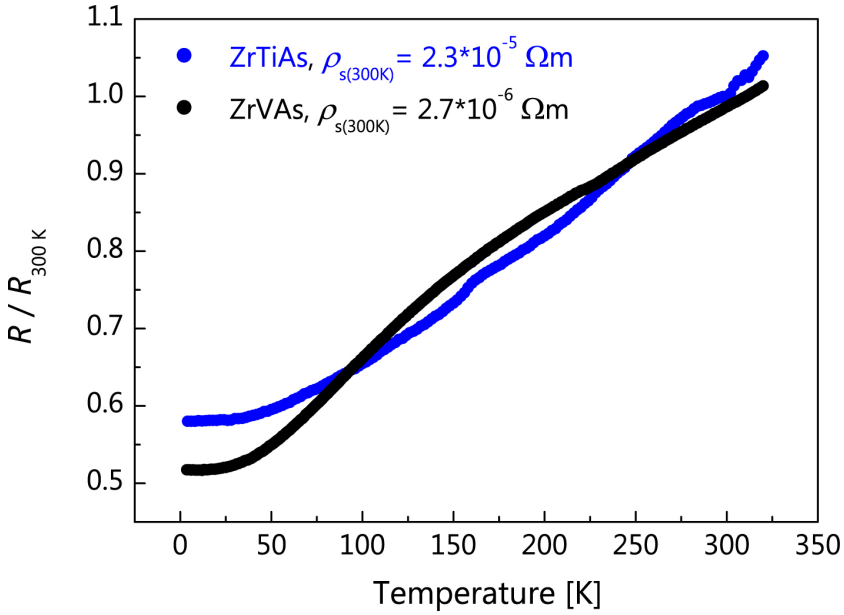


**Figure 4.2:** Electrical resistivity versus temperature for ZrTiAs and ZrVAs.

The resistivity measurement of $Zr_{1.25}V_{0.75}As$ showed a sudden drop of the resistance value at a temperature of about 4 K, which could have been indicative for a superconducting transition (Figure 4.2). However, magnetic measurements of the sample revealed that the superconducting volume fraction (SVF) is only as small as 0.8 % (Figure 4.4) and the critical fields of the superconducting phase are as low as ~ 1000 Oe. Similar critical temperatures and small SVFs have also been found for the other Zr rich samples ($x$ = 0.20 and 0.35), so that it is most likely that the superconducting behavior originates from unidentified binaries like $V_{0.987}Zr_{0.013}$, which is known to show a superconducting transition at a comparable $T_c$[112]. The increased $\rho_{s(300K)}$ value of $Zr_{1.25}V_{0.75}As$ ($2.4 \cdot 10^{-5}$ Ωm) compared to the one of ZrVAs is probably due to an increased amount of impurities and / or a higher disorder in the V layers due to Zr doping.

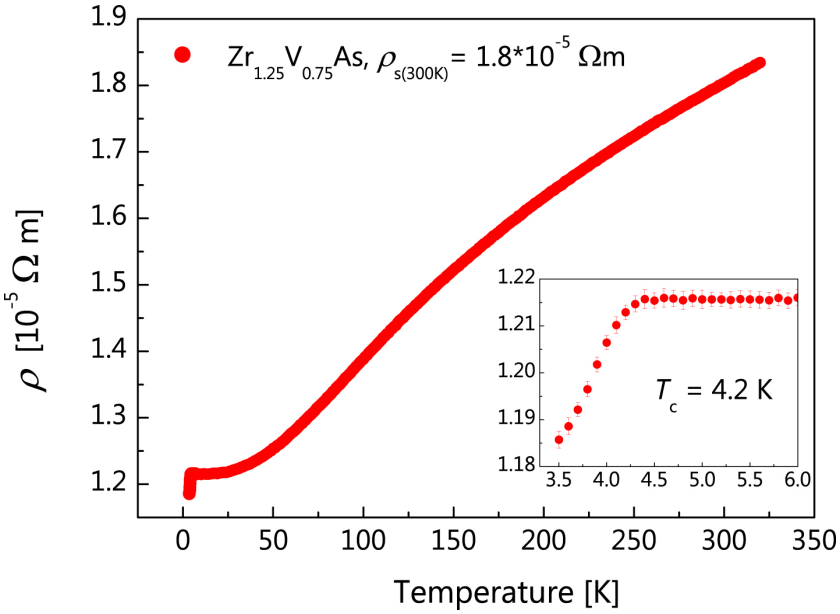


**Figure 4.3:** Electrical resistivity versus temperature for $Zr_{1.25}V_{0.75}As$. Inlay: low temperature regime between 3.5 K and 6.0 K.

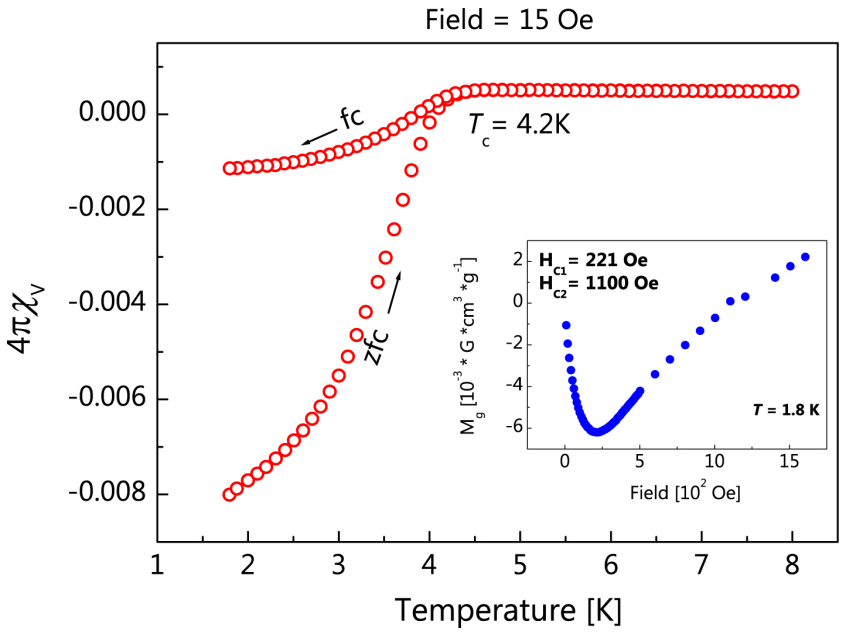


**Figure 4.4:** Magnetic measurements of $Zr_{1.25}V_{0.75}As$. Red: zero-field-cooled and field-cooled susceptibility measurement with an applied of 15 Oe. Inlay: Field dependent magnetization measurement at 1.8 K with detected critical fields of 221 Oe and 1100 Oe.

## 4.5 Conclusion

The metal rich arsenides ZrTiAs and $Zr_{1+x}V_{1-x}As$ ($x$ = 0.20-0.35) have been characterized as metallic compounds which can be obtained by arc melting pre-reacted mixtures of the elements. Decreasing the valence electron concentration in ZrVAs by additional Zr (direct hole-doping of the VAs-layers) does not lead to a significant change of the physical properties. The metallic character is only slightly decreased upon Zr doping, as can be seen from the measured $\rho_{s(300K)}$ value of $Zr_{1.25}V_{0.75}As$, which is probably due to an increased disorder within the VAs-layers. No anomaly in the resistivity or magnetic measurements has been detected, what could have been indicative for similar structural or magnetic transitions as found for some parent compounds of the iron arsenide superconductors.

# 5 Synthesis of $LaFeAsO_{1-x}F_x$ via solid state metathesis reaction

*Parts of this chapter are published in:* R. Frankovsky, A. Marchuk, R. Pobel, D. Johrendt, *Solid State Communications* **2012**, *152*, 632.
Doi: 10.1016/j.ssc.2011.11.028
http://www.sciencedirect.com/science/article/pii/S0038109811006326


## 5.1 Motivation

One way to think about new compounds is to simply replace atom fragments by isoelectronic ones. In 2009, this has been successfully achieved by finding the new superconducting compounds $Sr_2ScO_3FeP$ ($T_c$ = 17 K) and $Sr_2VO_3FeAs$ ($T_c$ = 37 K), which consist of two-dimensional iron-pnictide tetrahedral layers, separated by perovskite-like metal oxide interlayers[33, 113]. These compounds have been derived from known compounds containing CuS layers[114, 115] instead of the iron pnictide layers and were the first representatives of the so-called 21311 iron pnictide superconductor family. Going the other way round, Ubaldini *et al.* presented the oxycoppersulfide superconductor $BiOCu_{1-x}S$ ($T_c$ = 5.8 K) with ZrCuSiAs-type structure and which is therefore isostructural to LaFeAsO[116]. It has to be noted that the parent compound BiOCuS has already been known since 1994[117]. To possibly enhance the critical temperature of the bismuth compound, the goal was to synthesize the analogue iron arsenide compound BiOFeAs. Indeed, with a phenomenological relation between $T_c$ and competing instabilities a $T_c$ as high as 42 K was predicted for hypothetical BiOFeAs[118]. For this reason, enormous efforts have been made to synthesize this possible high temperature superconductor. Since conventional synthesis routes (reaction of binary oxides and / or arsenides

with the elements) did not lead to BiOFeAs, an alternative synthesis route was developed.

One approach to obtain control of solid-state reactions is based on the concept of building blocks developed mainly by Ferey, Yaghi and O'Keeffe[119-121]. It was initially applied to assemble metal-organic frameworks from precursor molecules with fitting structural properties. Infinite two-dimensional building blocks were proposed by Cario *et al.*, who predicted and synthesized transition metal pnictide compounds with the ZrCuSiAs-type structure by solid state metathesis (SSM) reaction [122, 123]. The driving force behind SSM reactions is the formation of stable by-products, often alkaline halides[124], which can easily be removed afterwards. Since the ZrCuSiAs structure is built of alternating fluorite and anti-fluorite-type layers, precursors containing these fragments have been used. As an example, BaFZnP was obtained from BaFCl with flourite-type $(BaF)^+$ building blocks and NaZnP with anti-fluorite-type $(ZnP)^-$-building blocks, giving NaCl as by-product (see Figure 5.1)[122].

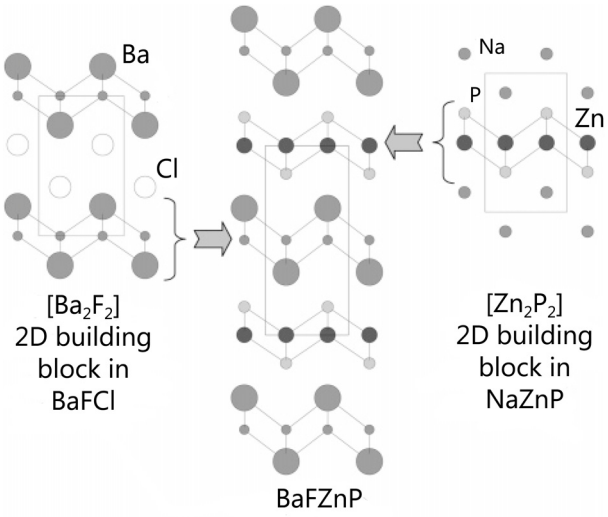


**Figure 5.1:** Structure prediction for BaFZnP on the concept of building blocks. Reprinted with permission from[122]. Copyright 2005 American Chemical Society.

Transferring this concept to the synthesis of BiOFeAs, BiOCl and NaFeAs were chosen as starting materials. However, the obtained samples from the metathesis reactions showed similar compositions like the ones obtained by conventional

synthesis routes and consisted mainly of elemental Bi, FeAs and $Fe_3O_4$. An explanation for the formation of the latter products can be found in the habilitation thesis of P. Schmidt, where an electrochemical series for solid state compounds, valid at high temperatures (700 K -1300 K), was presented[125]. According to this electrochemical series, oxidic compounds with oxidation states of $Fe^{+II}/Bi^{+III}$, which would be the case in BiOFeAs, cannot be obtained by thermodynamic reaction control, since the difference of the electrochemical potential leads to the oxidation of $Fe^{+II}$ and the reduction of $Bi^{+III}$ to form the thermodynamic equilibrium. This is consistent with the observation of Bi, FeAs and $Fe_3O_4$ as main products of the above mentioned syntheses.

Since BiOFeAs could not be obtained via solid state metathesis reaction, it was decided to test the general suitability of this approach for the synthesis of another ZrCuSiAs-type compound, LaFeAsO and the superconducting solid solution series $LaFeAsO_{1-x}F_x$[15]. The synthesis of $LaFeAsO_{1-x}F_x$ by classical solid-state reactions leads to samples with relatively high amounts of impurity phases (mainly LaOF)[15, 126]. Therefore, another purpose of using this alternative synthesis approach was to optimize the product quality.

For the synthesis of LaFeAsO, LaOCl and NaFeAs were used as starting materials. Following the concept of Cario, LaOCl contains the fluorite-type units $(LaO)^+$ and NaFeAs contains the anti-fluorite-type units $(FeAs)^-$, meaning the two structural motifs of LaFeAsO ($OLa_{4/4}$ – and $FeAs_{4/4}$- tetrahedral layers) are already present in the starting materials. In other words, combining the PbFCl- type structure (LaOCl) with the anti-PbFCl-type structure (NaFeAs) formally leads to the formation of a filled variant of the PbFCl-type structure (ZrCuSiAs – type, LaFeAsO). Figure 5.2 illustrates the general synthesis pathway, where the high lattice energy of NaCl is expected to shift the equilibrium to the desired product. From this scheme one may assume that the product formation could be topotactic, that is without bond cleavage in the LaO- and FeAs-layers of the precursors. To what extent this assumption is true, and whether the physical properties of the products differ from those obtained by classical methods will also be shown in this chapter.

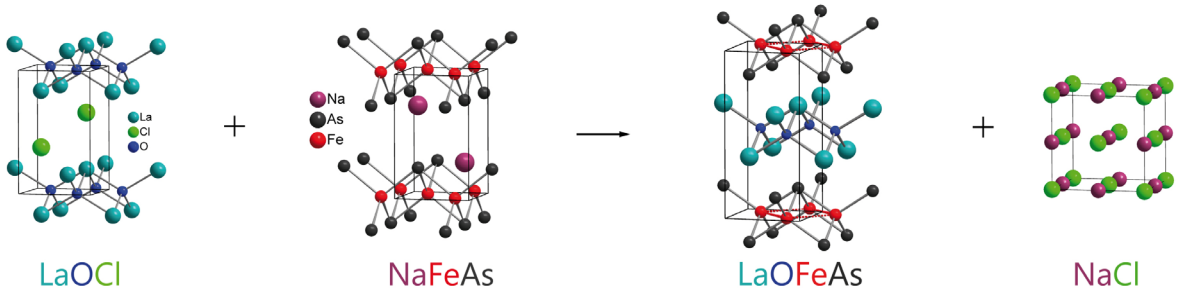


**Figure 5.2:** Scheme of the SSM reaction using the concept of building blocks.

## 5.2 Synthesis

According to the scheme illustrated in Figure 5.2, LaFeAsO was synthesized by heating LaOCl and NaFeAs in a molar ratio of 1:1. In a first three-step attempt, the reaction mixture was heated to 1023, 1123 and 1223 K and reacted for 48 h, respectively. The mixture was cooled down and well homogenized between each step. As can be seen in Figure 5.3, the amount of the desired product was increased with each reaction step. The formation of the binary arsenides LaAs and $Fe_2As$ after the primary heating treatment was a first hint that the reaction pathway does not follow a topotactic route.

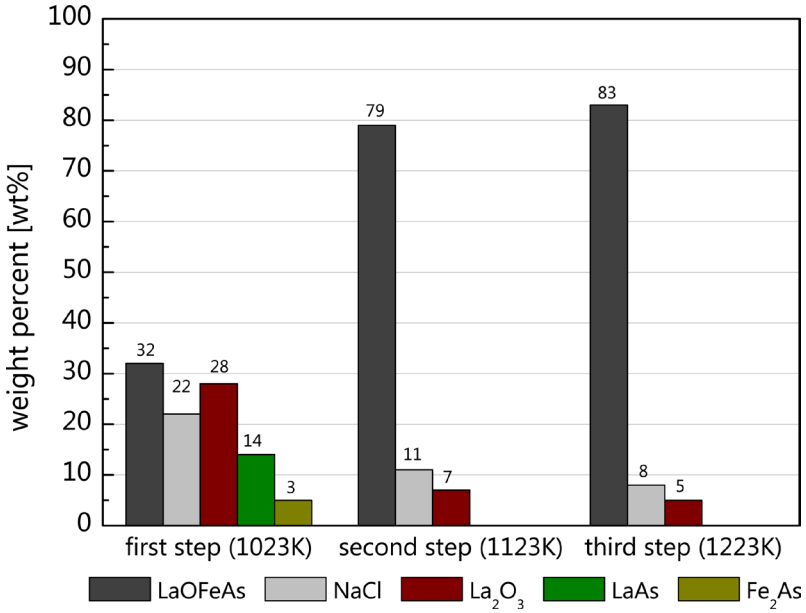


**Figure 5.3:** Composition of the reaction mixture after different reaction steps of the synthesis optimization process.

Combining these three steps to a one-step synthesis led to the temperature program, which generally was used to synthesize 1111 compounds of the La-Fe-As-O system via the metathesis route. The mixtures therefore were heated to 1023 K for 48h, followed by heating to 1223 K and reaction for 96 h. To remove the co-formed salts NaCl and NaF, the obtained mixtures were washed with water (three times) and ethanol, followed by drying the product under high vacuum. For the synthesis of the $LaFeAsO_{1-x}F_x$ ($x$ = 0.05, 0.10, 0.15) series, stoichiometric amounts of LaOCl, NaFeAs, $LaF_3$ and elemental Na were reacted in the one-step synthesis, mentioned above, according to the following reaction equation.

$$(1-x)\ LaOCl + NaFeAs + x\ LaF_3 + x\ Na \rightarrow LaFeAsO_{1-x}F_x + (1-x)\ NaCl + 2x\ NaF$$

The reaction mixtures of the whole series ($x$ = 0-0.15) were heated in the following reaction vessel setup: alumina crucibles, welded in niobium tubes enclosed by silica tubes (see chapter 2 for details).

## 5.3 Reaction pathway

As mentioned earlier, the formation of intermediate binary compounds at lower temperatures raised first doubts about the topotactic character of the reaction. Therefore, the reaction was monitored by means of temperature-dependent X-ray diffraction. A mixture of LaOCl and NaFeAs was sealed in a silica capillary and heated with a rate of 120 K/h on a diffractometer equipped with a high temperature furnace (see chapter 2 for details). The measured diagrams show that the formation of the intermediate binary phases starts at about 973 K, the same temperature where the first reflections of the product (LaFeAsO) appear (Figure 5.4). Hence, the reaction obviously proceeds via intermediate binaries formed by decomposition of the precursors, and is therefore not of topotactic character.

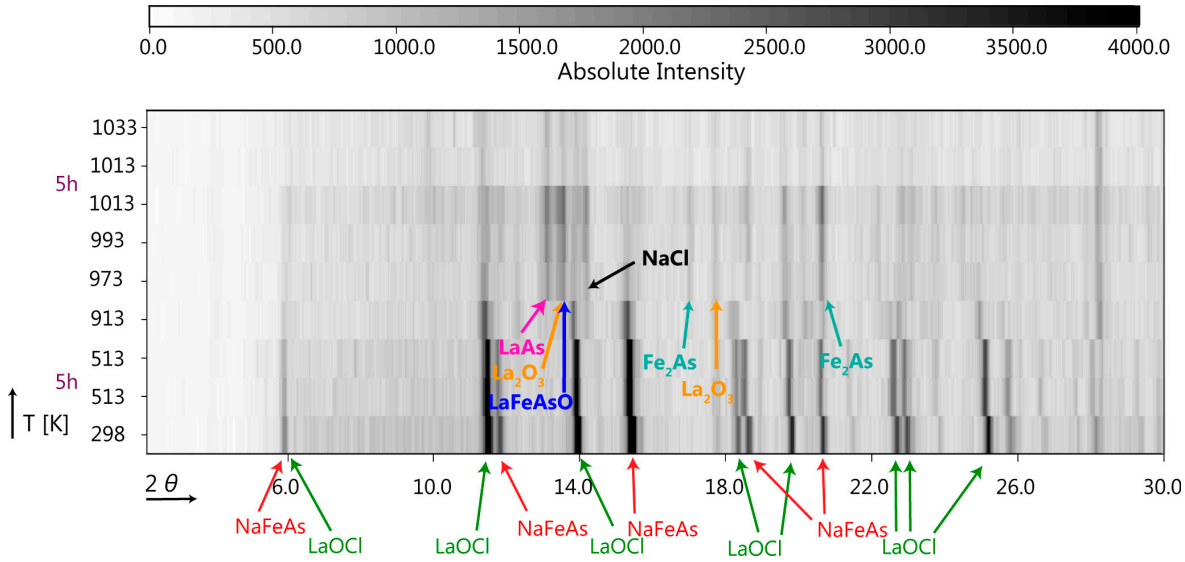


**Figure 5.4:** Temperature-dependent X-ray pattern monitoring the reaction of LaOCl and NaFeAs.

The *in situ* formation of the intermediate binaries quite likely improves the overall homogeneity of the reaction mixture and therefore leads to products of higher purity (as will be shown later in this chapter) compared to conventional synthesis methods.

## 5.4 Sample quality

The phase purity of the obtained samples was checked by Rietveld refinements of powder diffraction patterns (HUBER G670, Cu-$K_{\alpha1}$ radiation and STOE STADI P, Mo-$K_{\alpha1}$ radiation). Since the effective F content cannot be derived from Rietveld refinements or EDX measurements, the O:F ratio was held constant at the nominal composition and the evolution of the lattice parameters was used as indicator of the effective F content in the samples. Empirical absorption corrections were performed, estimating sample thicknesses of 0.02mm (see chapter 2 for details) for patterns recorded with the HUBER diffractometer. As an example, the Rietveld refinements of the $LaFeAsO_{0.9}F_{0.1}$ sample before and after the removal of the by-products are shown in Figure 5.5 (patterns recorded on the HUBER G670 diffractometer).

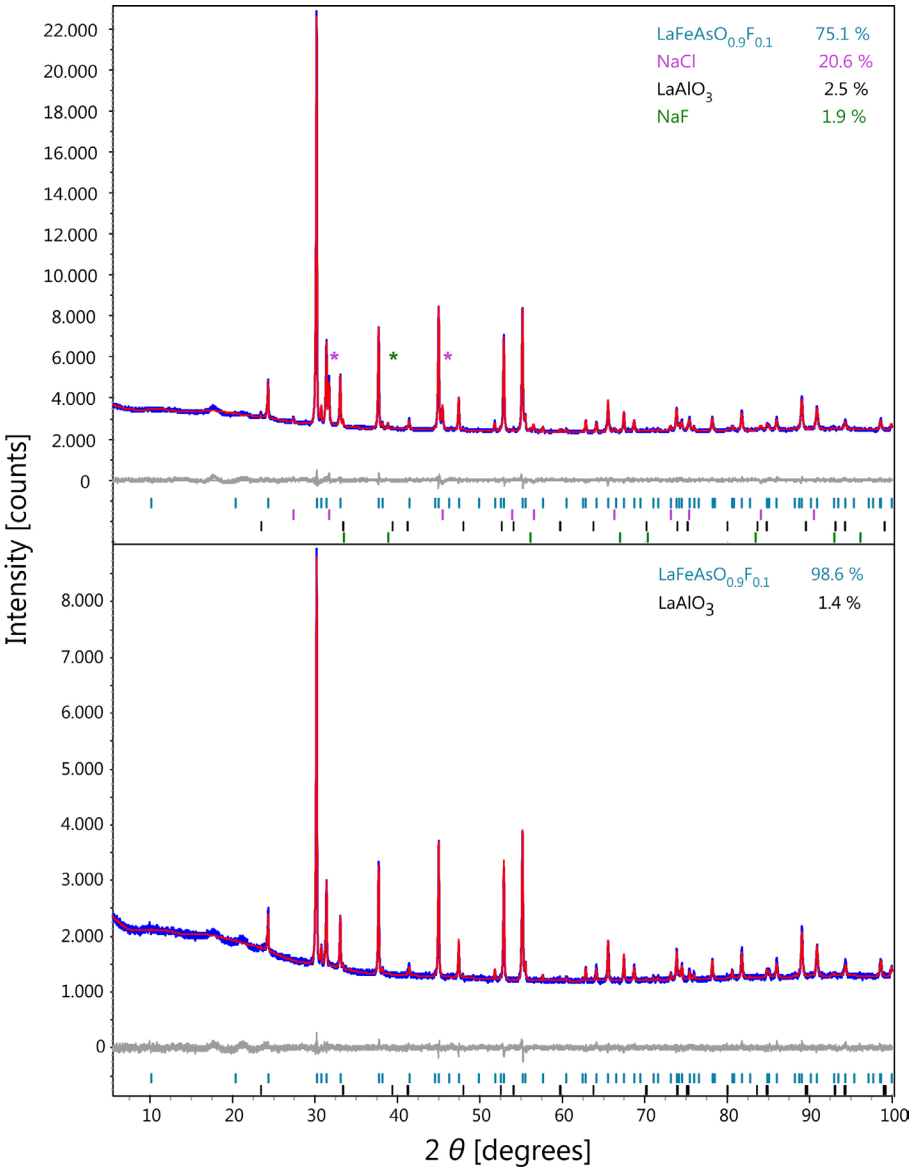


**Figure 5.5:** Rietveld refinement of the $x$ = 0.1 sample, before (above) and after (below) the removal of the co-formed salts NaCl and NaF (main reflections marked with *).

An additional diffraction pattern of higher quality has been recorded for the $LaFeAsO_{0.9}F_{0.1}$ sample (STOE STADI P, Mo-$K_{\alpha1}$, 60 h measuring time) after the removal of the co-formed salts (see Figure 5.6). The corresponding Rietveld refinement revealed traces of LaAs as additional impurity phase. The obtained lattice parameters as well as the identified impurities of the $LaFeAsO_{1-x}F_x$ (x = 0-0.15) series are summarized in Table 5.1 (the data for $LaFeAsO_{0.9}F_{0.1}$ is the one obtained from the STOE STADI P refinement).

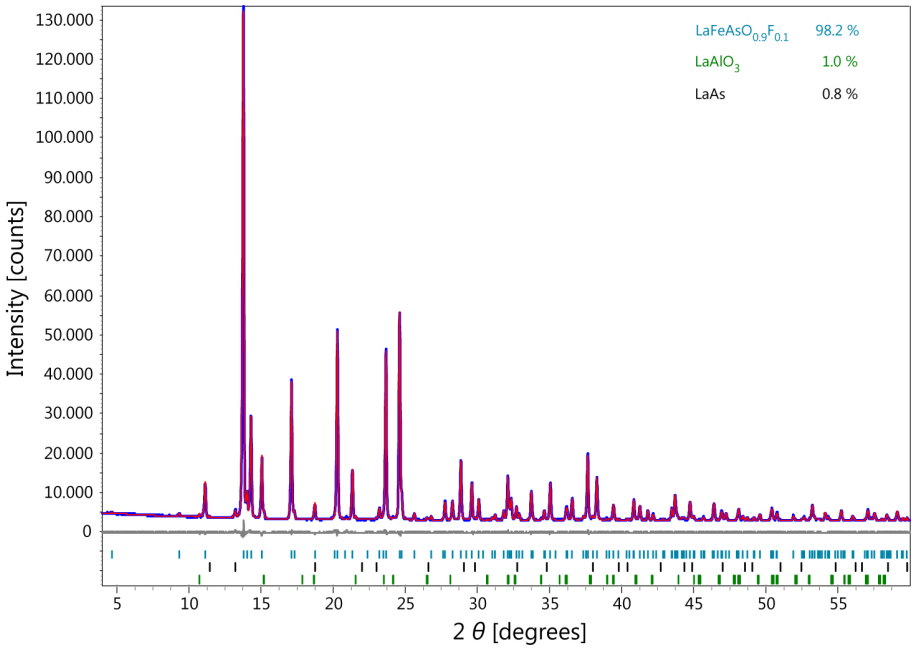


**Figure 5.6:** Rietveld refinement of $LaFeAsO_{0.9}F_{0.1}$ on a long term diffraction pattern (STOE STADI P, Mo-$K_{\alpha1}$, 60 h) after the removal of the co-formed salts NaCl and NaF.

**Table 5.1:** Lattice parameters and sample quality of $LaFeAsO_{1-x}F_x$ synthesized by SSM reaction.

| $LaFeAsO_{1-x}F_x$ | *a* [pm] | *c*[pm] | V [Å$^3$] | Impurities |
|---|---|---|---|---|
| $x$ = 0 | 403.2(1) | 873.8(1) | 142.0(1) | --- |
| $x$ = 0.05 | 402.8(1) | 872.3(1) | 141.6(1) | LaAs, 1.0 wt% |
| $x$ = 0.10 | 402.6(1) | 871.2(1) | 141.2(1) | $LaAlO_3$ 1.0 wt%; LaAs 0.8 wt% |
| $x$ = 0.15 | 402.0(1) | 869.7(1) | 140.6(1) | LaAs 3.5 wt%; $LaAlO_3$ 1.4 wt% |

As expected, the cell volume decreases with increasing fluoride content due to the smaller ionic radius of fluoride compared to oxide. This, in combination with the low content of impurity phases, shows that the effective compositions of the samples are very close to the (or even exact the) nominal ones. Compared to conventional synthesis methods, the amount of impurity phases (FeAs and LaOF)[15, 126] was decreased by using the SSM reaction. The occurrence of the $LaAlO_3$ impurity is due to the reaction with the alumina crucible. Alternative reaction vessel setups did however not improve sample quality.

## 5.5 Physical properties

To check whether the physical properties of the samples prepared by the SSM reaction differ from the ones obtained by conventional methods, electrical resistance as well as low-temperature XRD measurements of LaFeAsO have been performed. Furthermore, magnetic susceptibilities of the $LaFeAsO_{1-x}F_x$ ($x$ = 0.05–0.15) were measured under zero-field-cooled and field-cooled (zfcfc) conditions.

As mentioned earlier, LaFeAsO undergoes a structural phase transition from the tetragonal space group *P*4/*nmm* to orthorhombic *Cmme* at around 160 K ($T_s$) and a magnetic transition to an antiferromagnetic phase at around 140 K ($T_N$) [39, 127]. The low-temperature XRD diagrams of LaFeAsO have been recorded between 180 K and 130 K on a HUBER G670 diffractometer (Co-$K_{\alpha1}$ radiation, equipped with a closed cycle He-cryostat) and were refined with the Rietveld method using the TOPAS package[67]. The development of the lattice parameters with decreasing temperature is illustrated in Figure 5.7. Consistent with earlier publications, a splitting of the lattice parameters *a* and *b* was found below 162 K indicating the structural transition. The lattice parameters were allowed to be refined equal when the difference was < 0.6 pm and a $R_{wp}$ value of at least 1.7 was achieved with equally refined parameters *a* and *b*.

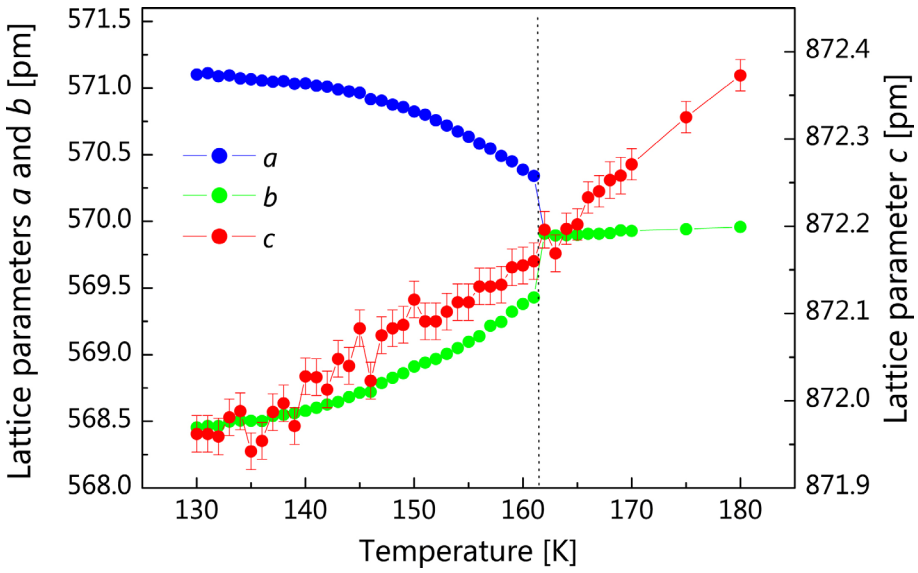


**Figure 5.7:** Development of the lattice parameters of LaFeAsO with temperature, showing the structural transition below ~162 K. Please note that the error bars of *a* and *b* are within the size of the chosen symbols.

As it was first shown by Klauss *et al.*, the structural and magnetic transitions can be observed on the derivation of the electrical resistance d$\rho$/d$T$ [127]. The measurement of the electrical resistance of LaFeAsO is shown in Figure 5.8. As can be seen the structural transition is indicated by a sign change of the first derivation (~ 165 K) and the magnetic transition is observed at its maximum (~ 140K).

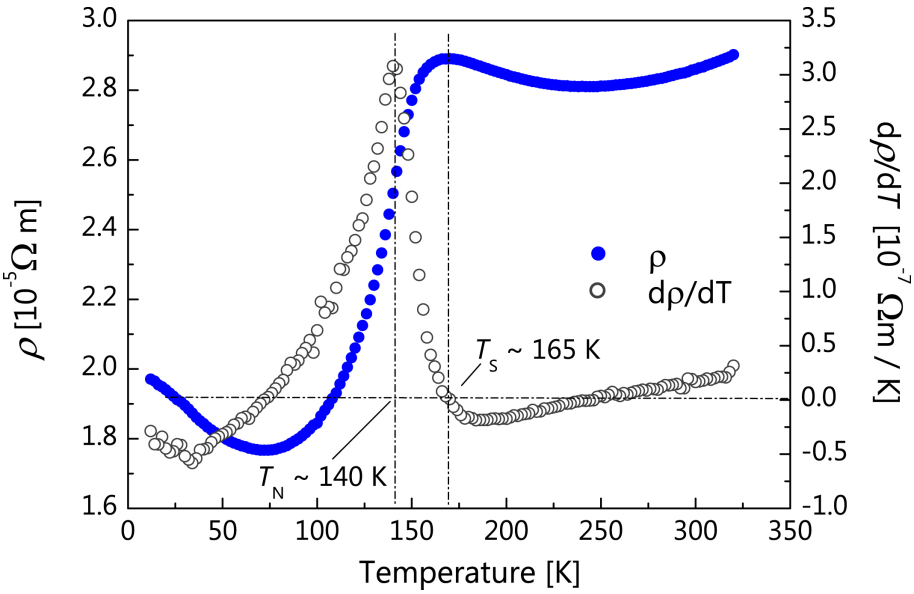


**Figure 5.8:** Temperature dependence of the electrical resistivity $\rho$ of LaFeAsO together with the derivative d$\rho$/d$T$. $T_s$ and $T_N$ mark the strucutral and magnetic phase transition respectively

Results of the magnetic susceptibility measurements are depicted in Figure 5.9. The maximum $T_c$ of 26 K has been detected for $LaFeAsO_{0.9}F_{0.1}$ and bulk superconductivity has been confirmed for the $x$ = 0.10 and 0.15 ($T_c$ = 9 K) samples, but only a small superconducting volume fraction of 4 % has been observed for the $x$ = 0.05 sample ($T_c$= 11 K). Because the latter sample is only on the verge of the superconducting composition ($x$ > 0.04)[126], small changes of the true composition could lead to the loss of the superconducting properties. The paramagnetic susceptibility above $T_c$ is relatively high, indicating possible traces of ferromagnetic impurities. However, the weight fraction of the ferromagnetic impurity was estimated to be less than 0.5 wt% under the assumption that this impurity is metallic iron.

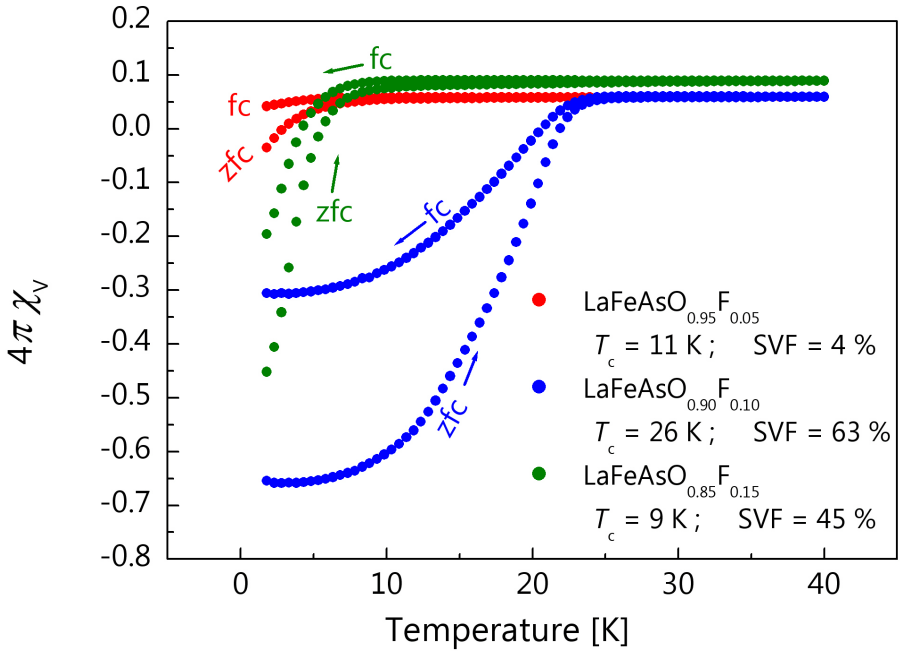


**Figure 5.9:** Zero-field-cooled and field-cooled susceptibility measurements of the $LaO_{1-x}F_xFeAs$ samples with an applied field of 15 Oe.

## 5.6 Conclusion

A new method to synthesize LaFeAsO and superconducting $LaFeAsO_{1-x}F_x$ ($x$ = 0.05, 0.10, 0.15) by solid state metathesis (SSM) reaction has been developed. Samples of high purity have been obtained by using LaOCl and NaFeAs as precursors. Temperature dependent X-ray diffraction shows that the reaction pathway proceeds via decomposition of the precursor to binary intermediates (LaAs, $La_2O_3$, $Fe_2As$) and is thus not of topotactic character, as one may assume at first. Nevertheless, the *in situ* formation of the binary intermediates leads to a better homogeneity of the reaction mixture which improves the phase purity. Superconductivity was confirmed in agreement with conventionally prepared compounds. The results prove the general suitability of the SSM reaction to produce iron based superconductors and may be useful to explore new compounds that are difficult or impossible to synthesize by conventional methods.

# 6 Synthesis of CaFeAsF and $Ca_{0.4}Nd_{0.6}FeAsF$ via solid state metathesis reaction

The 1111 compounds *AE*FeAsF (*AE* = Ca, Sr, Eu) have been reported at the end of 2008[23-26]. The parent compounds show the typical anomaly in resisitvity- and magnetic measurements. For CaFeAsF and SrFeAsF these anomalies could be attributed to similar spin density wave transitions as found for the *RE*FeAsO compunds (*RE* = rare earth metal). The structure changes from tetragonal (spacegoup *P*4/*nmm*) to orthorhombic (*Cmme*) symmetry below ~ 120 K (CaFeAsF) and 175 K (SrFeAsF) respectively[128]. In the case of SrFeAsF, magnetic ordering was detected by means of Mößbauer spectroscopy, and neutron experiments showed that the onset of the magnetic transition is as low as 133 K [24, 129] which is the largest temperature difference between structural and magnetic transition in the iron arsenide family and therefore has intensively been studied[130]. For CaFeAsF the magnetic behavior at low temperatures has not been investigated in detail yet. Like in the *RE*FeAsO compounds, superconductivity can be induced by indirect-electron doping (e. g. $Ca_{1-x}Nd_xFeAsF$ or $Sr_{1-x}La_xFeAs$) [27, 131] or direct electron-doping ($CaFe_{1-x}CoFeASF$ and $SrFe_{1-x}CoAsF$) [25, 26, 128]. To extend the applicability of the solid state metathesis reaction developed for the $LaFeAsO_{1-x}F_x$ series, the concept was transferred to the synthesis of stoichiometric and doped CaFeAsF.

## 6.1 CaFeAsF

### 6.1.1 Synthesis and reactivity

Following the concept of a solid state metathesis reaction, the starting materials for the synthesis of CaFeAsF were CaFCl and NaFeAs, according to the reaction equation:

$$CaFCl + NaFeAs \rightarrow CaFeAsF + NaCl$$

CaFCl is isostructural to LaOCl (PbFCl-type, which was used for the synthesis of LaFeAsO) and contains $FCa_{4/4}$ tetrahedral layers[58], the same structural motif which is found in CaFeAsF. General considerations about the solid state metathesis reaction are described in chapter 5.2. Interestingly, the above formulated reaction would mean a selective halide reaction with sodium. As will be seen this is indeed the case, although one would expect NaF to be the more stable byproduct, compared to NaCl. On the other hand Cl- atoms are too large to replace the F-atoms in the tetrahedral holes of the $FCa_{4/4}$-layers and a hypothetical CaFeAsCl crystallizing in the ZrCuSiAs type structure seems unrealistic.

As compared with the metathesis syntheses in the LaFeAsO system (chapter 5 and 7) slightly milder reaction conditions had to be chosen. The starting materials were pressed to a pellet and heated to 873 K for 20h, followed by heating to 1173 K and reaction for 40 h. First attempts at higher temperatures of the first heating step, led to higher amounts of impurity phases, especially $CaF_2$. This is probably due to the decomposition of CaFCl to $CaF_2$ at temperatures above 973 K, which has already been observed at the synthesis of CaFCl (see chapter 2). Therefore, a first step at moderate temperatures seems to be necessary for the formation of reactive intermediate products, assuming a similar reaction pathway as found for the synthesis of LaFeAsO.

## 6.1.2 Sample quality and physical properties

The optimization of the reaction conditions led to samples of high purity ( > 96 wt%) with $CaF_2$ and traces of Fe (< 0.5 wt%) being the only detected impurities. As an example a Rietveld refinement after the removal of NaCl is depicted in Figure 6.1. The obtained lattice parameters of $a$ = 387.5 (1) pm and $c$ = 858.4 (1) pm are consistent with previously reported[23].

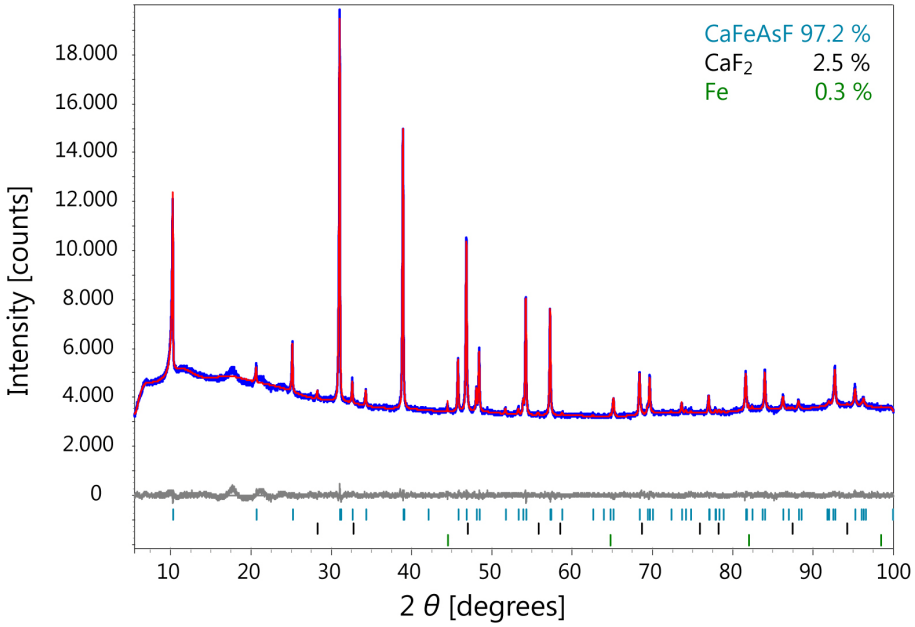


**Figure 6.1:** Rietveld refinement of CaFeAsF.

In first reports of CaFeAsF being a possible parent compound for new iron arsenide superconductors, anomalies in resistivity and magnetic measurements were detected at 118 K, implying structural and magnetic transitions analogous to LaFeAsO[16, 17]. To verify these findings and prove the suitability of the solid state metathesis reaction, the physical properties of CaFeAsF were measured. Figure 6.2 shows the temperature dependent resistivity- and susceptibility (100 Oe, inlay) measurements. The sharp drop of the resistivity at 118 K and the less pronounced drop in the susceptibility measurement confirm the findings by H. H. Wen[23]. The high susceptibility values are probably due to iron as ferromagnetic impurity.

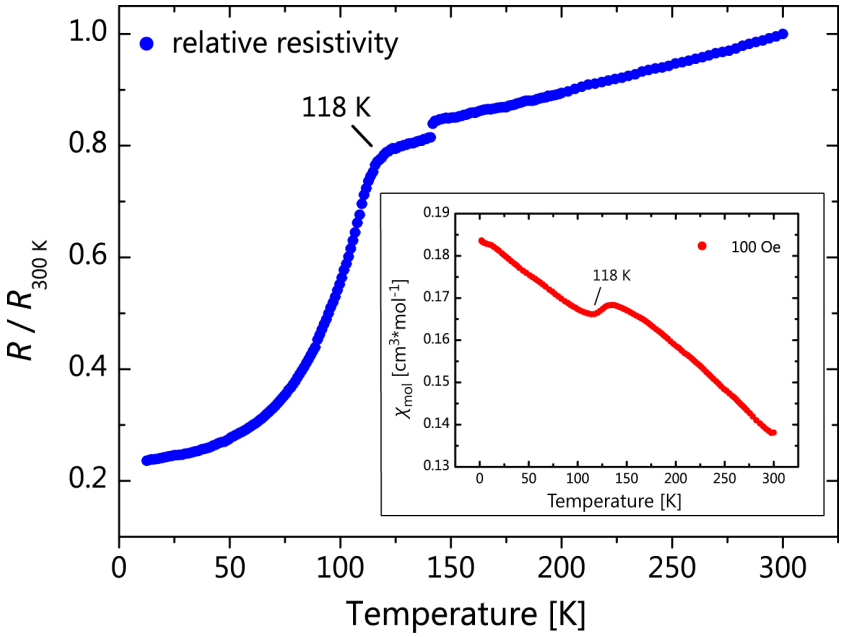


**Figure 6.2:** Temperature dependence of the resistivity and susceptibility of CaFeAsF. The anomaly indicating a structural and / or magnetic transition is clearly visible at 118 K.

## 6.2 $Ca_{0.4}Nd_{0.6}FeAsF$

Simultaneously with the report about the parent compound CaFeAsF, high $T_c$ superconductivity was reported for rare earth doped $Ca_{1-x}RE_xFeASF$ ($x$ = Nd, Pr)[27]. A very high critical temperature of 56 K was reported for $Ca_{0.4}Nd_{0.6}FeAsF$, which one is of the highest reported for the new iron arsenide superconductors. The conventionally prepared (solid state reaction of the binary compounds) samples of Cheng *et al.* contained large amounts of impurities, mainly $CaF_2$, NdAs and $Fe_2As$. Quoting reference [27]: '*…Therefore it would be helpful for forming the superconducting phase by blocking the formation of the $CaF_2$ phase and thus the $Fe_2As$ and REAs (RE =Nd and Pr*'. After the successful synthesis of high purity samples of $LaFeAsO_{1-x}F_x$ and CaFeAsF using a solid state metathesis reaction, the goal was to increase the purity of Nd doped CaFeAsF samples, by a similar synthesis route.

### 6.2.1 Synthesis, sample quality and magnetism

The samples were prepared by heating the starting materials acoording to the reaction equation:

$$NaFeAs + 0.4\ CaFCl + 0.6\ NdF_3 + 0.6\ Na \rightarrow Ca_{0.4}Nd_{0.6}FeAsF + 0.4\ NaCl + 1.2\ NaF$$

Since elemental sodium had to be used to react with additional fluoride, the starting materials could not be pressed to pellets directly, but were pre-reacted at 423 K for 5 h. The as prepared mixtures were compressed to pellets afterwards and heated using different temperature programs:

a. 873 K for 48 h
b. 1173 K for 60 h
c. 1173 K for 20 h followed by 1323 K for 96 h
d. 973 K for 20 h followed by 1223 for 96 h
e. 1173 K for 40 h

The Rietveld refinements of the obtained samples revealed that NdAs, $CaF_2$, $NaNdF_4$ and probably Fe, together with the co-formed NaF and NaCl were the main constituents. The desired ZrCuSiAs type phase $Ca_{1-x}Nd_xFeAsF$ was only detected in samples b. and e. with amounts < 4 wt%. The Ca : Nd ratio was held constant for the refinement according to the nominal composition (0.4 : 0.6). In both samples the 1111 compound was refined with similar cell parameters of $a$ ~ 395 pm and $c$ ~ 855 pm, where the $a$ axis is elongated and the $c$ axis is a little bit shortened compared to the undoped compound (details of the refinements of both samples can be found at the appendix). Cheng *et al.* have found lattice parameters of $a$ = 394.5 pm and $c$ = 859.3 pm for $Ca_{0.4}Nd_{0.6}FeAsF$[27]. The change of the lattice constants therefore indicates a successful replacement of Ca by Nd. However, to what extend Nd was doped into CaFeAsF cannot be said reliably. Interestingly no traces of $Ca_{1-x}Nd_xFeAsF$ have been found when reacting at high

temperatures (> 1173 K). Contrary to this, the reaction temperature of the conventional synthesis performed by Cheng was as high as 1323 K (with yields higher than 4 wt%). This could be due to the formation of $NaNdF_4$, whose formation was favored at the high temperature SSM experiments. To avoid the formation of $NaNdF_4$ another experiment has been performed using LiFeAs plus elemental Li instead of NaFeAs and Na. This, however, did not lead to an improvement of the sample quality, indicating that the formation of very stable $CaF_2$ and NdAs should be the main problem for obtaining samples of high purity.

A zero-field-cooled and field-cooled measurement has been performed on the sample of reaction b. As can be seen from Figure 6.3 a splitting of the zfc- and the fc-signal was observed at a temperature of ~ 55 K, which can be indicative for a superconducting transition. However, the amount of the superconducting phase must be very low, since the magnetic signal remains positive. This is understandable, since the diamagnetism of the superconductor interfers with the strong magnetism of elemental iron for example, which results in a positive signal if the amount of the superconducting phase is as low as detected from the Rietveld refinements. Additionally to the probable superconducting transition, an antiferromagnetic signal is visible at 13 K, which matches with the reported Néel temperature of NdAs[132].

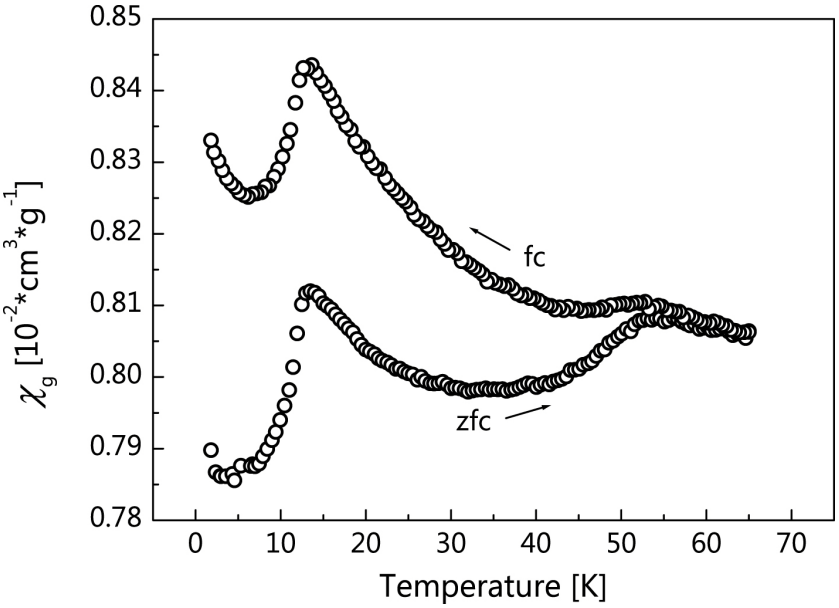


**Figure 6.3:** Zero-field-cooled (zfc) and field-cooled (fc) susceptibility measurements of the mixture obtained from reaction *b* with an applied field of 15 Oe.

## 6.3 Conclusion

The replacement of LaOCl by isostructural CaFCl as starting material for the solid state metathesis reaction with NaFeAs, expanded the applicability of this alternative synthesis route to another family of 1111 iron-arsenide compounds, namely the alkaline earth fluoride iron arsenides. Due to the structural conditions of the targeted compound the reaction is halide selective, as only NaCl is formed as co-product of the metathesis reaction. The physical properties of as-prepared CaFeAsF are consistent with the ones reported for the conventionally prepared compound. However, the formation of the very stable byproduct $CaF_2$ could not be suppressed completely. This together with the formation of other stable compounds like NdAs and $NaNdF_4$ made it difficult to obtain pure samples of Nd doped CaFeAsF. Nevertheless, the small traces of the ZrCuSiAs-type compound showed unit cell parameters as one would expect for Nd doped CaFeAsF. This, together with the performed magnetic measurement can be seen as a confirmation of the superconducting properties of Nd doped CaFeAsF

# 7 Co-substituted $LaFe_{1-x}Mn_xAsO_{1-y}F_y$

*Parts of this chapter are published in:* R. Frankovsky, H. Luetkens, F. Tambornino, A. Marchuk, G. Pascua, A. Amato, H. H. Klauss and Dirk Johrendt,
*Physical Review B* **2013**, *87*, 174515.
Doi: 10.1103/PhysRevB.87.174515
http://link.aps.org/doi/10.1103/PhysRevB.87.174515


## 7.1 Motivation

Charge-doping suppresses structural transitions from tetragonal to orthorhombic symmetry and SDW antiferromagnetism in stoichiometric parent compounds of 1111- and 122-type iron arsenides like LaFeAsO or $BaFe_2As_2$, and superconductivity is induced in the proximity of magnetism[15, 20]. In stark contrast to the cuprates, also substitution of the iron atoms by transition metals with the same or higher number of valence electrons induces superconductivity, for example in $Ba(Fe_{1-x}Co_x)_2As_2$.[45] However, whether transition metal substitution leads to charge doping or acts as scattering centers is still under debate[133-135].
Even less understood is the fact that hole-doping by transition metal substitution (Cr, Mn) has on no account induced superconductivity so far[46, 48, 136, 137].
Substitution of Fe by Cr or Mn in $Ba(Fe_{1-x}TM_x)_2As_2$ leads to a suppression of the structural transition for $x \geq 0.335$ and $x > 0.10$ respectively[46, 136-138]. Even though the transition is absent for highly doped samples, a magnetic phase develops albeit with a magnetic structure different from the low doped samples[137, 139]. The antiferromagnetic ordering changes from stripe-like (SDW) to Néel-type (G-type) in Cr substituted compounds, which is consistent with the absence of the orthorhombic phase. A co-existence of both types of AFM ordering is reported for $x = 0.305$ and $x = 0.335$, although the structural transition is already suppressed for

the latter concentration [137]. This is unusual, since the stripe-like SDW is believed to be coupled to the orthorhombic transition by magnetoelastic effects[140-142]. For $Ba(Fe_{1-x}Mn_x)_2As_2$ a more complicated behavior is observed. In first reports, magnetic ordering with a propagation vector (½ ½ 1) (stripe-like or SDW AFM) was observed in the absence of the orthorhombic distortion ($x$ > 0.10) but no traces of Néel type fluctuations or ordering have been found[46]. However, recent neutron diffraction studies found co-existence of long-ranged stripe like antiferromagentic ordering and purely dynamic short-range Néel type spin fluctuations introduced by Mn in $Ba(Fe_{0.925}Mn_{0.075})_2As_2$[139]. Whether these short-range fluctuations are also present in the samples with higher Mn concentrations has not been studied yet. NMR measurements of $Ba(Fe_{1-x}Mn_x)_2As_2$ revealed localized Mn moments, which couple to the conduction electrons and induce a staggered spin polarization within the Fe-layer[135]. It was proposed that spin fluctuations (Néel-type) which arise from these local Mn moments could be disruptive for superconductivity[135, 139]. Actually, very recent theoretical calculations confirmed the suppression of superconductivity by Néel type fluctuations in the iron pnictides[143]. Meanwhile there is growing evidence for local Mn moments leading to a different type of (short range) magnetic fluctuations / ordering, which competes with the long range ordering developed by the Fe lattice.

In contrast to this, very little is known about manganese substitution in 1111 compounds. Substitution of Fe by Mn in CaFeAsF and LaFeAsO changes the resistivity behavior from metallic to semiconducting[48, 144]. Because this is already observed for very small Mn concentrations one may argue that Mn mainly acts as a scattering center in these compounds[144]. In $LaFe_{1-x}Mn_xAsO$ the structural distortion seems to be suppressed at $x$ > 0.06 according to conductivity and thermoelectric power measurements[48]. However, information about the magnetic behavior of the 1111-compounds upon Mn substitution is still lacking.

It is widely believed that in FeAs superconductors certain structural preconditions like interatomic distances, the pnictogen layer height or the distance between the iron-arsenide layers have to be fulfilled to induce superconductivity or to reach

high critical temperatures (for an overview see Ref. [43]). One of the most noticeable correlations of $T_c$ to a structural parameter is found in the As–Fe–As angles of the FeAs tetrahedra. Lee *et al.* have collected structural data from many iron based superconductors and found that the highest $T_c$s appear in systems were the angles are close to the value of 109.47°, suggesting that the potential for high critical temperatures is biggest for regular tetrahedral[51]. It has been suggested that the angle is not only determined by the different atom sizes but that the electron count plays an important role as well[36]. Although the experimental data indicate that an ideal tetrahedral angle seems to be crucial for high $T_c$s, the most recent investigations about the interplay between doping and structural changes in doped $BaFe_2As_2$ have shown that charge modifications play the mayor role for the suppression of magnetism and the emergence of superconductivity. Zinth *et al.* have demonstrated that charge compensation in $Ba_{1-x}K_x(Fe_{0.93}Co_{0.07})_2As_2$ ($x \approx 0.14$) recovers the magnetic and structural transitions of the parent compound and superconductivity re-emerges for lower (electron-doped) as well as for higher (hole-doped) potassium concentrations.[53] This shows how the physical properties can be controlled by modifying the charge balance in $BaFe_2As_2$.

To expand the knowledge about the influence of direct hole-doping on the structural, electronic and magnetic properties of 1111-type iron arsenides, the series $LaFe_{1-x}Mn_xAsO$ ($x$ = 0.0 - 0.2) was investigated and a comparison is drawn with directly hole-doped 122 compounds. Furthermore the influence of charge compensation by additional electrons due to additional F doping in $LaFe_{0.1}Mn_{0.1}AsO_{0.9}F_{0.1}$ as well as the formally electron doped series $LaFe_{0.9}Mn_{0.1}AsO_{1-y}F_y$ ($y$ = 0.2-0.5) is presented.

## 7.2 Synthesis

The synthesis of the $LaFe_{1-x}Mn_xAsO_{1-y}F_y$ samples was performed by heating stoichiometric amounts of LaOCl, NaFeAs, NaMnAs, $LaF_3$ (powder, 99.99 %) and Na (ingots, 99.8 %) according to the solid-state metathesis reaction:

$$(1-x)\ NaFeAs + x\ NaMnAs + (1-y)\ LaOCl + y\ LaF_3 + y\ Na \rightarrow LaFe_{1-x}Mn_xAsO_{1-y}F_y + (1-y)\ NaCl + 2y\ NaF$$

($x$ = 0.05 – 0.20; $y$ = 0.0 – 0.5 with $x$ = 0.1)

General considerations about the solid-state metathesis reaction are discussed in chapter 5. Here, it should be noted that NaMnAs is isostructural to NaFeAs and therefore it also contains the $FeAs_{4/4}$ tetrahedral layers as a structural motif. The precursors were well homogenized, filled in alumina crucibles, welded in Niobium tubes enclosed by silica tubes. All crucibles and tubes contained a purified argon atmosphere. The reaction mixtures were heated to 1023 K for 48 h and 1223 K for 96 h, followed by cooling to room temperature with 200 K/h. The co-formed salts NaCl and NaF were removed by washing the obtained mixture with water (3 times) and ethanol, followed by drying the product under high vacuum. The synthesis of the starting materials is described in chapter 2.

## 7.3 Sample quality and structural changes upon doping

The metathesis reaction yielded single phase samples of $LaFe_{1-x}Mn_xAsO$. With increasing Mn concentration the cell parameters and the volume increase almost linearly, indicating that Mn is successfully inserted (see Figure 7.1). This, together with the sample purity, indicates that the effective Mn contents are very close to the nominal ones

Parallel to the unit cell expansion, the Fe–As and metal–metal distances increase. The twofold As–Fe–As angle $\varepsilon_2$ of the FeAs tetrahedra becomes more regular, decreasing from 113.1(2)° ($x$ = 0) to 111.8(2)° ($x$ = 0.20). The structural changes upon Mn-doping are therefore consistent with the ones reported by Bérardan *et al.* ($x$ = 0-0.1)[48], but the reported cell parameters of the corresponding sample compositions are much larger than those we find.

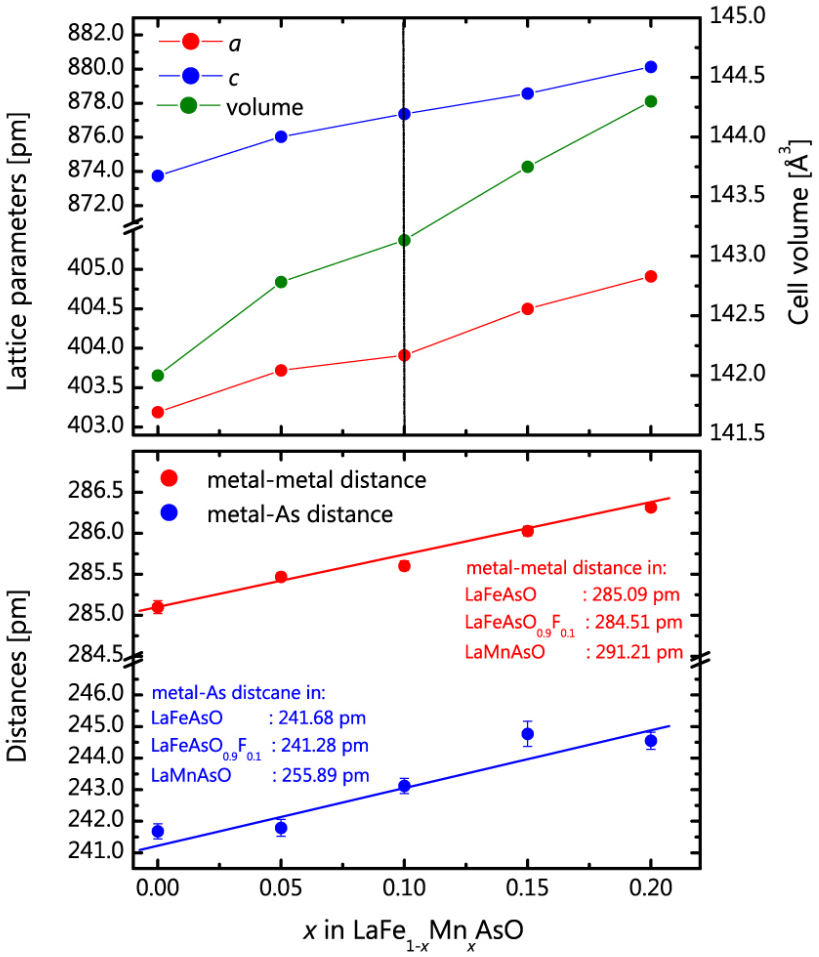


**Figure 7.1:** Changes of the unit cell parameters (top) and interatomic distances (bottom) with increasing Mn fraction in $LaFe_{1-x}Mn_xAsO$. The dotted black line marks the Mn concentration held constant for the series $LaFe_{0.9}Mn_{0.1}AsO_{1-y}F_y$. Some interatomic distances of similar 1111 compounds are listed for comparison.

The effective doping levels have been confirmed by at least 5 EDX measurements of each sample and averaged compositions showing deviations of less than 1 % of the nominal compositions were obtained (Figure 7.2).

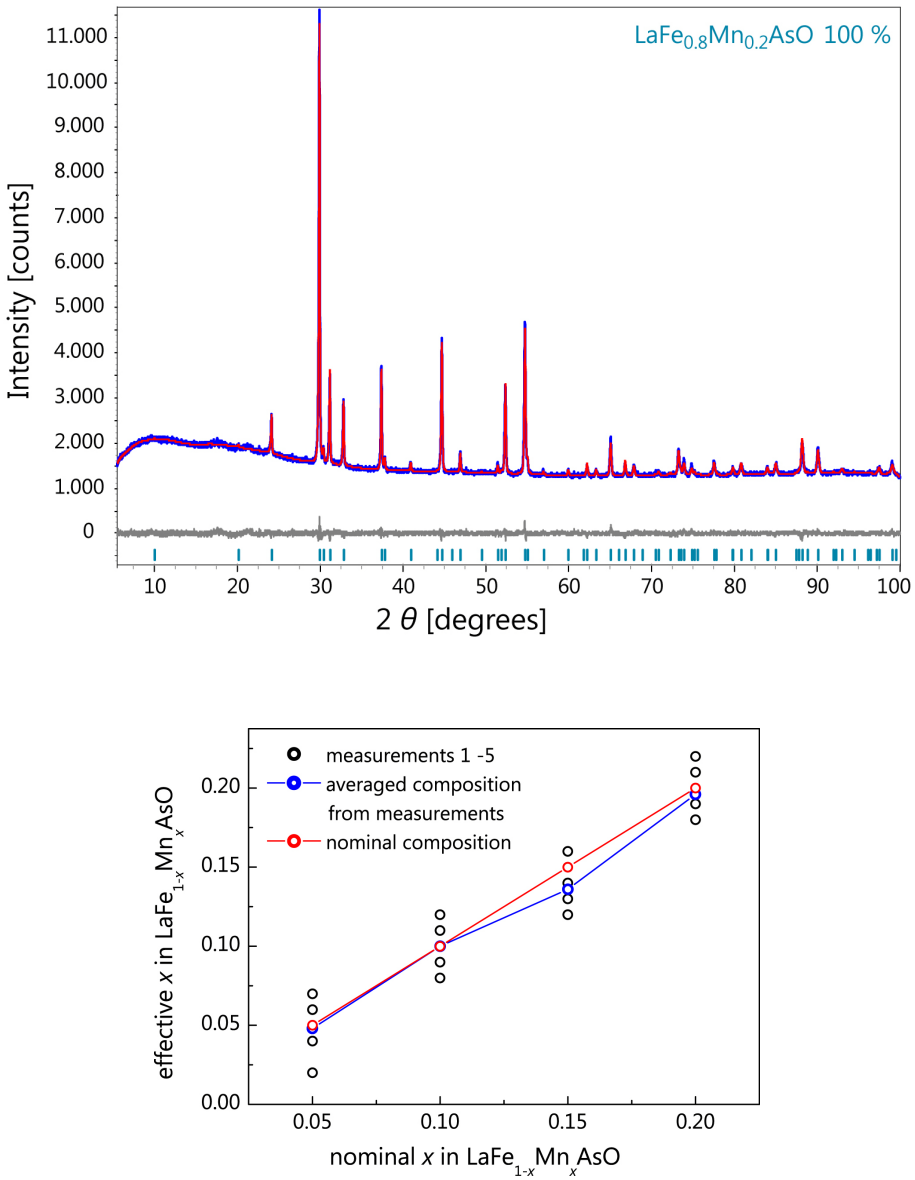


**Figure 7.2:** Rietveld refinement of $LaFe_{0.8}Mn_{0.2}AsO$ (top) and results from EDX measurements on $LaFe_{1-x}Mn_xAsO$ (bottom; black circles: individual measurements; blue circles: averaged composition from individual measurements; red circles: nominal composition)

Samples of the series $LaFe_{0.9}Mn_{0.1}AsO_{1-y}F_y$ ($y$ = 0.1 – 0.5) contained small amounts of LaAs (< 3 wt%, for $y$ = 0.1 and 0.2) and with increasing $y$ additional $Na_{1.5}La_{1.5}F_6$ ($y$ = 0.3, 0.4, 0.5) and $LaF_2$ ($y$ = 0.4, 0.5) were identified as impurities, with the highest amount (sum of 20 wt%) for the highest nominal fluorine content. Since the effective F content cannot be derived from Rietveld refinements or EDX measurements, the evolution of the lattice parameters was used as indicator of the effective F content in the samples. As one can see from Figure 7.3, additional F in

$LaFe_{0.9}Mn_{0.1}AsO$ leads to a decrease of the lattice parameter *a*, while the *c* axis is more or less unaffected after a small decrease for $y = 0.1$ Since the sample quality is very good for low F concentrations, the effective F content should be very similar to the nominal one in the low doping regime. The decreasing cell volume indicates that the effective F content further increases with nominal *y*, despite the higher amount of impurities. Therefore the nominal fluorine contents are stated keeping in mind that higher *y* also means higher effective F content (even though they might not be linearly related).

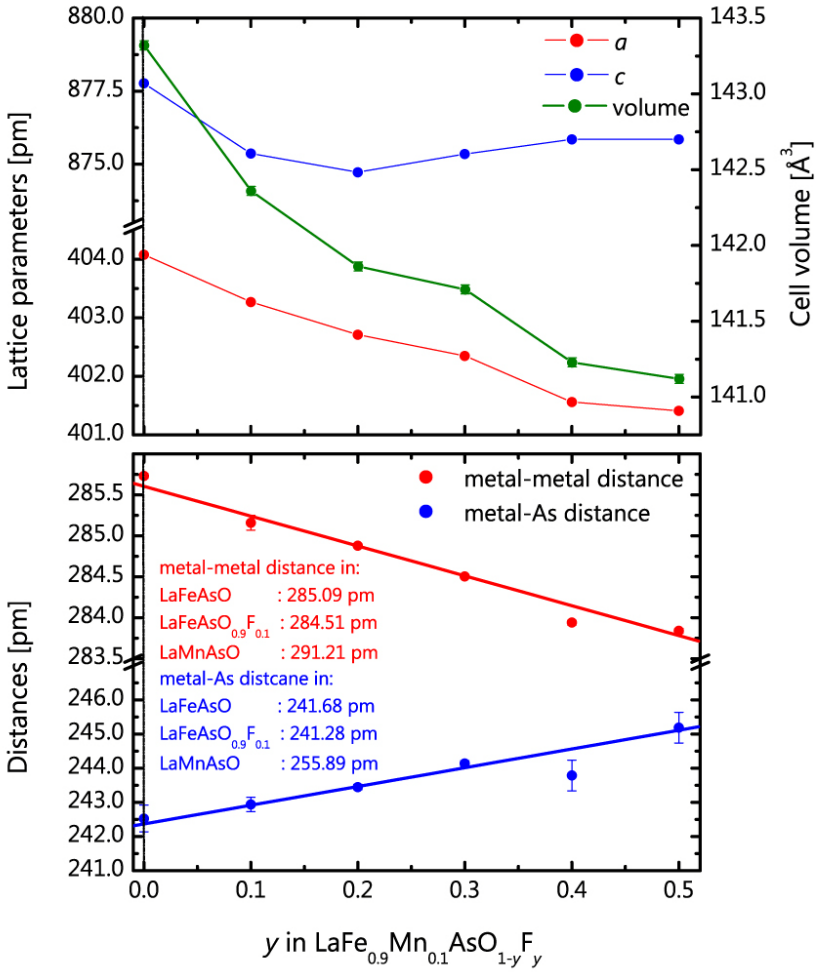


**Figure 7.3:** Changes of the unit cell parameters (top) and interatomic distances (bottom) with increasing F content in $LaFe_{0.9}Mn_{0.1}AsO_{1-y}F_y$.

Together with the shrinkage of the *a*-axis also the Fe-Fe bond length is decreased, which reaches a value similar to optimally electron doped $LaFeAsO_{0.9}F_{0.1}$, for

$y$ = 0.3. The two-fold As–Fe–As angle $\varepsilon_2$ further decreases with increasing $y$ and almost reaches the ideal value of 109.47° for $y$ = 0.5(≈ 110°). Because of the shrinkage of the $a$-axis (together with the $\varepsilon_2$ angle) and the nearly unaffected length of the $c$ axis, a geometrical consequence is a further increase of the metal-arsenic distance. From a structural point of view, with additional F doping in $LaFe_{0.9}Mn_{0.1}AsO$ the precondition for superconductivity appears to be fulfilled. Metal-metal distances similar to optimally electron doped LaFeAsO and an As–Fe–As angle close to the ideal value are found. Counterproductive to this is the increasing metal-arsenic distance caused by the initially increase of the $c$ axis by Mn doping. An increasing bond length can lead to more localized electrons due to a smaller orbital overlap.

## 7.4 Physical properties

A metal to semiconductor transition for Mn concentrations higher than 3 % and an increasing semiconducting behavior with increasing Mn content in $LaFe_{1-x}Mn_xAsO$ was reported[48]. The semiconducting behavior is associated to the suppression of the structural transition, which was concluded from thermopower measurements[48].

The resistivity measurements of the samples prepared by the solid-state metathesis reaction are consistent also for further Mn doping as can be seen from Figure 7.4. With increasing $x$, the semiconducting behavior gets more pronounced and the relative resistance ratio $R_{12K}$ / $R_{300K}$ is the highest for $x$ = 0.2. The measured resistivity $\rho_s$ at 300 K is increasing as well, and it is one order of magnitude higher for the highest Mn concentration compared to undoped LaFeAsO ($4.7 \cdot 10^{-4}$ Ωm for $x$ = 0.2 and $2.8 \cdot 10^{-5}$ Ωm for $x$ = 0.0). Furthermore low temperature XRD measurements showed that the structural transition is absent for the whole series $LaFe_{1-x}Mn_xAsO$ ($x$ = 0.05-0.20)

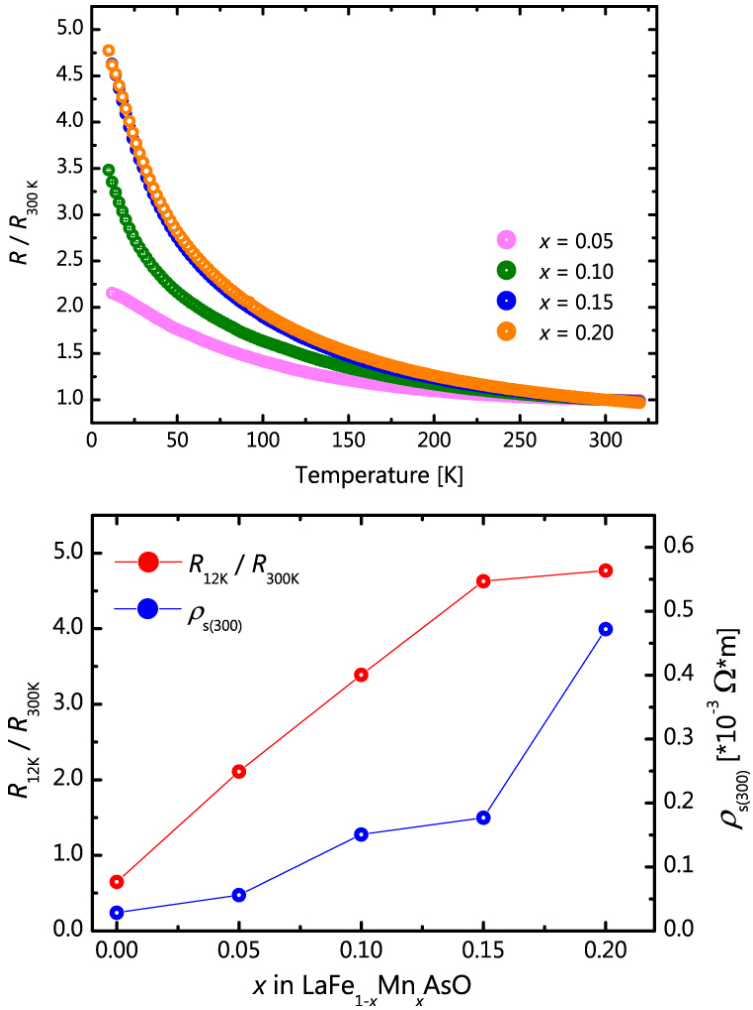


**Figure 7.4:** Temperature-dependence of the normalized resistivity $R$ / $R_{300K}$ for $LaFe_{1-x}Mn_xAsO$ (top); evolution of $R_{12K}$ / $R_{300K}$ and resistivity $\rho$ at 300 K with increasing Mn content (bottom).

Additional electrons introduced by F doping lead to a higher charge carrier concentration within the FeAs-layer and the metallic behavior is regained with increasing F doping. Figure 7.5 shows that F doping in $LaFe_{0.9}Mn_{0.1}AsO_{1-y}F_y$ leads to a decrease of the $R_{12K}$ / $R_{300K}$ values and the resistivity $\rho_s$ at 300 K. The discordant values for $\rho_{s(300)}$ of the $y$ = 0.3 and 0.5 sample are probably due to increased contact resistances. No superconductivity was found for the formally electron-doped samples ($y$ > 0.2) nor any anomaly of the electrical resistivity was observed for charge compensated $LaFe_{0.9}Mn_{0.1}AsO_{0.9}F_{0.1}$, what could have been indicative for structural or magnetic transitions. Low temperature XRD measurements of $LaFe_{0.9}Mn_{0.1}AsO_{1-y}F_y$ ($y$ = 0.10 and 0.20) showed no transition from tetragonal to orthorhombic symmetry at low temperatures.

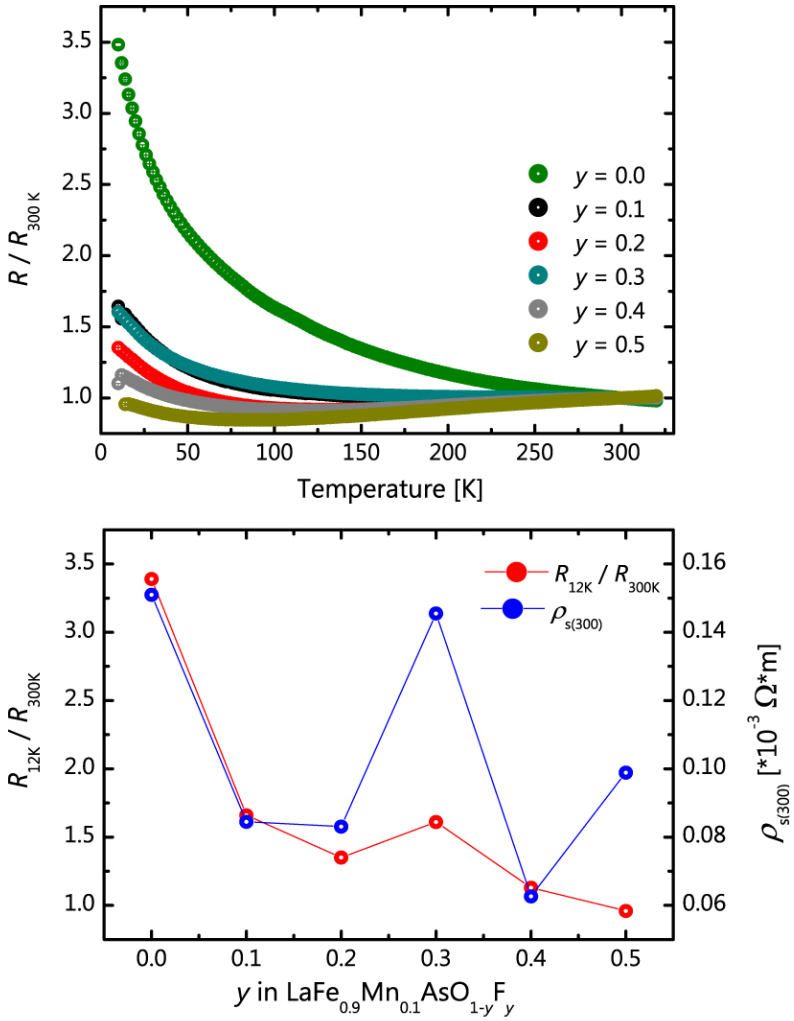


**Figure 7.5:** Temperature-dependence of the normalized resistivity $R$ / $R_{300K}$ for $LaFe_{0.9}Mn_{0.1}AsO_{1-y}F_y$ (top); evolution of $R_{12K}$ / $R_{300K}$ and resistivity $\rho$ at 300 K with increasing F content (bottom).

Magnetic measurements on the SQUID magnetometer showed temperature-independent susceptibility and no anomaly that would indicate a magnetic transition. In some samples ferromagnetic impurities were found. Under the assumption that these impurities are iron, the amounts were estimated to be smaller than 0.5 *wt* %. For a more detailed study of the magnetic properties muon spin relaxation (μSR) experiments were performed on the $x$ = 0.05-0.20 and the $y$ = 0.10 and 0.20 samples at the πM3 beam line at the Paul-Scherrer-Institut (Switzerland). μSR as a local magnetic probe can provide valuable information on the magnetic volume fraction and the magnetic homogeneity. Figure 7.6 shows the zero field (ZF) μSR spectra for the Mn doped samples ($y$ = 0). The data of

LaFeAsO ($x$ = 0) are shown for comparison[145]. At high temperatures the muon spin polarization is only weakly relaxing as a function of time due to the interaction of the muon spin ensemble with the small magnetic fields originating from nuclear magnetic moments or diluted ferromagnetic impurities only. At low temperatures anyhow the muons might experience a much stronger internal magnetic field due to ordering of the electronic moments. This is the case for all Mn doped samples as evident from the strongly time dependent muon spin polarization observed in the ZF spectra. In a long range ordered magnet a coherent muon precession of the whole ensemble is observed giving rise to long-lived oscillations in the ZF μSR time spectra as it is the case for the $x$ = 0.0 sample. The value of the precession frequency is proportional to local magnetic field and therefore to the ordered electronic magnetic moment. A damping of the μSR oscillation indicates a distribution of internal magnetic fields sensed by the muon ensemble and is therefore a measure of the disorder in the magnetic system. It is evident that the μSR precession is strongly damped for all Mn- doped samples. This proves that the doping of Mn ions into the magnetic Fe lattice introduces considerable disorder making the magnetic ordering short range in nature. The magnetic correlation length can be estimated with a rule of thumb: If the precession is just visible as in the $x$ = 0.05 sample the magnetic correlation length is about 10 lattice constants only[146]. Interestingly the observed frequency is still 16.5 MHz for the $x$ = 0.05 sample compared to 23 MHz at $x$ = 0. If the same stripe AFM magnetic structure is assumed this means that the average ordered magnetic moment is only reduced by 29% for this doping level. It should be noted that it seems unlikely that the stripe AFM order is realized since no structural distortion could be observed for $x$ > 0.05. From the local probe (μSR) data alone it is not possible to deduce the magnetic structure. Therefore it is also not possible to decide if the apparent magnetic disorder stems from localized magnetic Mn ions within a disordered stripe AFM phase or if it is due to a disordered mixture of different anti-ferromagnetic phases as e.g. observed in Cr doped $Ba(Fe_{1-x}Cr_x)_2As_2$ [137] or due to a new disordered magnetic structure e.g. of Néel-type as observed in LaMnAsO or

$BaMn_2As_2$.[147, 148] To clarify this point magnetic neutron scattering data would be indispensable.

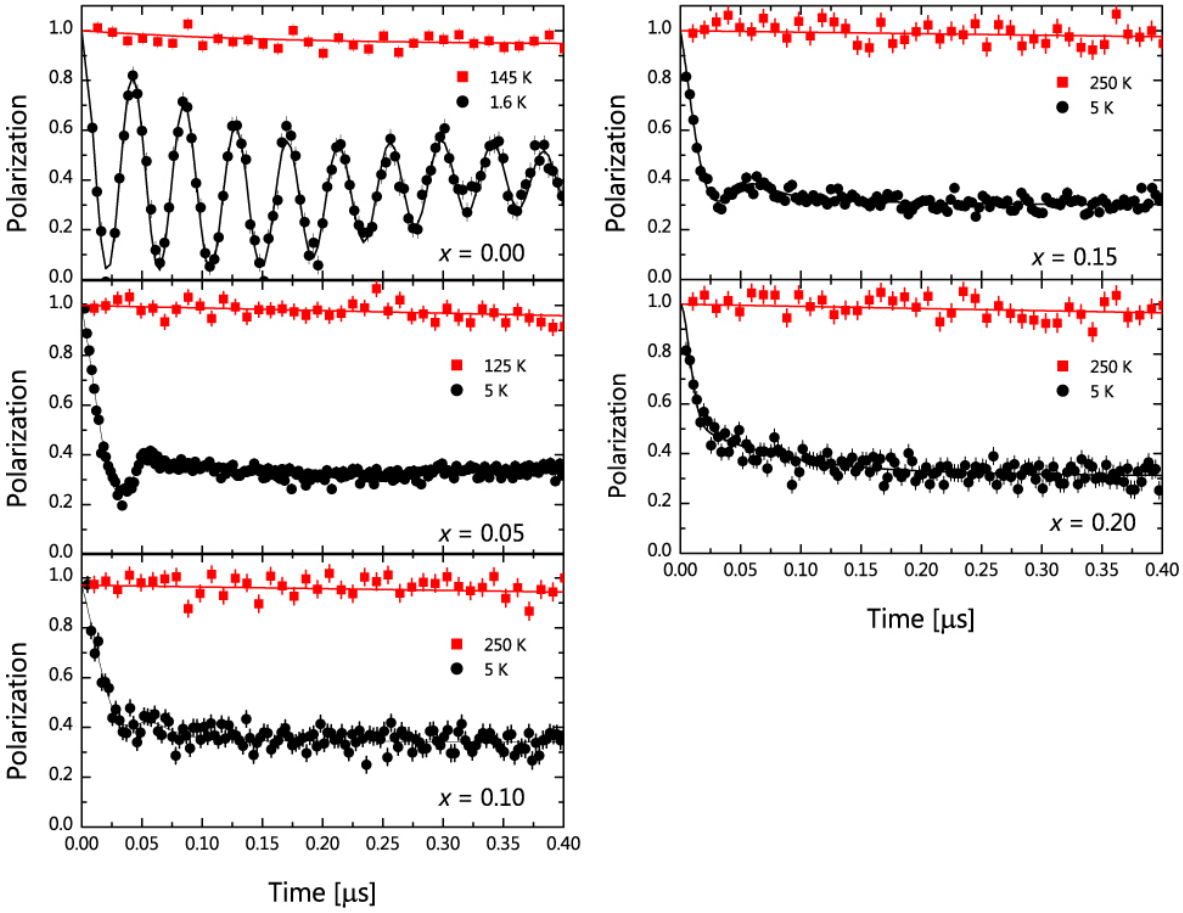


**Figure 7.6:** Zero field spectra of the $LaFe_{1-x}Mn_xAsO$ series, the data for $x$ = 0.0 was taken from [145].

With a local probe like ZF μSR on the other hand it is possible to determine the magnetic volume fraction. In a 100% static magnetically ordered powder, 2/3 of the internal field components are perpendicular to the initial muon spin direction and cause a precession (or fast relaxation) while the remaining 1/3 fraction does not precess. It is clear from Figure 7.6 that in all Mn doped samples the full volume is statically magnetic at 5 K. In a dynamic magnetic state also the remaining 1/3 component would show a relaxation [146] which is not the case here. In magnetically ordered $Ba(Fe_{0.925}Mn_{0.075})_2As_2$ inelastic neutron scattering have detected magnetic spin fluctuations at two different wave vectors corresponding to the stripe and Néel type of magnetic order[139]. Here, no indications for spin fluctuations in

$LaFe_{1-x}Mn_xAsO$ are found. This does not necessarily mean the absence of these fluctuations, but that the fluctuations, if present, are too fast to be observed within the time window of the μSR technique.

The temperature dependence of the magnetic volume fraction can be better determined in a series of weak transverse field (TF) μSR measurements. In this case a weak external magnetic field of 50 Oe is applied perpendicular to the initial muon spin direction. In a paramagnetic state all the muon spins precess in the external field. If the sample, on the other hand, is magnetic the muon spins precess in the much larger internal fields. Therefore the amplitude of the precession signal in the external magnetic field is a measure for the paramagnetic volume fraction. In Figure 7.7 the magnetic volume fraction is shown as a function of temperature for various Mn doping levels. The transition is rather broad for the Mn-doped samples, while it is sharp for the undoped compound. This indicates a certain amount of disorder and/or chemical inhomogeneity. In such a situation it is difficult to determine the true Néel temperature $T_N$, therefore the values for 10%, 50% and 90% magnetic ordering are highlighted.

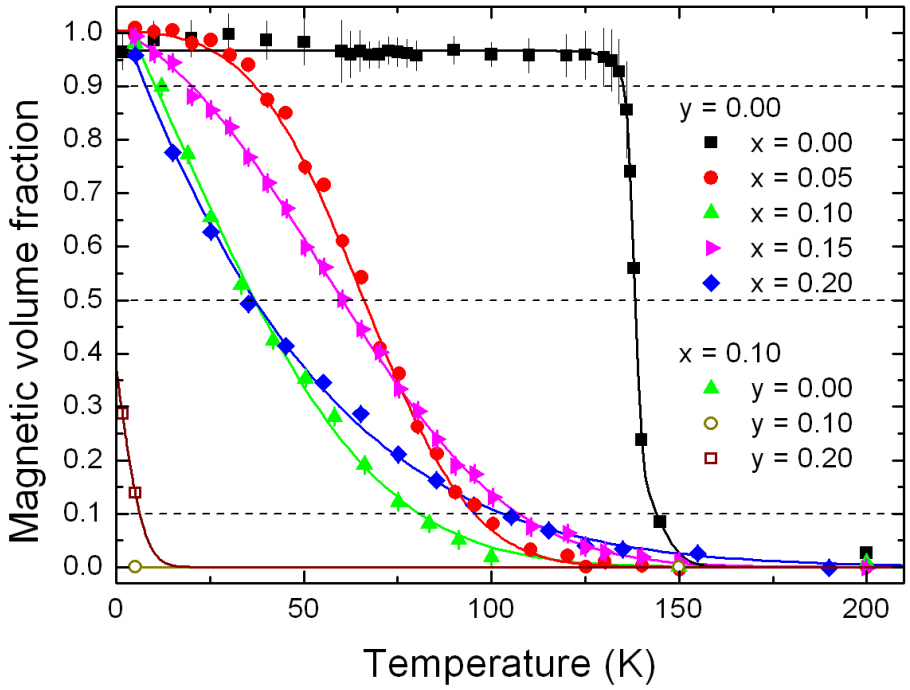


**Figure 7.7:** Development of the magnetic volume fraction as a function of temperature for $LaFe_{1-x}Mn_xAsO_{1-y}F_y$, data for $x$ = 0.0 are taken from Ref. [145].

In Figure 7.8 the obtained magnetic phase diagram is shown. It resembles that for Mn doped $BaFe_2As_2$ with a minimum of $T_N$ around $x$ = 0.10. For Mn concentrations of x ≥ 0.10 in $Ba(Fe_{1-x}Mn_x)_2As_2$ only long-range magnetic order has been detected so far.[46, 138] On the contrary our data indicate short range / disordered magnetism for the 1111 system which can be understood if Mn acts predominately as a magnetic scattering centre, which presumably distorts the long range magnetic order of the iron atoms, or induces a different type of short range antiferromagnetic order itself. Additionally, it is natural to assume that the SDW magnetism of the Fe sublattice which is observed for the parent compound is destroyed or at least fairly disturbed by Mn doping with x ≥ 0.05 since the magnetoelastically coupled orthorhombic distortion is absent for these samples.

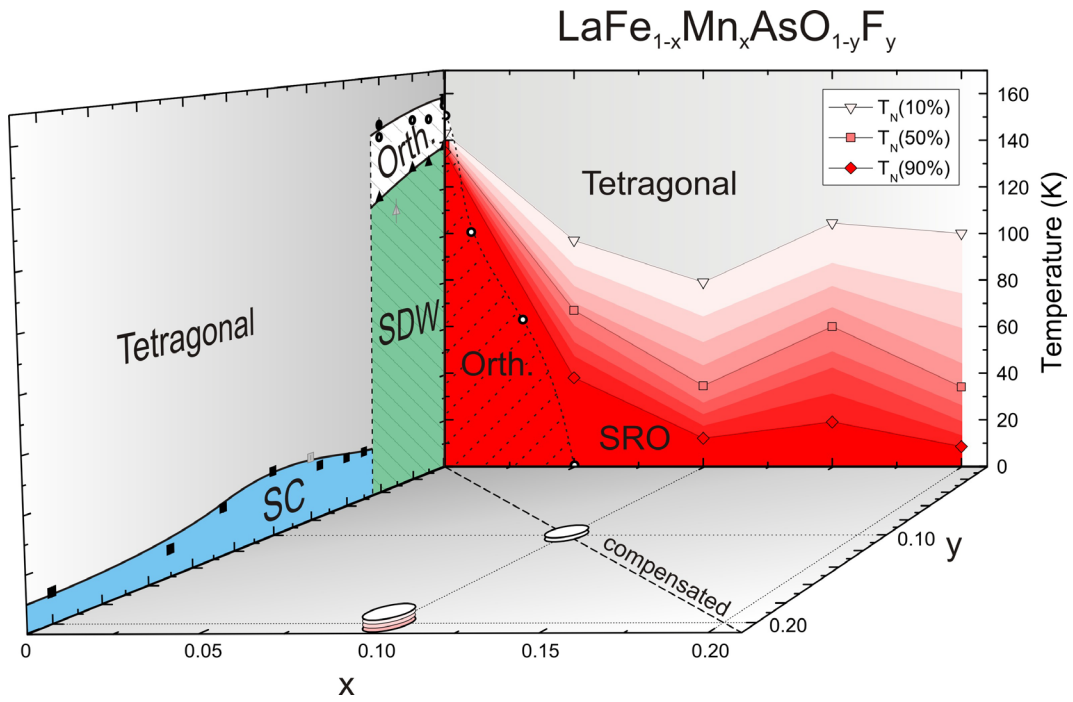


**Figure 7.8:** Structural and magnetic phase diagram of $LaFe_{1-x}Mn_xAsO_{1-y}F_y$. The structural data for $x$ < 0.05 are taken from Ref. [48]. The data for $x$ = 0.0 are taken from Ref. [145]. The magnetic volume fraction has a color code in steps of 10% from white (0% magnetic) to red (90% magnetic). The compensated sample with $x$ = 0.1 and $y$ = 0.1 is non-magnetic down to the lowest measured temperature while weak magnetism develops in 30% of the sample in the $x$ = 0.1, $y$ = 0.2 sample below 5 K.

The zf spectra of the charge compensated ($y$ = 0.10) and formally electron-doped sample ($y$ = 0.20) are shown in Figure 7.9 (together with $LaFe_{0.9}Mn_{0.1}AsO$). Surprisingly, F doping leads to a complete suppression of the magnetic transition and the $y$ = 0.1 sample is non-magnetic over the whole temperature range. The observation of an essentially non-magnetic state for a charge compensated sample is astonishing since it is completely different from $Ba_{1-x}K_x(Fe_{0.93}Co_{0.07})_2As_2$ ($x \approx 0.14$), where the magnetism of the parent compound is regained for the charge compensated composition.[53] Actually we would like to point out that in the case of the 1111 family investigated here the charge compensated sample with $x = y = 0.1$ is the most non-magnetic sample investigated in this study.

The $y$ = 0.2 sample is similar to the $y$ = 0.1 sample, but the magnetism is slightly stronger which can be appreciated by comparing the 5 K data in Figure 7.9. ZF, TF and LF μSR measurements show that the observed weak magnetism remains partially dynamic down to the lowest measured temperatures and that it does only occupy ≈ 30% of the sample volume (see Figure 7.7). In none of the investigated samples superconductivity could be observed. This means that although the magnetism can be suppressed or strongly weakened with further F doping it is not possible to induce superconductivity in F doped $LaFe_{0.9}Mn_{0.1}AsO$.

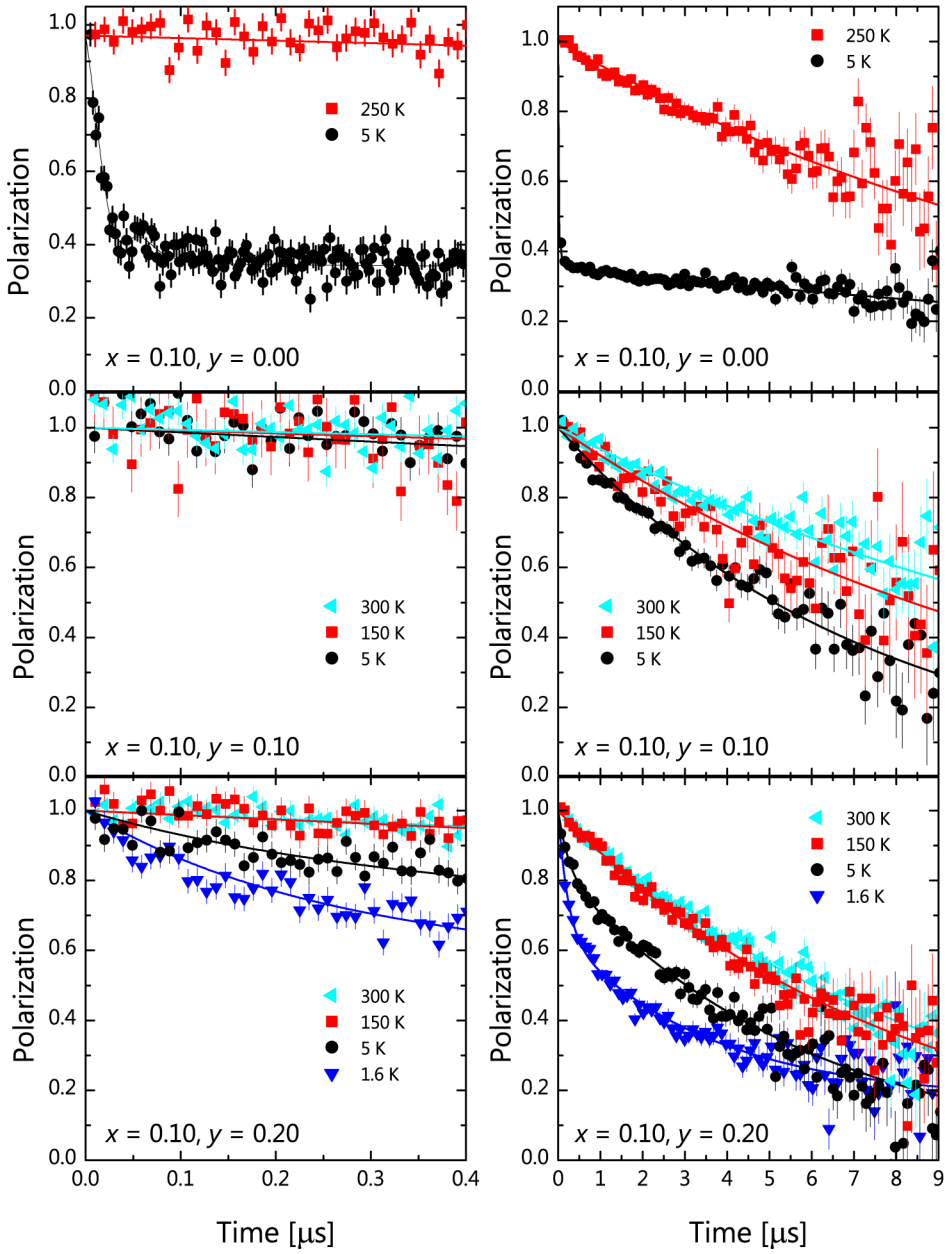


**Figure 7.9:** Zero field spectra of $LaFe_{0.9}Mn_{0.1}AsO$ and $LaFe_{0.9}Mn_{0.1}AsO_{1-y}F_y$ ($y$ = 0.1 and 0.2). On the left side a short time window is shown as for the Mn doped series and on the right a long time window is displayed, since the magnetism is much weaker for the F doped compounds.

From a NMR study Texier *et al.* [135] found that introducing Mn into $Ba(Fe_{1-x}Mn_x)_2As_2$ does actually not introduce charge doping, and that the Mn ion carries a local moment due to the localization of the additional hole. These localized moments in turn can couple to the Fe electronic band and induce an alternating spin polarization into it. For the case of $Ba(Fe_{1-x}Mn_x)_2As_2$ it was argued that these local Mn moments are unable to suppress the antiferromagnetic

ordering at low doping, but that they suppress superconductivity due to breaking of Cooper pairs. Texier *et al.* [135] speculate that this pair breaking should prevent superconductivity even if the long range magnetic order could be destroyed by other means.

Similar conclusions can be drawn from the structural, magnetic and transport measurements on $LaFe_{1-x}Mn_xAsO_{1-y}F_y$. The doping with relatively small amounts of $x \geq 0.05$ Mn into $LaFe_{1-x}Mn_xAsO$ leads to a complete suppression of the tetragonal to orthorhombic transition usually concomitant with the stripe-like SDW AFM order. Upon further Mn doping short range magnetism is found to persist up to the highest doping level studied here. It is possible that a similar but more disordered kind of Néel magnetic order as observed for Cr and Mn doped $BaFe_2As_2$ compounds is established, even though this hypothesis cannot directly be proven with a local probe technique like μSR. As in the case of $Ba(Fe_{1-x}Mn_x)_2As_2$ no superconductivity is induced by Mn doping into LaFeAsO. On the contrary, the room temperature resistivity increases with Mn doping and the temperature dependence of the resistivity changes from metallic to increasingly semiconducting and the increasing bond lengths indicate a more localized electronic behavior. The electron doping by introducing F into of $LaFe_{0.9}Mn_{0.1}AsO_{1-y}F_y$ in contrast increases the conductivity of the system as evidenced by resistivity measurements. In addition, the static magnetism is quickly suppressed by the electron doping and the structural prerequisites for high-$T_c$ superconductivity like an almost regular Fe-As tetrahedron is successively approached. Nevertheless neither in the nominally charge compensated compound ($x$ = 0.1, $y$ = 0.1) nor in the nominally electron doped compound ($x$ = 0.1, $y$ = 0.2) superconductivity is induced. Theoretically it has been shown, that the combination of short-range Néel fluctuations and pair-breaking impurity scattering effectively can suppress superconductivity[143]. Therefore it is reasonable to assume that a similar effect is at work in $LaFe_{0.9}Mn_{0.1}AsO_{1-y}F_y$ as well with localized paramagnetic Mn magnetic moments and possibly residual Néel fluctuations acting as pair breakers in the otherwise non-magnetic samples.

## 7.5 Conclusion

High quality Samples of $LaFe_{1-x}Mn_xAsO$ were obtained using a solid state metathesis reaction. Also the double substituted $LaFe_{0.9}Mn_{0.1}AsO_{1-y}F_x$ series has been obtained in very good quality in a one step reaction, despite the use of five starting materials. Structural investigations revealed that upon additional F doping, parameters like the metal-metal distance or the As–Fe–As angle reach values which have been thought to be essential for the emergence of high superconducting $T_c$s. On the other hand, the increase of the metal-arsenic distances indicates a situation with stronger localization of the electrons. The magnetic behavior of the Mn doped 1111 compounds is different from the corresponding 122 compounds. From μSR measurements short ranged magnetic order was found, with the transition temperatures passing a minimum for $x$ = 0.10. While the structural transition is present for Mn concentrations of up to ≈ 11 % in $Ba(Fe_{1-x})_2Mn_xAs_2$, the $LaFe_{1-x}Mn_xAsO$ series shows no structural transition down to 10 K. The previously reported semiconducting character of $LaFe_{1-x}Mn_xAsO$ ($x$ = 0-0.1) [48] was confirmed and gets more pronounced with higher Mn concentrations. Together with the semiconducting character, the measured $\rho_{s(300K)}$ values are further increased with increasing Mn concentration.

Additional electron doping with F leads in turn to a more metallic behavior. On the other hand, the magnetic transition is completely suppressed for charge-compensated $LaFe_{0.9}Mn_{0.1}AsO_{0.9}F_{0.1}$, which means that charge compensation does not lead to the regain of the parents compound properties as in $Ba_{1-x}K_xFe_{1.86}Co_{0.14}As_2$ ($x \approx 0.14$)[53]. The nominal optimal electron-doped $LaFe_{0.9}Mn_{0.1}AsO_{0.8}F_{0.2}$ shows very weak magnetism at temperatures below 5 K. Thus although the magnetic transition is suppressed and the electron count should lead to a superconducting state, the latter is not observed down to low temperatures. As stated above, it has been proposed that in such a case the localized Mn moments and possible residual Néel fluctuations may act as pair breakers. In agreement with this theoretical prediction, the results show that Mn impurities

within the FeAs layer are detrimental to superconductivity in electron doped $LaFeAsO_{1-y}F_y$. In summary, the series $LaFe_{1-x}Mn_xAsO_{1-y}F_y$ shows a complex structural, electronic and magnetic phase diagram in which electron and hole doping have very different electronic and magnetic effects. This is in stark contrast to the $Ba_{1-x}K_x(Fe_{1-y}Co_y)_2As_2$ system where the electron count essentially governs the physical properties[53].

# 8 Summary

## $La_3Pd_{4-x}Fe_xGe_4$

$La_3Pd_4Ge_4$ crystallizes in the $U_3Ni_4Si_4$ type structure (spacegroup *Immm*, $Z = 2$)[101, 103]. The structure can be described by alternating layers of $AlB_2$ type units and $BaAl_4$ type units, which leads to two crystallographically independent Pd atom sites. Within the $AlB_2$ type layers, Pd is trigonally planar coordinated by three Ge atoms and within the $BaAl_4$ type units, the Pd atoms are located in the centre of edge sharing $PdGe_{4/4}$ tetrahedra. The latter structural motif of metal- germanide / arsenide tetrahedra is also present in all iron based superconductors. $La_3Pd_4Ge_4$ is superconducting with $T_c$ = 2.75 K[101]. By partly substituting Pd by Fe atoms the concentration of the charge carriers was modified assuming to hereby improve the superconducting properties. For low Fe concentrations samples of good quality could be obtained by arc melting the elements at temperatures exceeding 3273 K. For nominal $x \leq 1.0$ solely Pd atoms on tetrahedrally coordinated sites were substituted by iron. Measurements of the electric resistivity and magnetism characterized the samples with $x \leq 1.5$ as metals but no superconducting behavior was observed down to a temperature of 1.8 K.

## Zr*M*As (*M* = Ti, V) and $Zr_{1+x}V_{1-x}As$

The compounds Zr*M*As (*M* = Ti, V) crystallize in the CeScSi type structure, in which the 3*d* metals *M* are coordinated by 4 As atoms, forming distorted square planes[107, 108]. Contrary to the superconducting iron arsenides, the structure of Zr*M*As is rather three-dimensional since the metal-arsenide layers are not well separated by other layers or atoms. A similarity can be found in the strong metal–metal bonds of the 3*d* metal atoms and the fact that the states around the Fermi Energy are mainly composed of *M d* states, thus being responsible for the supposed metallic character of these compounds[107, 108]. To reveal the true physical properties, high quality samples were synthesized by arc-melting pre-reacted

element mixtures. The theoretically predicted metallic character of these metal rich arsenides could be confirmed by measurements of the electric resistivity and magnetism. Additionally, the influence of a varying charge carrier concentration in the series $Zr_{1+x}V_{1-x}As$ ($x$ = 0.20-0.35)[108], which can be understood as directly hole-doped VAs-layers, was investigated. It was shown that Zr doping in ZrVAs does not lead to a significant change of the physical properties. The obtained compounds are still metallic, though showing higher resistivity values, which is probably due to the increased inhomogeneity of the samples and / or the increased disorder within the VAs-layers.

## $LaFeAsO_{1-x}F_x$ ($x$ = 0-0.15) via a solid state metathesis reaction

A solid state metathesis reaction route was developed for the synthesis of $LaFeAsO_{1-x}F_x$[15]. The parent compound LaFeAsO was obtained by using LaOCl and NaFeAs as starting materials, which consist of the same structural motifs as the targeted compound. The investigation of the reaction pathway by means of temperature-dependent X-ray diffraction showed that the reaction proceeds via intermediate binary products and is not of topotactic nature. For the synthesis of fluoride doped samples, $LaF_3$ was used as F source. Compared to conventional syntheses the sample quality was improved drastically, with less than only 2 wt% of impurity phases in the F doped samples. The *in situ* formation of the binary intermediate products is most likely the reason for the better homogeneity of the reaction mixture and the consequentially improved sample quality. Measurements of the physical properties confirmed the structural and magnetic phase transitions of the parent compound LaFeAsO[39, 127] and the superconducting properties of the F doped samples.

## CaFeAsF and $Ca_{0.4}Nd_{0.6}FeAsF$ via solid state metathesis reaction

The general suitability of the synthesis of 1111 iron-arsenide compounds via solid state metathesis reaction was proven by expanding its applicability to the CaFeAsF system[23]. LaOCl was replaced by isotypic CaFCl as a starting material. The

structural conditions of the targeted product CaFeAsF lead to a halide selective reaction of NaFeAs and CaFCl, since only NaCl is obtained as co-product of the metathesis reaction. In a one step synthesis CaFeAsF was obtained with only small amounts of impurities. Resistivity and susceptibility measurements confirmed the reported anomaly at 118 K, which Nomura *et al.* attributed to the same structural transition as it was found for LaFeAsO[128]. Despite the good results achieved for the parent compound, it was very difficult to obtain samples containing Nd doped CaFeAsF, which was reported to have a very high $T_c$ of 56K[27]. The targeted compounds were only obtained in small amounts due to the formation of very stable side products like NdAs and $CaF_2$.

## Co-substituted $LaFe_{1-x}Mn_xAsO_{1-y}F_y$

An extensive study of the physical and structural properties of directly hole-doped $LaFe_{1-x}Mn_xAsO$ ($x$ = 0.05-0.20) and charge compensated / electron-doped $LaFe_{0.9}Mn_{0.1}AsO_{1-y}F_y$ ($y$ = 0.1-0.5) has been created by means of (temperature-dependent) powder X-ray-diffraction, resistivity measurements and magnetic characterizations ($\mu$SR measurements). Samples of good quality could be obtained, using a solid state metathesis reaction. The reported semiconducting properties of $LaFe_{1-x}Mn_xAsO$[48] were confirmed whereby the metallic character is increased upon further F doping in $LaFe_{0.9}M_{0.1}AsO$. No superconducting signal was observed within the whole series $LaFe_{0.9}Mn_{0.1}AsO_{1-y}F_y$, although the electronic (in terms of charge doping) and allegedly structural preconditions were found to be fulfilled. The magnetic characterization of $LaFe_{1-x}Mn_xAsO$ by the $\mu$SR technique revealed static short range magnetic order. Interestingly, in F doped $LaFe_{0.9}Mn_{0.1}AsO_{1-y}F_y$ ($y$ = 0.1 and 0.2) the static short range magnetism is quickly suppressed ($y$ = 0.1). The observation of an essentially non-magnetic state for a charge compensated sample is astonishing since it is completely different from $Ba_{1-x}K_xFe_{1.86}Co_{0.14}As_2$ ($x \approx$ 0.14), where the magnetism of the parent compound is regained for the charge compensated composition[53]. The allegedly optimally electron doped $LaFe_{0.9}Mn_{0.1}AsO_{0.8}F_{0.2}$ shows very weak dynamic short range magnetism below 5 K.

Thus although the magnetic transition is suppressed and the electron count should lead to a superconducting state, the latter is not observed down to low temperatures. It was proposed, that in such a case the localized Mn moments could act as pair breakers for the Cooper pairs and therefore act destructive to the emergence of superconductivity[135, 139, 143]. Finally, the study about $LaFe_{1-x}Mn_xAsO_{1-y}F_y$ shows that there are much more complicated correlations of electronic, magnetic and structural degrees of freedom to superconductivity than thought to be.

## Solid state metathesis reaction and building block concept

Although the solid state metathesis reactions presented in this thesis are most likely not of a topochemic character, which has been shown for the synthesis of LaFeAsO, the use of starting materials which consist of similar building units as the targeted compounds can be very useful (*building block concept*). Figure 8.1 gives an overview of the developed solid state metathesis reactions, together with some hypothetical approaches which can be imagined to be successful.

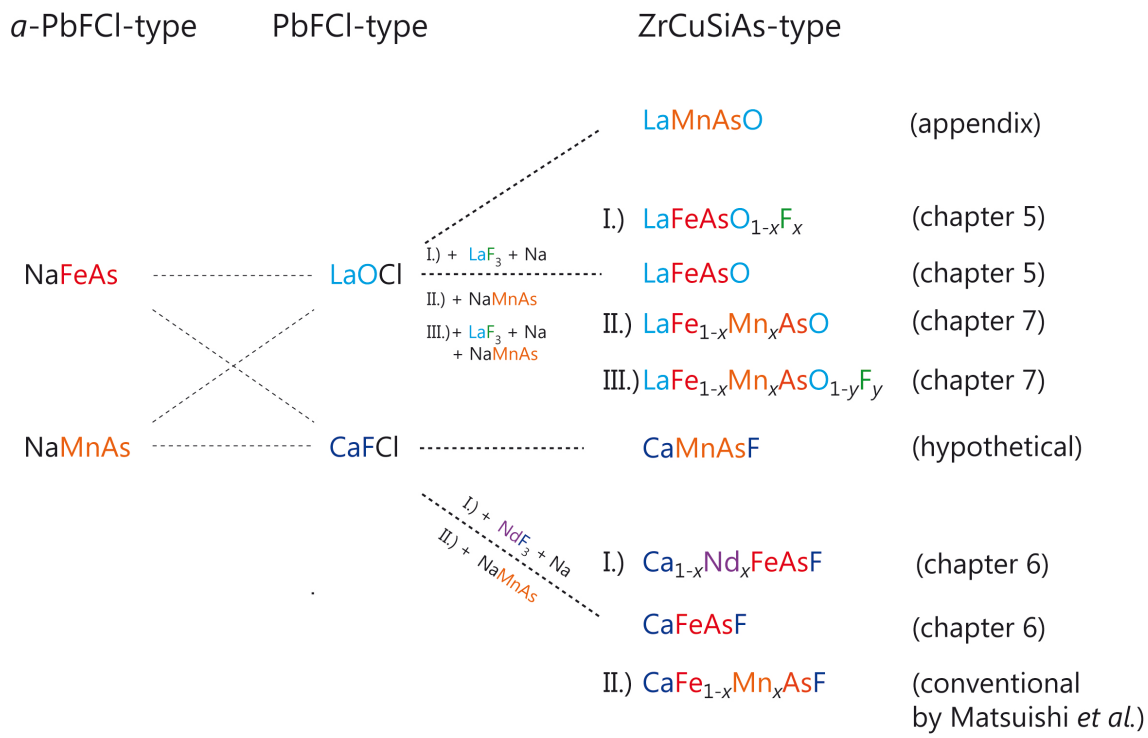


**Figure 8.1:** Schematic overview of the successfully used solid state metathesis reactions and theoretical approaches for the synthesis of CaMnAsF and $CaFe_{1-x}Mn_xAsF$. It has to be noted, that $CaFe_{1-x}Mn_xAsF$ has been conventionally synthesized by Matsuishi *et al.*[144].

As can be seen, choosing the appropriate compounds keeps the total number of reactants low. This is particularly evident for the synthesis of the undoped parent compounds, which have been synthesized by the reaction of only 2 starting materials. Another advantage of the building block concept can be seen, when it comes to reaction planning. As an example, the $LaFe_{1-x}Mn_xAsO$ series was simply synthesized by combining NaFeAs and isostypic NaMnAs at the desired composition, which in turn left the total number of staring materials low again. Another example is the synthesis of the hypothetical compound CaMnAsF, which can easily be imagined to be synthesized out of NaMnAs and CaFCl. Thus the concept of the presented solid state metathesis reactions can be a very helpful tool to synthesize a great variety of 1111 iron-arsenide compounds and their doped derivatives in good sample quality.

## Conclusion

The results of this thesis can be divided into three major topics, which can also be seen as different approaches of solid state chemistry to reveal interesting features of known and unknown compounds and to develop alternative synthesis routes.

Firstly, known compounds with related structural motifs to the superconducting iron-arsenides were investigated regarding their structural and physical properties. In case of $La_3Pd_4Ge_4$ the influence of Fe doping on the properties was studied, whereas in the series Zr*M*As (*M* = Ti, V) the physical properties have not yet been reported at all and were investigated for the first time.

Secondly, an alternative synthesis route has been developed for the synthesis of superconducting $LaFeAsO_{1-x}F_x$. This solid state metathesis reaction distinctly increased the quality of the samples compared to conventionally prepared products. Furthermore, the reaction pathway was investigated and clarified, which helps to understand the processes during high temperature solid state metathesis reactions in general.

Thirdly, this alternative synthesis route was expanded to other systems and new compounds like co-substituted $LaFe_{1-x}Mn_xAsO_{1-y}F_y$ were prepared and thoroughly investigated. This led to a complex study of the interplay of magnetism, electronic and structural conditions and the occurrence of superconducting properties. The investigation and understanding of such complex coherences will probably be decisive for the further understanding of the superconducting mechanism in iron based superconductors.

# A. Appendix

## A.1 Rietveld refinement of $LaGe_{2-x}Pd_x$

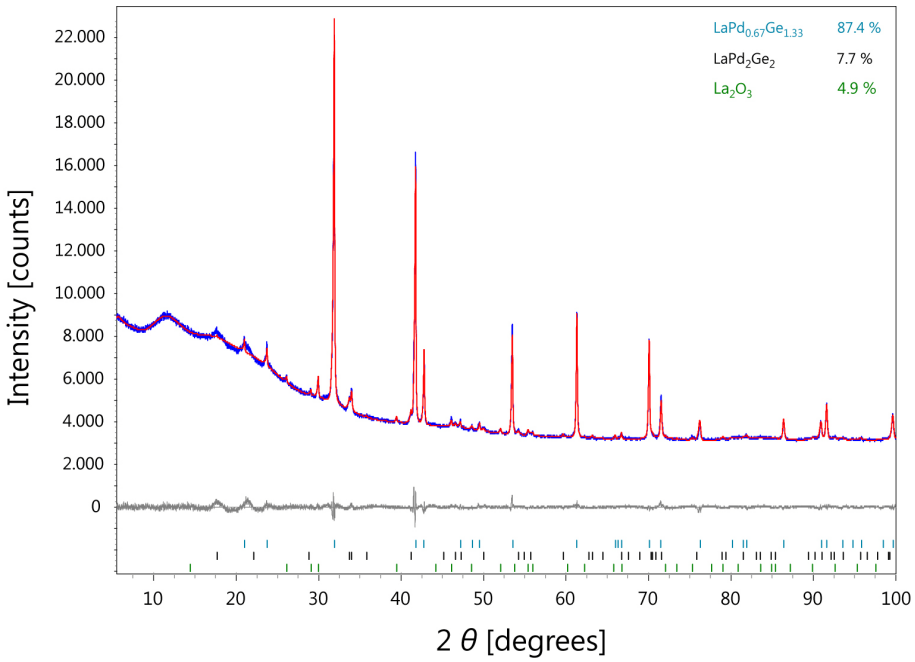


**Figure A.1:** Rietveld refinement of $LaGe_{2-x}Pd_x$ (spacegroup *P6/mmm*)

**Table A.1:** Crystallographic data of $LaGe_{2-x}Pd_x$ obtained from the Rietveld refinement.

| | | | | | | |
|---|---|---|---|---|---|---|
| Diffractometer | | HUBER G670, Cu-$K_{\alpha1}$, flat sample holder | | | | |
| Spacegroup | | *P6/mmm* (191), $Z$ = 1 | | | | |
| Lattice parameters | | $a = b$ = 432.1 (1) pm; $c$ = 422.7(1) pm | | | | |
| Cell volume | | 68.34(1) Å$^3$ | | | | |
| $R_p$, $R_{wP}$, $R_{Bragg}$, $\chi^2$ | | 1.011, 1.407, 0.837, 0.912 | | | | |
| **Atom** | **Site** | ***x*** | ***y*** | ***z*** | **Occ.** | **$U_{iso}$ [pm$^2$]** |
| La | 1*a* | 0 | 0 | 0 | 1 | 206(5) |
| Ge | 2*d* | 1/3 | 2/3 | 1/2 | 0.64(1) | 216(6) |
| Pd | 2*d* | 1/3 | 2/3 | 1/2 | 0.36(1) | 216(6) |
| Detected phases | | $LaGe_{1.28(1)}Pd_{0.72(1)}$ (87 wt%), $LaPd_2Ge_2$ (8 wt%), $La_2O_3$ (5 wt%) | | | | |

## A.2 Additional data for Zr*M*As (*M* = V, Ti) and $Zr_{1+x}V_xAs$

**Table A.2:** Crystallographic data of ZrTiAs from single crystal diffraction.

| | | | | |
|---|---|---|---|---|
| Nominal composition | ZrTiAs | | | |
| Refined composition | $Zr_{0.99(1)}Ti_{0.95(1)}As$ | | | |
| Temperature | 293 K | | | |
| Diffractometer | Stoe IPDS | | | |
| Radiation | Mo.$K_\alpha$, λ = 0.71073 Å | | | |
| Space group | *I*4/*mmm* (139) | | | |
| Lattice parameters [pm] | $a = b$ = 376.8 (1) pm; $c$ = 1478.4 (5) pm | | | |
| Cell volume [Å$^3$] | 209.92(6) Å$^3$ | | | |
| $Z$ | 4 | | | |
| Calculated density | 6.77 g/cm$^3$ | | | |
| Absorption coefficient | 23.913 mm$^{-1}$ | | | |
| 2$\theta$ range | 2.76 – 30.20 | | | |
| Reflections (total) | 725 | | | |
| Reflections (independent) | 122 | | | |
| Reflections with I > 2σ(I) | 113 | | | |
| Refined Parameters | 13 | | | |
| $R_{int}$, $R_\sigma$ | 0.046, 0.027 | | | |
| $R_1$, $wR_2$ [I > 2σ(I)] | 0.019, 0.039 | | | |
| $R_1$, $wR_2$ [all data] | 0.020, 0.040 | | | |
| Goodness of fit (GooF) | 1.125 | | | |
| Largest resid. peak, hole | 0.816 e$^-$/Å$^3$, -1.564 e$^-$/Å$^3$ | | | |
| Atomic parameters, with atomic displacement parameters $U$ in pm$^2$: | | | | |
| Zr | 4*e* (0,0,*z*) | $z$ = 0.3209(1) | occ. 0.99(1) | $U_{11} = U_{22}$ = 68(3); $U_{33}$ = 63(3) |
| Ti | 4*c* (0, ½,0) | | occ. 0.95(1) | $U_{11}$ = 140 (1) $U_{22}$ = 83(7); $U_{33}$ = 47(6) |
| As | 4*e* (0,0,*z*) | $z$ = 0.1300(1) | occ. 1 | $U_{11} = U_{22}$ = 65(3); $U_{33}$ = 61(3) |

**Table A.3:** Crystallographic data of ZrTiAs obtained from the Rietveld refinement.

| Diffractometer | | STOE STADI P, Mo-$K_{\alpha1}$, flat sample holder | | | | |
|---|---|---|---|---|---|---|
| Spacegroup | | *I*4/*mmm* (139), *Z* = 4 | | | | |
| Lattice parameters | | *a* = *b* = 376.8 (1) pm; *c* = 1474.5(1) pm | | | | |
| Cell volume | | 209.3(7) Å$^3$ | | | | |
| $R_p$, $R_{wP}$, $R_{Bragg}$, $\chi^2$ | | 2.523, 3.214, 1.550, 1.124 | | | | |
| **Atom** | **Site** | ***x*** | ***y*** | ***z*** | **Occ.** | **$U_{iso}$ [pm$^2$]** |
| Zr | 4*e* | 0 | 0 | 0.3211(2) | 0.99(4) | 27(3) |
| Ti | 4*c* | 0 | ½ | 0 | 0.96(1) | 50(5) |
| As | 4*e* | 0 | 0 | 0.1297(2) | 1 | 32(3) |
| Detected phases | | $ZrTi_{0.96(1)}As$ (100 wt%) | | | | |

**Table A.4:** Crystallographic data of ZrVAs obtained from the Rietveld refinement.

| Diffractometer | | STOE STADI P, Mo-$K_{\alpha1}$, flat sample holder | | | | |
|---|---|---|---|---|---|---|
| Spacegroup | | *I*4/*mmm* (139), *Z* = 4 | | | | |
| Lattice parameters | | *a* = *b* = 376.8 (1) pm; *c* = 1411.7(1) pm | | | | |
| Cell volume | | 200.3(1) Å$^3$ | | | | |
| $R_p$, $R_{wP}$, $R_{Bragg}$, $\chi^2$ | | 2.389, 3.658, 1.048, 1.175 | | | | |
| **Atom** | **Site** | ***x*** | ***y*** | ***z*** | **Occ.** | **$U_{iso}$ [pm$^2$]** |
| Zr | 4*e* | 0 | 0 | 0.3266(2) | 1.00(1) | 81(5) |
| V | 4*c* | 0 | ½ | 0 | 0.98(1) | 91(8) |
| As | 4*e* | 0 | 0 | 0.1278(2) | 1 | 72(5) |
| Detected phases | | $ZrV_{0.98(1)}As$ (98.4 wt%), ZrAs (1.6 wt%) | | | | |

**Table A.5:** Crystallographic data of $Zr_{1.20}V_{0.80}As$ obtained from the Rietveld refinement.

| Diffractometer | | STOE STADI P, Mo-$K_{\alpha1}$, flat sample holder | | | | |
|---|---|---|---|---|---|---|
| Spacegroup | | *I*4/*mmm* (139), *Z* = 4 | | | | |
| Lattice parameters | | *a* = *b* = 377.4 (1) pm; *c* = 1433.3(1) pm | | | | |
| Cell volume | | 204.1(1) Å$^3$ | | | | |
| $R_p$, $R_{wP}$, $R_{Bragg}$, $\chi^2$ | | 2.660, 3.621, 0.811, 2.013 | | | | |
| **Atom** | **Site** | ***x*** | ***y*** | ***z*** | **Occ.** | **$U_{iso}$ [pm$^2$]** |
| Zr1 | 4*e* | 0 | 0 | 0.3239(2) | 1.00(1) | 95(6) |
| V | 4*c* | 0 | ½ | 0 | 0.80(1) | 140(9) |
| Zr2 | 4*c* | 0 | ½ | 0 | 0.20(1) | 140(9) |
| As | 4*e* | 0 | 0 | 0.1282(2) | 1 | 64(6) |
| Detected phases | | $Zr_{1.20(1)}V_{0.80(1)}As$ (main phase) + small unidentified peaks | | | | |

**Table A.6:** Crystallographic data of $Zr_{1.25}V_{0.75}As$ obtained from the Rietveld refinement.

| Diffractometer | | STOE STADI P, Mo-$K_{\alpha1}$, flat sample holder | | | | |
|---|---|---|---|---|---|---|
| Spacegroup | | *I*4/*mmm* (139), *Z* = 4 | | | | |
| Lattice parameters | | *a* = *b* = 377.0 (1) pm; *c* = 1434.2(1) pm | | | | |
| Cell volume | | 203.9(1) Å$^3$ | | | | |
| $R_p$, $R_{wP}$, $R_{Bragg}$, $\chi^2$ | | 2.431, 3.314, 0.511, 2.086 | | | | |
| **Atom** | **Site** | ***x*** | ***y*** | ***z*** | **Occ.** | **$U_{iso}$ [pm$^2$]** |
| Zr1 | 4*e* | 0 | 0 | 0.3266(2) | 1.00(1) | 92(6) |
| V | 4*c* | 0 | ½ | 0 | 0.71(1) | 231(10) |
| Zr2 | 4*c* | 0 | ½ | 0 | 0.29(1) | 231(10) |
| As | 4*e* | 0 | 0 | 0.1278(2) | 1 | 82(6) |
| Detected phases | | $Zr_{1.29(1)}V_{0.71(1)}As$ (main phase) + small unidentified peaks | | | | |

**Table A.7:** Crystallographic data of $Zr_{1.35}V_{0.65}As$ obtained from the Rietveld refinement.

| | | | | | | |
|---|---|---|---|---|---|---|
| Diffractometer | | STOE STADI P, Mo-$K_{\alpha1}$, flat sample holder | | | | |
| Spacegroup | | *I*4/*mmm* (139), *Z* = 4 | | | | |
| Lattice parameters | | *a* = *b* = 378.2(1) pm; *c* = 1457.4(2) pm | | | | |
| Cell volume | | 208.4(1) Å$^3$ | | | | |
| $R_p$, $R_{wP}$, $R_{Bragg}$, $\chi^2$ | | 2.441, 3.122, 0.780, 1.228 | | | | |
| **Atom** | **Site** | ***x*** | ***y*** | ***z*** | **Occ.** | **$U_{iso}$ [pm$^2$]** |
| Zr1 | 4*e* | 0 | 0 | 0.3226(2) | 1.00(1) | 112(5) |
| V | 4*c* | 0 | ½ | 0 | 0.64(1) | 256(10) |
| Zr2 | 4*c* | 0 | ½ | 0 | 0.36(1) | 256(10) |
| As | 4*e* | 0 | 0 | 0.1315(2) | 1 | 91(5) |
| Detected phases | | $Zr_{1.36(1)}V_{0.64(1)}As$ (main phase) + small unidentified peaks | | | | |

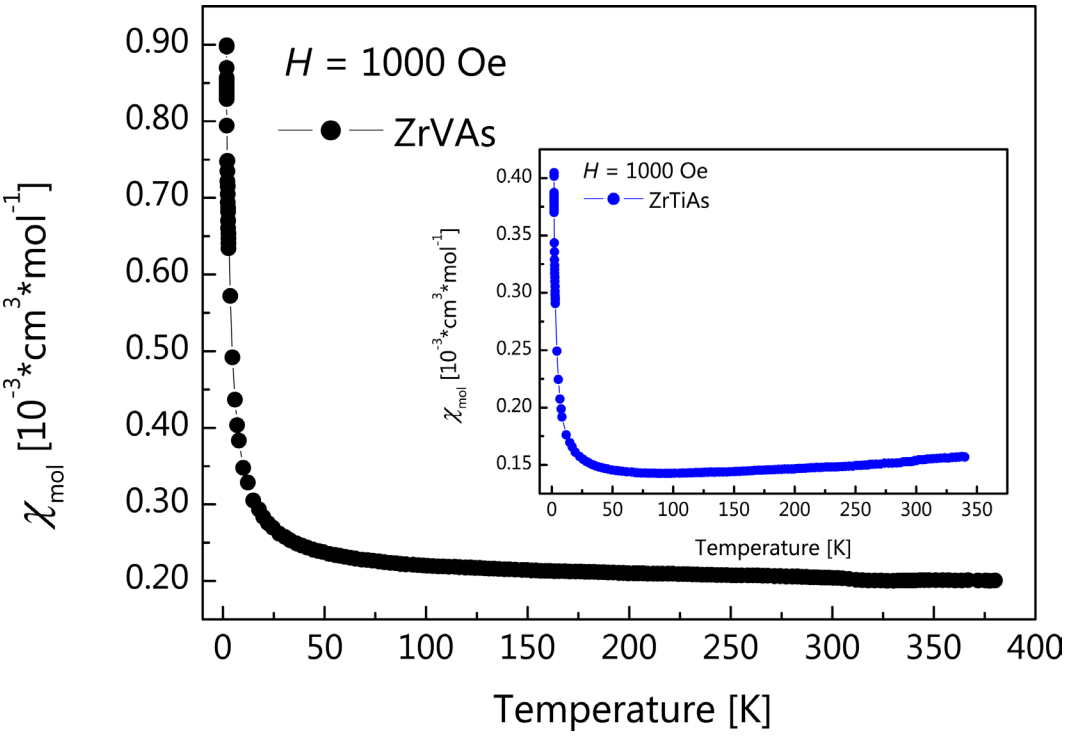


**Figure A.2:** Measurement of the magnetic susceptibility versus temperature with an applied field of 1000 Oe for Zr*M*As (*M* = Ti, V)

## A.3 Rietveld refinement of $LaFeAsO_{0.9}F_{0.1}$

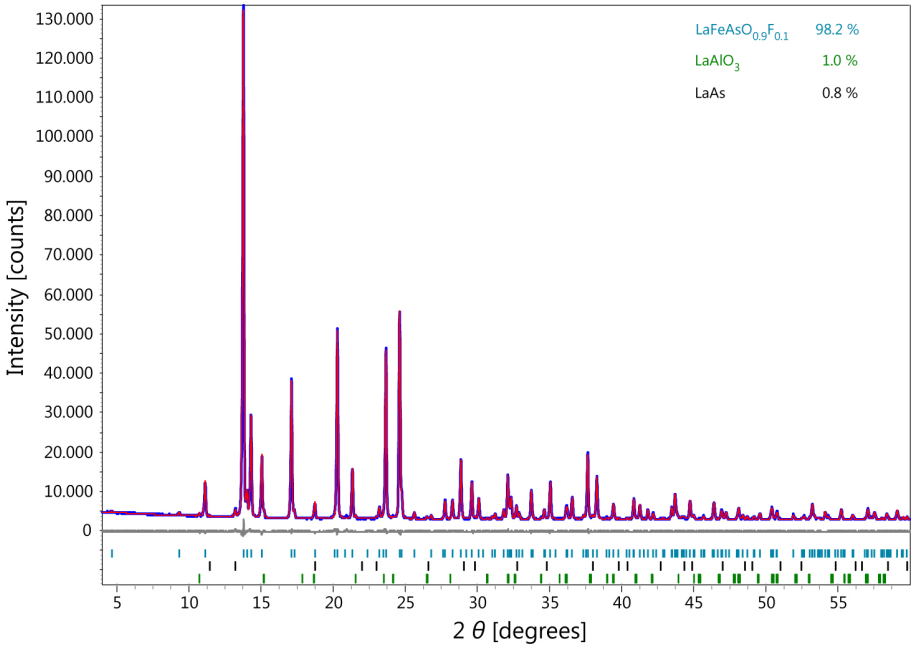


**Figure A.3:** Rietveld refinement of $LaFeAsO_{0.9}F_{0.1}$ (spacegroup *P*4/*nmm*) on the STOE STADI P data.

**Table A.8:** Crystallographic data of $LaFeAsO_{0.9}F_{0.1}$ obtained from the Rietveld refinement.

| | | | | | | |
|---|---|---|---|---|---|---|
| Diffractometer | | STOE STADI P, Mo-$K_{\alpha1}$, flat sample holder | | | | |
| Spacegroup | | *P*4/*nmm* (129) (*o*2), *Z* = 2 | | | | |
| Lattice parameters | | *a* = *b* = 402.6 (1) pm; *c* = 871.2(1) pm | | | | |
| Cell volume | | 141.2(1) Å$^3$ | | | | |
| $R_p$, $R_{wP}$, $R_{Bragg}$, $\chi^2$ | | 1.524, 2.012, 0.476, 1.373 | | | | |
| **Atom** | **Site** | ***x*** | ***y*** | ***z*** | **Occ.** | **$U_{iso}$ [pm$^2$]** |
| La | 2*c* | ¼ | ¼ | 0.6459(1) | 1 | 55(1) |
| Fe | 2*a* | ¾ | ¼ | 0 | 1 | 58(2) |
| As | 2*c* | ¼ | ¼ | 0.1528(2) | 1 | 53(1) |
| O | 2*b* | ¾ | ¼ | ½ | 0.9 | 15(9) |
| F | 2*b* | ¾ | ¼ | ½ | 0.1 | 15(9) |
| Detected phases | | $LaFeAsO_{0.9}F_{0.1}$ (98 wt%), $LaAlO_3$ (1 wt%), LaAs (1 wt%) | | | | |

## A.4 Additional data for CaFeAsF and $Ca_{0.4}Nd_{0.6}FeAsF$

**Table A.9:** Crystallographic data of CaFeAsF obtained from the Rietveld refinement (see chapter 6).

| Diffractometer | HUBER G670, Cu-$K_{\alpha1}$, flat sample holder | | | | | |
|---|---|---|---|---|---|---|
| Spacegroup | *P*4/*nmm* (129) (o2), *Z* = 2 | | | | | |
| Lattice parameters | *a* = *b* = 387.5 (1) pm; *c* = 858.3(1) pm | | | | | |
| Cell volume | 128.9(1) Å$^3$ | | | | | |
| $R_p$, $R_{wP}$, $R_{Bragg}$, $\chi^2$ | 1.128, 1.476, 0.153, 0.924 | | | | | |
| **Atom** | **Site** | ***x*** | ***y*** | ***z*** | **Occ.** | **$U_{iso}$ [pm$^2$]** |
| Ca | 2*c* | ¼ | ¼ | 0.6511(4) | 1 | 92(6) |
| Fe | 2*a* | ¾ | ¼ | 0 | 1 | 48(6) |
| As | 2*c* | ¼ | ¼ | 0.1654(2) | 1 | 63(4) |
| F | 2*b* | ¾ | ¼ | ½ | 1 | 22(12) |
| Detected phases | CaFeAsF (97 wt%), $CaF_2$ (3 wt%), Fe (0.3 wt%) | | | | | |

**Table A.10:** Crystallographic data of $Ca_{0.4}Nd_{0.6}FeAsF$ (sample *b.*) obtained from the Rietveld refinement ($z_{Ca}$ and $z_{As}$ were taken from the refinement of CaFeAsF). The thermal displacement parameters $U_{iso}$ were constraint to 89 $pm^2$.

| Diffractometer | | HUBER G670, Cu-$K_{\alpha1}$, flat sample holder | | | |
|---|---|---|---|---|---|
| Spacegroup | | *P4/nmm* (129) (*o2*), *Z* = 2 | | | |
| Lattice parameters | | *a* = *b* = 394.9 (2) pm; *c* = 855.2(4) pm | | | |
| Cell volume | | 133.4(2) Å$^3$ | | | |
| $R_p$, $R_{wP}$, $R_{Bragg}$, $\chi^2$ | | 1.312, 1.992, 0.747, 1.653 | | | |
| **Atom** | **Site** | ***x*** | ***y*** | ***z*** | **Occ.** |
| Ca | 2*c* | ¼ | ¼ | 0.6511 | 0.4 |
| Nd | 2*c* | ¼ | ¼ | 0.6511 | 0.6 |
| Fe | 2*a* | ¾ | ¼ | 0 | 1 |
| As | 2*c* | ¼ | ¼ | 0.1654 | 1 |
| F | 2*b* | ¾ | ¼ | ½ | 1 |
| Detected phases | | $CaF_2$ (23 wt%), NdAs (21 wt%), NaCl (17 wt%), NaF (27 wt%), $NaNdF_4$ (5 wt%), $Ca_{0.4}Nd_{0.6}FeAsF$ (4 wt%), $Fe_2As$ (3 wt%) | | | |

**Table A.11:** Crystallographic data of $Ca_{0.4}Nd_{0.6}FeAsF$ (sample *e.*) obtained from the Rietveld refinement ($z_{Ca}$ and $z_{As}$ were taken from the refinement of CaFeAsF). The thermal displacement parameters $U_{iso}$ were constraint to 89 $pm^2$.

| Diffractometer | | HUBER G670, Cu-$K_{\alpha1}$, flat sample holder | | | |
|---|---|---|---|---|---|
| Spacegroup | | *P4/nmm* (129) (*o2*), *Z* = 2 | | | |
| Lattice parameters | | *a* = *b* = 394.7 (4) pm; *c* = 854.5(8) pm | | | |
| Cell volume | | 133.1(6) Å$^3$ | | | |
| $R_p$, $R_{wP}$, $R_{Bragg}$, $\chi^2$ | | 1.575, 2.218, 0.427, 0.880 | | | |
| **Atom** | **Site** | ***x*** | ***y*** | ***z*** | **Occ.** |
| Ca | 2*c* | ¼ | ¼ | 0.6511 | 0.4 |
| Nd | 2*c* | ¼ | ¼ | 0.6511 | 0.6 |
| Fe | 2*a* | ¾ | ¼ | 0 | 1 |
| As | 2*c* | ¼ | ¼ | 0.1654 | 1 |
| F | 2*b* | ¾ | ¼ | ½ | 1 |
| Detected phases | | $CaF_2$ (23 wt%), $NaNdF_4$ (11 wt%), NdAs (9 wt%), $Fe_2As$(10 wt%), NaCl (17 wt%), NaF (26 wt%), $Ca_{0.4}Nd_{0.6}FeAsF$ (4 wt%) | | | |

# A.5 Synthesis of LaMnAsO

Since LaMnAsO represents one end of the solid solution $LaFe_{1-x}Mn_xAsO$, discussed in chapter 7, it was decided to synthesize the Mn containing parent compound via solid state metathesis reaction. Furthermore the latter served as test for the usage of NaMnAs as starting material. LaMnAsO is isotypic to LaFeAsO and crystallizes in the ZrCuSiAs-type structure (spacegroup*P*4/*nmm* (#129))[149]. LaMnAsO is antiferromagnetic (Néel-type) with $T_N$ = 317 K, which was found from neutron and synchrotron diffraction studies[147, 150]. Additionally LaMnAsO shows semiconducting behavior and giant magnetorresistance (GMR)[147].

### *A.5.1 Synthesis*

LaMnAsO was synthesized by heating stoichiometric amounts of LaOCl and NaMnAs according to the solid-state metathesis reaction:

$$LaOCl + NaMnAs \rightarrow LaMnAsO + NaCl$$

The reaction mixture was heated to 1023 K for 48 h and 1223 K for 96 h, followed by cooling to room temperature with 300 K/h. The co-formed NaCl was removed by washing the obtained mixture with water (3 times) and ethanol, followed by drying the product under high vacuum.

### *A.5.2 Rietveld refinement of LaMnAsO*

The Rietveld refinement of LaMnAsO revealed small amounts of LaOCl as side phase and additionally some very small unidentified peaks (see Figure A.4). The obtained lattice parameters (Table A.12) are consistent with the ones obtained by Jeitschko *et al.* ($a$ = 412.4, $c$ = 903.0)[149, 151].

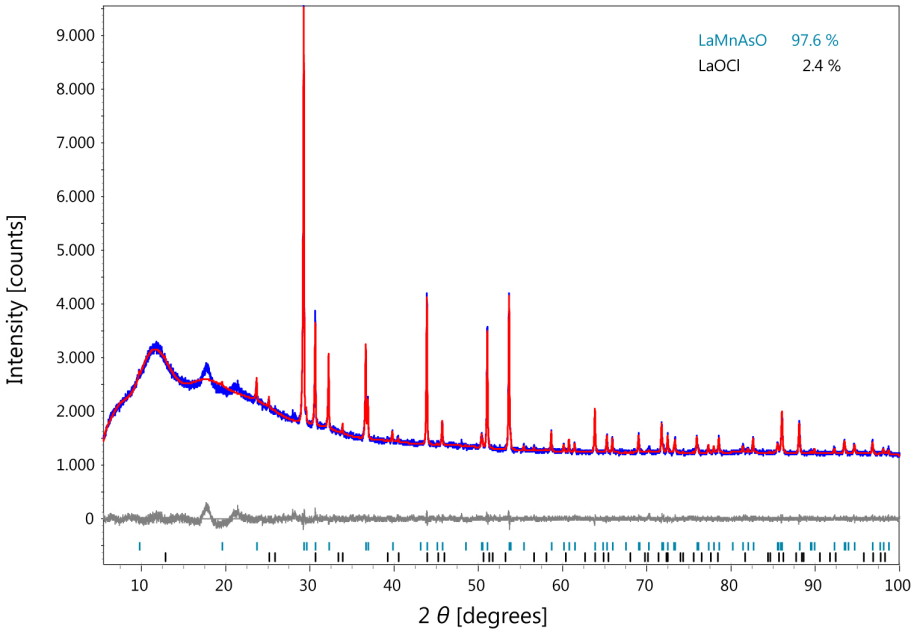


**Figure A.4:** Rietveld refinement of LaMnAsO (spacegroup *P*4/*nmm*).

**Table A.12:** Crystallographic data of LaMnAsO obtained from the Rietveld refinement.

| Diffractometer | | HUBER G670, Cu-$K_{\alpha1}$, flat sample holder | | | | |
|---|---|---|---|---|---|---|
| Spacegroup | | *P*4/*nmm* (129) (*o*2), *Z* = 2 | | | | |
| Lattice parameters | | *a* = *b* = 411.9 (1) pm; *c* = 904.4(1) pm | | | | |
| Cell volume | | 153.4(1) Å$^3$ | | | | |
| $R_p$, $R_{wP}$, $R_{Bragg}$, $\chi^2$ | | 1.497, 1.985, 0.367, 0.804 | | | | |
| **Atom** | **Site** | ***x*** | ***y*** | ***z*** | **Occ.** | **$U_{iso}$ [pm$^2$]** |
| La | 2*c* | ¼ | ¼ | 0.6325(1) | 1 | 153(4) |
| Mn | 2*a* | ¾ | ¼ | 0 | 1 | 214(9) |
| As | 2*c* | ¼ | ¼ | 0.1683(1) | 1 | 140(7) |
| O | 2*b* | ¾ | ¼ | ½ | 1 | 62(30) |
| Detected phases | | LaMnAsO(98 wt%), LaOCl (2 wt%), | | | | |

### *A.5.3 Resistivity measurement*

The performed resistivity measurement (Figure A.5) confirmed the previously reported semiconducting behavior of LaMnAsO[147].

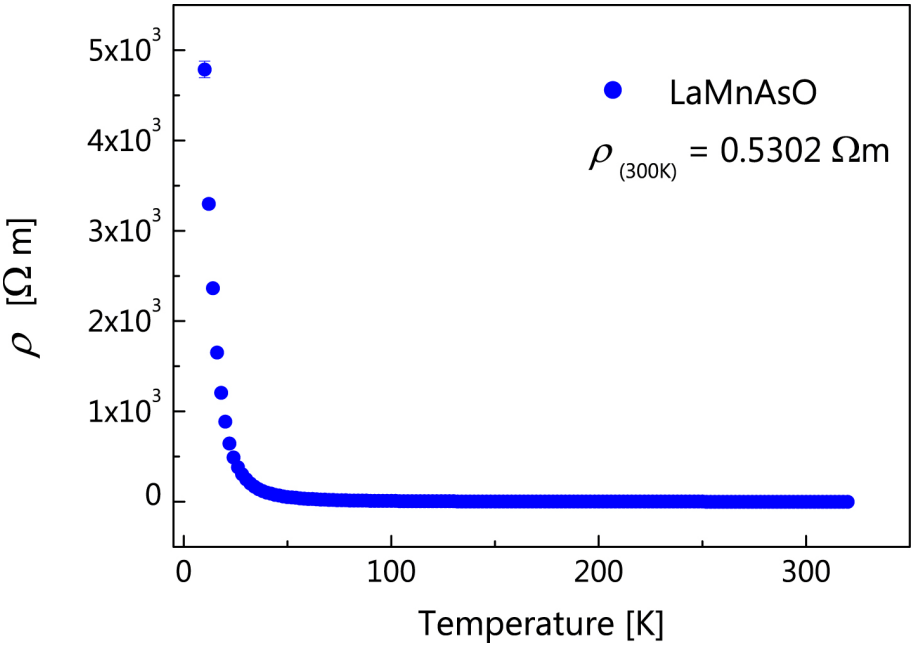


**Figure A.5**: Temperature dependence of the electrical resistivity $\rho$ of LaMnAsO.

# Abbreviations

| Abbreviation | Expression / Word |
|---|---|
| 2θ | diffraction angle |
| $4\pi\chi_V$ | magnetic (e. g. superconducting) volume fraction |
| ° | degree |
| Ø | diameter |
| A | Ampere |
| Å | Ångstrøm |
| AC | alternating current |
| *AE* | alkaline earth metal |
| AFM | antiferromagnetic |
| BCS | acronym of Bardeen, Cooper, Schrieffer |
| CGS | centimeter gram second |
| $e^-$ | electron(s) |
| EDX | engergy dispersive X-ray analysis |
| $E_f$ | Fermi energy |
| eq. | equivalents |
| *et al.* | et alii ("*and others*") |
| fc | field-cooled |
| h | hour |
| *H* | magnetic field |
| $H_{c1}$ | lower critical field |
| $H_{c2}$ | upper critical field |
| IPDS | imaging plate diffraction system |
| K | Kelvin |
| mg | milligram |
| $M_{mol}$ | magnetization per mole |
| MPMS | magnetic property measurement system |
| nm | nanometer |

| | |
|---|---|
| NMR | nuclear magnetic resonance |
| *o2* | origin choice 2 |
| occ. | atom site occupancy |
| Oe | Ørsted |
| pm | picometer |
| *RE* | rare earth metal |
| SDW | spin-density wave |
| SQUID | superconducting quantum interference device |
| SSM | solid state metathesis |
| T | Tesla |
| $T_c$ | critical temperature |
| TF | transverse field |
| $T_N$ | Néel temperature |
| $T_s$ | structural transition temperature |
| *V* | Volume |
| wt% | weight percent |
| XRD | X-ray diffraction |
| YBCO | $YBa_2Cu_3O_{7-x}$ |
| *Z* | Number of empirical formulas per unit cell |
| ZF | zero field |
| zfc | zero-field-cooled |
| $\lambda$ | wavelength |
| µSR | muon spin relaxation |
| $\chi$ | magnetic susceptibility per volume (equivalent to $\chi_V$) |
| $\chi^2$ | goodness of fit |
| $\chi_g$ | magnetic susceptibility per gram |
| $\chi_{mol}$ | magnetic susceptibility per mole |

# Bibliography


[1] Nopelprize.org - The Official Web Site of the Nobel Prize, http://www.nobelprize.org/nobel_prizes/physics/laureates/1913/onnes-lecture.pdf,

[2] S. Blundell, *Superconductivity - A Very Short Introduction*, Oxford University Press, Oxford, **2009**.

[3] B. T. Matthias, T. H. Geballe, S. Geller, E. Corenzwit, *Physical Review* **1954**, *95*, 1435.

[4] B. T. Matthias, T. H. Geballe, R. H. Willens, E. Corenzwit, G. W. Hull, Jr., *Physical Review* **1965**, *139*, A1501.

[5] W. Buckel, R. Kleiner, *Supraleitung - Grundlagen und Anwendungen, 6. Auflage*, Wiley-VCH Verlag GmbH &Co. KGaA, Weinheim, **2004**.

[6] B. T. Matthias, *Physical Review* **1955**, *97*, 74.

[7] Wikipedia, the free encyclopedia: Electromagnet, http://en.wikipedia.org/wiki/Electromagnet, **2013.**

[8] S. W. Van Sciver, K. R. Marken, *Physics Today* **2002**, *55*, 37.

[9] L. Rossi, *Superconductor Science and Technology* **2010**, *23*, 034001.

[10] J. G. Bednorz, K. A. Müller, *Zeitschrift für Physik B* **1986**, *64*, 189.

[11] M. K. Wu, J. R. Ashburn, C. J. Torng, P. H. Hor, R. L. Meng, L. Gao, Z. J. Huang, Y. Q. Wang, C. W. Chu, *Physical Review Letters* **1987**, *58*, 908.

[12] J. Bardeen, L. N. Cooper, J. R. Schrieffer, *Physical Review* **1957**, *106*, 162.

[13] M. Tegel, *Iron pnictide superconductors*, Dissertation thesis, Ludwig-Maximilians-Universität (München), **2011**.

[14] Y. Kamihara, H. Hiramatsu, M. Hirano, R. Kawamura, H. Yanagi, T. Kamiya, H. Hosono, *Journal of the American Chemical Society* **2006**, *128*, 10012.

[15] Y. Kamihara, T. Watanabe, M. Hirano, H. Hosono, *Journal of the American Chemical Society* **2008**, *130*, 3296.

[16] C. de la Cruz, Q. Huang, J. W. Lynn, J. Li, W. Ratcliff, J. L. Zarestky, H. A. Mook, G. F. Chen, J. L. Luo, N. L. Wang, P. Dai, *Nature* **2008**, *453*, 899.

[17] T. Nomura, S. W. Kim, Y. Kamihara, M. Hirano, P. V. Sushko, K. Kato, M. Takata, A. L. Shluger, H. Hosono, *Superconductor Science & Technology* **2008**, *21*, 125028.

[18] M. Rotter, M. Tegel, D. Johrendt, I. Schellenberg, W. Hermes, R. Pöttgen, *Physical Review B* **2008**, *78*, 020503.

[19] M. Pfisterer, G. Nagorsen, *Zeitschrift für Naturforschung B* **1983**, *38*, 811.

[20] M. Rotter, M. Tegel, D. Johrendt, *Physical Review Letters* **2008**, *101*, 107006.

[21] V. Johnson, W. Jeitschko, *Journal of Solid State Chemistry* **1974**, *11*, 161.

[22] P. Quebe, L. J. Terbuchte, W. Jeitschko, *Journal of Alloys and Compounds* **2000**, *302*, 70.

[23] X. Zhu, F. Han, P. Cheng, G. Mu, B. Shen, B. Zeng, H.-H. Wen, *Physica C* **2009**, *469*, 381.
[24] M. Tegel, S. Johansson, V. Weiss, I. Schellenberg, W. Hermes, R. Pöttgen, D. Johrendt, *Europhysics Letters* **2008**, *84*, 67007.
[25] S. Matsuishi, Y. Inoue, T. Nomura, M. Hirano, H. Hosono, *Journal of the Physical Society of Japan* **2008**, *77*, 113709.
[26] S. Matsuishi, Y. Inoue, T. Nomura, H. Yanagi, M. Hirano, H. Hosono, *Journal of the American Chemical Society* **2008**, *130*, 14428.
[27] P. Cheng, B. Shen, G. Mu, X. Zhu, F. Han, B. Zeng, H.-H. Wen, *Europhysics Letters* **2009**, *85*, 67003.
[28] M. J. Pitcher, D. R. Parker, P. Adamson, S. J. C. Herkelrath, A. T. Boothroyd, R. M. Ibberson, M. Brunelli, S. J. Clarke, *Chemical Communications* **2008**, 5918.
[29] D. R. Parker, M. J. Pitcher, P. J. Baker, I. Franke, T. Lancaster, S. J. Blundell, S. J. Clarke, *Chemical Communications* **2009**, 2189.
[30] J. H. Tapp, Z. Tang, B. Lv, K. Sasmal, B. Lorenz, P. C. W. Chu, A. M. Guloy, *Physical Review B* **2008**, *78*, 060505.
[31] F.-C. Hsu, J.-Y. Luo, K.-W. Yeh, T.-K. Chen, T.-W. Huang, P. M. Wu, Y.-C. Lee, Y.-L. Huang, Y.-Y. Chu, D.-C. Yan, M.-K. Wu, *Proceedings of the National Academy of Sciences* **2008**, *105*, 14262.
[32] K.-W. Yeh, T.-W. Huang, Y.-l. Huang, T.-K. Chen, F.-C. Hsu, P. M. Wu, Y.-C. Lee, Y.-Y. Chu, C.-L. Chen, J.-Y. Luo, D.-C. Yan, M.-K. Wu, *Europhysics Letters* **2008**, *84*, 37002.
[33] X. Zhu, F. Han, G. Mu, P. Cheng, B. Shen, B. Zeng, H.-H. Wen, *Physical Review B* **2009**, *79*, 220512.
[34] F. Ma, Z.-Y. Lu, *Physical Review B* **2008**, *78*, 033111.
[35] D. J. Singh, M. H. Du, *Physical Review Letters* **2008**, *100*, 237003.
[36] D. Johrendt, *Journal of Materials Chemistry* **2011**, *21*, 13726.
[37] J. Dong, H. J. Zhang, G. Xu, Z. Li, G. Li, W. Z. Hu, D. Wu, G. F. Chen, X. Dai, J. L. Luo, Z. Fang, N. L. Wang, *Europhysics Letters* **2008**, *83*, 27006.
[38] C. de la Cruz, Q. Huang, J. W. Lynn, J. Li, W. R. Ii, J. L. Zarestky, H. A. Mook, G. F. Chen, J. L. Luo, N. L. Wang, P. Dai, *Nature* **2008**, *453*, 899.
[39] T. Nomura, S. W. Kim, Y. Kamihara, M. Hirano, P. V. Sushko, K. Kato, M. Takata, A. L. Shluger, H. Hosono, *Superconductor Science and Technology* **2008**, *21*, 125028.
[40] G. Xu, H. Zhang, X. Dai, Z. Fang, *Europhysics Letters* **2008**, *84*, 67015.
[41] P. L. Alireza, Y. T. C. Ko, J. Gillett, C. M. Petrone, J. M. Cole, G. G. Lonzarich, S. E. Sebastian, *Journal of Physics: Condensed Matter* **2009**, *21*, 012208.
[42] H. Luetkens, H. H. Klauss, M. Kraken, F. J. Litterst, T. Dellmann, R. Klingeler, C. Hess, R. Khasanov, A. Amato, C. Baines, M. Kosmala, O. J. Schumann, M. Braden, J. Hamann-Borrero, N. Leps, A. Kondrat, G. Behr, J. Werner, B. Büchner, *Nature Materials* **2009**, *8*, 305.
[43] D. C. Johnston, *Advances in Physics* **2010**, *59*, 803.

[44] A. S. Sefat, R. Jin, M. A. McGuire, B. C. Sales, D. J. Singh, D. Mandrus, *Physical Review Letters* **2008**, *101*, 117004.
[45] A. S. Sefat, A. Huq, M. A. McGuire, R. Jin, B. C. Sales, D. Mandrus, L. M. D. Cranswick, P. W. Stephens, K. H. Stone, *Physical Review B* **2008**, *78*, 104505.
[46] M. G. Kim, A. Kreyssig, A. Thaler, D. K. Pratt, W. Tian, J. L. Zarestky, M. A. Green, S. L. Bud'ko, P. C. Canfield, R. J. McQueeney, A. I. Goldman, *Physical Review B* **2010**, *82*, 220503.
[47] A. Thaler, H. Hodovanets, M. S. Torikachvili, S. Ran, A. Kracher, W. Straszheim, J. Q. Yan, E. Mun, P. C. Canfield, *Physical Review B* **2011**, *84*, 144528.
[48] D. Bérardan, L. Pinsard-Gaudart, N. Dragoe, *Journal of Alloys and Compounds* **2009**, *481*, 470.
[49] R. Zhi-An, L. Wei, Y. Jie, Y. Wei, S. Xiao-Li, Zheng-Cai, C. Guang-Can, D. Xiao-Li, S. Li-Ling, Z. Fang, Z. Zhong-Xian, *Chinese Physics Letters* **2008**, *25*, 2215.
[50] J. Zhao, Q. Huang, C. de la Cruz, S. Li, J. W. Lynn, Y. Chen, M. A. Green, G. F. Chen, G. Li, Z. Li, J. L. Luo, N. L. Wang, P. Dai, *Nat Mater* **2008**, *7*, 953.
[51] C. H. Lee, A. Iyo, H. Eisaki, H. Kito, M. T. Fernandez-Diaz, T. Ito, K. Kihou, H. Matsuhata, M. Braden, K. Yamada, *Journal of the Physical Society of Japan* **2008**, *77*, 083704.
[52] C. Löhnert, T. Stürzer, M. Tegel, R. Frankovsky, G. Friederichs, D. Johrendt, *Angewandte Chemie International Edition* **2011**, *50*, 9195.
[53] V. Zinth, T. Dellmann, H.-H. Klauss, D. Johrendt, *Angewandte Chemie, International Edition* **2011**, *50*, 7919.
[54] G. R. Stewart, *Reviews of Modern Physics* **2011**, *83*, 1589.
[55] C. W. Chu, F. Chen, M. Gooch, A. M. Guloy, B. Lorenz, B. Lv, K. Sasmal, Z. J. Tang, J. H. Tapp, Y. Y. Xue, *Physica C-Superconductivity and Its Applications* **2009**, *469*, 326.
[56] G. Achenbach, H. U. Schuster, *Zeitschrift Für Anorganische Und Allgemeine Chemie* **1981**, *475*, 9.
[57] J. Hölsä, K. Koski, S. Makkonen, E. Säilynoja, H. Rahiala, *Journal of Alloys and Compounds* **1997**, *249*, 217.
[58] H. P. Beck, *Journal of Solid State Chemistry* **1976**, *17*, 275.
[59] *G670 Imaging Plate Guinier Camera*, v. 5.0 build 2, HUBER,
[60] *WinXPOW*, v. 2.12, STOE & Cie GmbH, **2005.**
[61] M. Tegel, *HConvert*, v. 0.8, Ludwig-Maximilians-Universität, München, **2011.**
[62] *Win XPOW GRAPHIC*, v. 2.16, STOE & Cie GmbH, Darmstadt, **2005.**
[63] *Win XPOW THEO*, v. 2.05, STOE & Cie GmbH, Darmstadt, **2004.**
[64] *Win XPOW Search*, v. 2.08, STOE & Cie GmbH, Darmstadt, **2005.**
[65] JCPDS, PDF 2, International Center for Diffraction Data, Swathmore, USA, **2001**.
[66] JCPDS, PDF 4+, International Center for Diffraction Data, Swathmore, USA, **2009**.

[67] A. Coelho, *TOPAS-Academic*, v. 4.1, Coelho Software, Brisbane, **2007.**
[68] B. H. Toby, *Journal of Applied Crystallography* **2005**, *38*, 1040.
[69] A. Le Bail, A. Jouanneaux, *Journal of Applied Crystallography* **1997**, *30*, 265.
[70] Y. Amemiya, J. Miyahara, *Nature (London, U. K.)* **1988**, *336*, 89.
[71] *BASREADER*, v. 2.13a, Raytest Isotopenmessgeräte GmbH, Straubenhardt, **1994.**
[72] *TINA*, v. 2.10g, Raytest Isotopenmessgeräte GmbH, Straubenhardt, **1993.**
[73] *X-RED 32 - Data reduction program*, v. 1.03, STOE & Cie GmbH, Darmstadt, **2002.**
[74] *XPREP - Data Preparation & Reciprocal Space Exploration*, v. 6.12, Bruker-AXS, **2001.**
[75] *X-Shape - Crystal Optimization for Numerical Absorption Correction*, v. 2.01, STOE & Cie GmbH, Darmstadt, **2001.**
[76] L. J. Farrugia, *Journal of Applied Crystallography* **1999**, *32*, 837.
[77] L. J. Farrugia, *WinGX - An integrated System of Windows Programs for the Solution, Refinment and Analysis of Single Crystal X-Ray Diffraction Data*, v. 1.70.01, University of Glasgow, **2005.**
[78] G. M. Sheldrick, *SHELXS-97 - A program for automatic solution of crystal structures*, v. 97-2, University of Göttingen, **1997.**
[79] G. M. Sheldrick, *SHELXL-97 - A program for crystal structure refinment*, v. 97-2, University of Göttingen, **1997.**
[80] G. M. Sheldrick, *Acta Crystallographica Section A* **2008**, *A64*, 112.
[81] K. Brandenburg, *Diamond - Crystal and Molecular Structure Visualization*, v. 3.1b, Crystal Impact GbR, Bonn, **2006.**
[82] *INCA*, v. 4.02, Oxford Instruments Analytical LTD, **2002.**
[83] Keithley, *Low Level Measurements, Precision DC Current, Voltage and Resistance Measurements*, 5th ed., Keithley Instruments Inc, Cleveland Ohio (USA), **1998**.
[84] P. Schnabel, *Philips Research Reports* **1964**, *19*, 43.
[85] L. J. van der Pauw, *Philips Research Reports* **1958**, *13*, 1.
[86] C. Kranenberg, *LEITMESS*, v. 2.53, Heinrich-Heine-Universität, Düsseldorf, **1998.**
[87] *Origin*, v. 6.1052, OriginLab Corporation, Northampton, USA,, **2000.**
[88] M. Mc Elfresh, *Fundamentals of Magnetism and Magnetic Measurments featuring Quantum Design's Magnetic Porperty Measurement System*, Quantum Design & Purdue University, **1994**.
[89] *Magnetic Property Measurement System MPMS XL, Hardware Reference Manual*, Quantum Design, San Diego, **2005**.
[90] *MPMS MultiVU*, v. 1.56 Build 72, Quantum Design Inc., San Diego, **2005.**
[91] M. Tegel, *SQUID Processor*, v. 0.2 (Mac/Windows), Ludwig-Maximilians-Universität, München, **2010.**

[92] H. Lueken, *Magnetochemie*, Table A.3, p. 426, Teubner Verlag, Stuttgart, Leipzig, **1999**.
[93] R. Frankovsky, *Synthese und Eigenschaften von $LaFe_2Ge_2$ und $La_{1-x}A_xFe_2Ge_2$ (A = Sr, Ca)*, Diploma thesis, Ludwig-Maximilians-Universität (München), **2009**.
[94] X. C. Wang, Q. Q. Liu, Y. X. Lv, W. B. Gao, L. X. Yang, R. C. Yu, F. Y. Li, C. Q. Jin, *Solid State Communications* **2008**, *148*, 538.
[95] G. Wu, Y. L. Xie, H. Chen, M. Zhong, R. H. Liu, B. C. Shi, Q. J. Li, X. F. Wang, T. Wu, Y. J. Yan, J. J. Ying, X. H. Chen, *Journal of Physics: Condensed Matter* **2009**, *21*, 142203.
[96] P. L. Alireza, J. Gillett, Y. T. C. Ko, S. E. Sebastian, G. G. Lonzarich, *Journal of Physics: Condensed Matter* **2009**, *21*, 012208.
[97] W. Yu, A. A. Aczel, T. J. Williams, S. L. Bud'ko, N. Ni, P. C. Canfield, G. M. Luke, *Physical Review B* **2009**, *79*, 020511.
[98] A. Kreyssig, M. A. Green, Y. Lee, G. D. Samolyuk, P. Zajdel, J. W. Lynn, S. L. Bud'ko, M. S. Torikachvili, N. Ni, S. Nandi, J. B. Leao, S. J. Poulton, D. N. Argyriou, B. N. Harmon, R. J. McQueeney, P. C. Canfield, A. I. Goldman, *Physical Review B* **2008**, *78*, 184517.
[99] D. Rossi, R. Marazza, R. Ferro, *Journal of the Less Common Metals* **1978**, *58*, 203.
[100] G. W. Hull, J. H. Wernick, T. H. Geballe, J. V. Waszczak, J. E. Bernardini, *Physical Review B* **1981**, *24*, 6715.
[101] H. Fujii, T. Mochiku, H. Takeya, A. Sato, *Physical Review B* **2005**, *72*, 214520.
[102] T. Mochiku, H. Fujii, H. Takeya, T. Wuernisha, K. Mori, T. Ishigaki, T. Kamiyama, K. Hirata, *Physica C: Superconductivity* **2007**, *463-465*, 182.
[103] J. P. Yarmolyuk, J. G. Akselrud, Y. N. Grin, V. S. Fundamenskii, E. I. Gladyshevski, *Soviet Physics Crystallography* **1979**, *24*, 332.
[104] Z. Ban, M. Sikirica, *Acta Crystallographica* **1965**, *18*, 594.
[105] I. Felner, M. Schieber, *Solid State Communications* **1973**, *13*, 457.
[106] H. Kleinke, B. Harbrecht, *Zeitschrift für anorganische und allgemeine Chemie* **2000**, *626*, 1851.
[107] C.-S. Lee, E. Dashjav, H. Kleinke, *Chemistry of Materials* **2001**, *13*, 4053.
[108] E. Dashjav, C.-S. Lee, H. Kleinke, *Journal of Solid State Chemistry* **2002**, *169*, 96.
[109] W. N. Stassen, M. Sato, L. D. Calvert, *Acta Crystallographica Section B* **1970**, *26*, 1534.
[110] I. R. Mokra, O. I. Bodak, *Dopovidi Akademii Nauk Ukrains'koi RSR, Seriya A: Fiziko-Matematichni ta Tekhnichni Nauki* **1979**, 312.
[111] S. Derakhshan, E. Dashjav, H. Kleinke, *European Journal of Inorganic Chemistry* **2004**, *2004*, 1183.
[112] R. Kuentzler, H. R. Khan, *Physics Letters A* **1985**, *113*, 89.
[113] H. Ogino, Y. Matsumura, Y. Katsura, K. Ushiyama, S. Horii, K. Kishio, J.-i. Shimoyama, *Superconductor Science and Technology* **2009**, *22*, 075008.

[114] W. J. Zhu, P. H. Hor, *Journal of Solid State Chemistry* **1997**, *134*, 128.
[115] W. J. Zhu, P. H. Hor, *Inorganic Chemistry* **1997**, *36*, 3576.
[116] A. Ubaldini, E. Giannini, C. Senatore, D. van der Marel, *Physica C: Superconductivity* **2010**, *470, Supplement 1*, S356.
[117] A. M. Kusainova, P. S. Berdonosov, L. G. Akselrud, L. N. Kholodkovskaya, V. A. Dolgikh, B. A. Popovkin, *Journal of Solid State Chemistry* **1994**, *112*, 189.
[118] Y.-Z. Zhang, H. O. Jeschke, R. Valenti, Institut für theoretische Physik, Goethe-Universität Frankfurt, Germany, *Personal Communication* **2009**.
[119] G. Ferey, *Journal of Solid State Chemistry* **2000**, *152*, 37.
[120] O. M. Yaghi, M. O'Keeffe, N. W. Ockwig, H. K. Chae, M. Eddaoudi, J. Kim, *Nature* **2003**, *423*, 705.
[121] C. Mellot-Draznieks, G. Ferey, *Current Opinion in Solid State & Materials Science* **2003**, *7*, 13.
[122] L. Cario, H. Kabbour, A. Meerschaut, *Chemistry of Materials* **2005**, *17*, 234.
[123] H. Kabbour, L. Cario, F. Boucher, *Journal of Materials Chemistry* **2005**, *15*, 3525.
[124] P. R. Bonneau, R. F. Jarvis, R. B. Kaner, *Nature* **1991**, *349*, 510.
[125] P. Schmidt, *Thermodynamische Analyse der Existenzbereiche fester Phasen - Prinzpien der Syntheseplanung in der anorganischen Festkörperchemie*, Habilitation thesis, Technische Universität (Dresden), **2007**.
[126] A. Kondrat, J. E. Hamann-Borrero, N. Leps, M. Kosmala, O. Schumann, A. Köhler, J. Werner, G. Behr, M. Braden, R. Klingeler, B. Büchner, C. Hess, *The European Physical Journal B* **2009**, *70*, 461.
[127] H. H. Klauss, H. Luetkens, R. Klingeler, C. Hess, F. J. Litterst, M. Kraken, M. M. Korshunov, I. Eremin, S. L. Drechsler, R. Khasanov, A. Amato, J. Hamann-Borrero, N. Leps, A. Kondrat, G. Behr, J. Werner, B. Büchner, *Physical Review Letters* **2008**, *101*, 077005.
[128] T. Nomura, Y. Inoue, S. Matsuishi, M. Hirano, J. E. Kim, K. Kato, M. Takata, H. Hosono, *Superconductor Science and Technology* **2009**, *22*, 055016.
[129] Y. Xiao, Y. Su, R. Mittal, T. Chatterji, T. Hansen, S. Price, C. M. N. Kumar, J. Persson, S. Matsuishi, Y. Inoue, H. Hosono, T. Brueckel, *Physical Review B* **2010**, *81*, 094523.
[130] Z. Li, Y. Fang, X. Ma, H. Pang, F. Li, *Physical Review B* **2011**, *84*, 134509.
[131] X. Zhu, F. Han, P. Cheng, G. Mu, B. Shen, L. Fang, H.-H. Wen, *Europhysics Letters* **2009**, *85*, 17011.
[132] P. Schobinger-Papamantellos, P. Fischer, O. Vogt, E. Kaldis, *Journal of Physics C: Solid State Physics* **1973**, *6*, 725.
[133] H. Wadati, I. Elfimov, G. A. Sawatzky, *Physical Review Letters* **2010**, *105*, 157004.
[134] S. Konbu, K. Nakamura, H. Ikeda, R. Arita, *Solid State Communications* **2012**, *152*, 728.

[135] Y. Texier, Y. Laplace, P. Mendels, J. T. Park, G. Friemel, D. L. Sun, D. S. Inosov, C. T. Lin, J. Bobroff, *EPL (Europhysics Letters)* **2012**, *99*, 17002.
[136] A. S. Sefat, D. J. Singh, L. H. VanBebber, Y. Mozharivskyj, M. A. McGuire, R. Jin, B. C. Sales, V. Keppens, D. Mandrus, *Physical Review B* **2009**, *79*, 224524.
[137] K. Marty, A. D. Christianson, C. H. Wang, M. Matsuda, H. Cao, L. H. VanBebber, J. L. Zarestky, D. J. Singh, A. S. Sefat, M. D. Lumsden, *Physical Review B* **2011**, *83*, 060509(R).
[138] A. Thaler, H. Hodovanets, M. S. Torikachvili, S. Ran, A. Kracher, W. Straszheim, J. Q. Yan, E. Mun, P. C. Canfield, *Physical Review B*, *84*, 144528.
[139] G. S. Tucker, D. K. Pratt, M. G. Kim, S. Ran, A. Thaler, G. E. Granroth, K. Marty, W. Tian, J. L. Zarestky, M. D. Lumsden, S. L. Bud'ko, P. C. Canfield, A. Kreyssig, A. I. Goldman, R. J. McQueeney, *Physical Review B* **2012**, *86*, 020503(R).
[140] C. Fang, H. Yao, W.-F. Tsai, J. Hu, S. A. Kivelson, *Physical Review B* **2008**, *77*, 224509.
[141] C. Xu, M. Müller, S. Sachdev, *Physical Review B* **2008**, *78*, 020501(R).
[142] R. M. Fernandes, L. H. VanBebber, S. Bhattacharya, P. Chandra, V. Keppens, D. Mandrus, M. A. McGuire, B. C. Sales, A. S. Sefat, J. Schmalian, *Physical Review Letters* **2010**, *105*, 157003.
[143] R. M. Fernandes, A. J. Millis, *arXiv:1208.3412v2* **2012**.
[144] S. Matsuishi, Y. Inoue, T. Nomura, Y. Kamihara, M. Hirano, H. Hosono, *New Journal of Physics* **2009**, *11*, 025012.
[145] H. H. Klauss, H. Luetkens, R. Klingeler, C. Hess, F. J. Litterst, M. Kraken, M. M. Korshunov, I. Eremin, S. L. Drechsler, R. Khasanov, A. Amato, J. Hamann-Borrero, N. Leps, A. Kondrat, G. Behr, J. Werner, B. Büchner, *Physical Review Letters* **2008**, *101*, 077005.
[146] A. Yaouanc, P. D. de Réotier, *Muon Spin Rotation, Relaxation and Resonance*, Oxford University Press, Oxford, **2011**.
[147] N. Emery, E. J. Wildman, J. M. S. Skakle, G. Giriat, R. I. Smith, A. C. McLaughlin, *Chemical Communications* **2010**, *46*, 6777.
[148] Y. Singh, M. A. Green, Q. Huang, A. Kreyssig, R. J. McQueeney, D. C. Johnston, A. I. Goldman, *Physical Review B* **2009**, *80*, 100403(R).
[149] A. T. Nientiedt, W. Jeitschko, P. G. Pollmeier, M. Brylak, *Zeitschrift für Naturforschung B* **1997**, *52*, 560.
[150] N. Emery, E. J. Wildman, J. M. S. Skakle, A. C. McLaughlin, R. I. Smith, A. N. Fitch, *Physical Review B* **2011**, *83*, 144429.
[151] P. Villars, K. Cenzual, Pearson's Crystal Data - Crystal Structure Database for Inorganic Compounds (on CD-ROM), ASM International, Materials Park, Ohio, USA, **2009/2010**.

# Full list of Publications

**Superconductivity up to 35 K in the Iron Platinum Arsenides**

**$(CaFe_{1-x}Pt_xAs)_{10}Pt_{4-y}As_8$ with Layered Structures**

C. Löhnert, T. Stürzer, M. Tegel, R. Frankovsky, G. Friederichs, D. Johrendt
*Angewandte Chemie International Edition* **2011**, *50*, 9195.

**Synthesis of $LaO_{1-x}F_xFeAs$ (x = 0-0.15) via solid state metathesis reaction**

R. Frankovsky, A. Marchuk, R. Pobel, D. Johrendt
*Solid State Communications* **2012**, *152*, 632. (chapter 5)

**High-Pressure Synthesis and Characterization of the Alkali Diazenide $Li_2N_2$**

S. B. Schneider, R. Frankovsky, and W. Schnick
*Angewandte Chemie International Edition* **2012**, *51*, 1873.

**Synthesis of Alkaline Earth Diazenides $M_{AE}N_2$ ($M_{AE}$ = Ca, Sr, Ba) by Controlled Thermal Decomposition of Azides under High Pressure**

S. B. Schneider, R. Frankovsky, and Wolfgang Schnick
*Inorganic Chemistry* **2012**, *51*, 2366.

**Ferromagnetism and the formation of interlayer $As_2$-dimers in $Ca(Fe_{1-x}Ni_x)_2As_2$**

R. Pobel, R. Frankovsky and D. Johrendt
*Z. Naturforsch B* **2013**, in press
http://arxiv.org/abs/1302.3046 (arxiv: 1302.3046; **2013**).

**Short range magnetic order and effective suppression of superconductivity by manganese-doping in $LaFe_{1-x}Mn_xAsO_{1-y}F_y$**

R. Frankovsky, H. Luetkens, F. Tambornino, A. Marchuk, G. Pascua, A. Amato, H. H. Klauss, D. Johrendt
submitted to *Physical Review B*
http://arxiv.org/abs/1303.6833 (*arxiv: 1303.6833*, **2013**). (chapter 7)

# Conference contributions

R. Frankovsky, D. Johrendt

**Synthese von $LaFeAsO_{1-x}F_x$ via Salzmetathesereaktion** (talk)

Hirschegg Festkörper-Seminar, Hirschegg (Austria), 23/06/2011 – 26/06/2011.

R. Frankovsky, A. Marchuk, R. Pobel, D. Johrendt

**Synthesis of $LaFeAsO_{1-x}F_x$ (x = 0-0.15) via solid state metathesis reaction** (poster)

International Workshop on Novel Superconductors and Super Materials 2011

Tokyo (Japan), 06/03/2011 – 08/03/2011.